TECHNISCHE UNIVERSITÄT MÜNCHEN

Lehrstuhl für Biochemie

Structural and Functional Studies on Proteins involved in Proteasomal Degradation, Photosynthesis and the Cellular Stress Response

Ferdinand T. E. Alte

Vollständiger Abdruck der von der Fakultät für Chemie der Technischen Universität München zur Erlangung des akademischen Grades eines
Doktors der Naturwissenschaften (Dr. rer. nat.)
genehmigten Dissertation.

Vorsitzender: Univ.- Prof. Dr. L. Hintermann
Prüfer der Dissertation: 1. Univ.- Prof. Dr. M. Groll
2. Univ.- Prof. Dr. Th. Kiefhaber
3. Univ.- Prof. Dr. J. Buchner

Die Dissertation wurde am 30.11.2011 bei der Technischen Universität München eingereicht und durch die Fakultät für Chemie am 31.01.2012 angenommen.

Index

1 Abstract

Biological questions often address the understanding of molecular form and function. In this context, biomolecular X-ray crystallography gives answers to two major challenges in modern life sciences. Since the method allows the accurate determination of structural details at atomic resolution even for large molecular assemblies, the behavior of entire biological systems can be unraveled. Moreover, novel therapeutic agents may be identified through analysis of drug-target interactions as part of a comprehensive structure guided drug design procedure. In particular, the dissection of the relation between structure and function is a powerful tool for the elucidation of catalytic mechanisms of enzymes, binding modes of interaction partners, the dynamics of a protein and the self assembly of oligomeric complexes.

In the course of establishing a crystallographic facility at the department of chemistry of the Technical University of Munich, the determination of crystal structures was implemented in three projects covering the fields of proteasomal degradation, photosynthesis and the cellular stress response. Furthermore, relevant functional properties were investigated as well.

Posttranslational modification of proteins by the small Ubiquitin-like modifier SUMO represents an important regulatory mechanism for protein function and localization, that controls diverse cellular events including transcriptional regulation, nuclear transport, cell cycle progression, DNA repair and signal transduction. Compared to the multitude of substrate proteins, a relatively small number of enzymes is involved in the dynamic conjugation and removal of SUMO-tags. Only two SUMO-specific proteases in yeast and six in human have been identified up to now. Recently, a third SUMO-directed protease (Wss1) with

a potential role in proteasomal degradation was predicted for *S. cerevisiae*. However, no experimental evidence for structural properties of Wss1 has been published so far. In the present work, the crystal structure of a Wss1-homologue from *S. pombe* (SpWss1b) was determined at a resolution of 1.0 Å (Alte et al., manuscript in preparation). The molecular architecture unambiguously reveals that Wss1 is a metalloenzyme featuring a M1/M34-peptidase-like fold. This finding clearly differentiates Wss1 from the hitherto known types of de-SUMOylating enzymes. Moreover, initial *in vitro* investigations demonstrate proteolytic activity of SpWss1b. Additional *in vivo* experiments applying yeast genetic methods showed that disruption of Wss1 can be compensated by *S. pombe* even under stress conditions.

Photosynthesis is a biochemical process that exploits the energy from sunlight to convert carbon dioxide into organic compounds. Plants contain special organelles named chloroplasts which harbour the actual site of photosynthesis: membrane stacks called thylakoids. Ferredoxin:NADP(H) Oxidoreductase (FNR) is a key enzyme of photosynthetic electron transport required for the generation of reduction equivalents. Recently, two proteins were found to be involved in membrane-anchoring of FNR by specific interaction via a conserved Ser/Pro-rich motif: Tic62 and Trol. In collaboration with the group of Prof. Soll (LMU Munich) the crystal structure of a ternary complex consisting of two molecules FNR and a synthetic peptide representing the FNR-binding motif from Tic62 was determined at 1.7 Å resolution (Alte et al., 2010). The peptide, which forms a poly-proline type II helix, induces self-assembly of the two FNR monomers into a back-to-back dimer by substantially increasing the contact area. Since binding occurs opposite to the FNR active sites, its activity is not affected by the interaction.

Surface plasmon resonance analyses disclose a high affinity of FNR to the binding motif, which is strongly increased under acidic conditions. The pH of the chloroplast stroma changes dependent on the light conditions from neutral to slightly acidic in complete darkness or to alkaline at saturating light conditions. Recruiting of FNR to the thylakoids could therefore represent a regulatory mechanism to adapt FNR availability/activity to photosynthetic electron flow.

Molecular chaperones, also referred to as heat shock proteins (Hsps), are the major players in the cellular heat stress response. They prevent client proteins from thermal unfolding and unspecific aggregation, thereby maintaining both the structural integrity of individual proteins as well as the overall cellular organization. Most chaperone classes comprise ATP-dependent Hsp-systems, which actively participate in refolding of unstructured substrate proteins, thus fulfilling a "foldase" function. By contrast, members of the family of small Hsps (sHsps) exclusively exhibit a "holdase" activity by shielding hydrophobic regions of nonnative proteins. In collaboration with the group of Prof. Buchner (TUM), the crystal structure of Hsp17.7, a sHsp from the polyextremophilic bacterium *D. radiodurans* was determined at 2.4 Å resolution (Bepperling et al., manuscript in preparation). Hsp17.7 crystallized as a homodimer, and the monomers adopt the characteristic α-crystallin core fold. Intriguingly, the conserved C-terminal Ile-x-Ile/Val-motif forms a defined crystal contact to a neighbouring dimer. This inter-molecular interaction is usually used for the physiological oligomerization of sHsps. However, Hsp17.7 clearly prefers a dimeric state both *in vitro* and *in vivo*. Comparison of the extended loop region to other organisms revealed significant structural divergence, giving rise to the assumption of an aberrant dimer packing, which may contribute to the atypical quaternary structure of Hsp17.7.

2 Zusammenfassung

Biologische Fragestellungen richten sich oft an das Verständnis molekularer Formen und Funktionen. In diesem Kontext gibt die biomolekulare Röntgenkristallographie Antworten auf zwei große Herausforderungen moderner Biowissenschaften. Da die Methode eine genaue Bestimmung struktureller Details bei atomarer Auflösung sogar für hochmolekulare Komplexe ermöglicht, kann das Verhalten vollständiger biologischer Systeme aufgeklärt werden. Ebenso ist die Identifizierung neuer therapeutischer Wirkstoffe durch die Analyse der Wechselwirkungen mit dem Zielmolekül im Rahmen einer umfassenden strukturbasierten Medikamentenentwicklung möglich. Die Entschlüsselung des Zusammenhangs von Struktur und Funktion ist insbesondere ein leistungsstarkes Werkzeug zur Aufklärung von Enzymmechanismen, Bindungsmodi von Interaktionspartnern, Proteindynamik sowie Selbstorganisation oligomerer Komplexe.

Im Zuge der Etablierung einer kristallographischen Einrichtung an der Fakultät für Chemie der Technischen Universität München wurde die Bestimmung von Kristallstrukturen in drei Projekten, welche die Themenbereiche Proteinabbau, Photosynthese und zelluläre Stressantwort abdecken, umgesetzt. Zudem wurden relevante funktionelle Eigenschaften untersucht.

Die posttranslationale Modifikation von Proteinen durch den Ubiquitin-ähnlichen Modifikator SUMO stellt einen wichtigen Regulationsmechanismus für die Funktion und Lokalisierung von Proteinen dar, der diverse zelluläre Vorgänge wie z.B. Transkription, Kerntransport, Zellzyklus, DNA-Reparatur und Signalweitergabe kontrolliert. Verglichen mit der Vielzahl an Substratproteinen, sind nur relativ wenige Enzyme an der dynamischen Anheftung und Abspaltung der SUMO-Marker beteiligt. Bislang wurden in der Hefe zwei und im Menschen sechs

SUMO-spezifische Proteasen entdeckt. Kürzlich wurde für die Bäckerhefe eine dritte SUMO-gerichtete Protease (Wss1) mit einer potentiellen Rolle im Protein-abbau vorhergesagt. Bislang sind jedoch keine experimentellen Belege für strukturelle Eigenschaften von Wss1 veröffentlicht. In der vorliegenden Arbeit wurde die Kristallstruktur eines Wss1-Homologs aus der Spalthefe (SpWss1b) mit einer Auflösung von 1,0 Å bestimmt (Alte et al., Manuskript in Vorbereitung). Der Molekülaufbau zeigt, dass Wss1 ein Metalloenzym mit einer Peptidase-ähnlichen Faltung ist (M1/M34-Familie). Dieser Befund unterscheidet Wss1 deutlich von den bisher bekannten SUMO-abspaltenden Enzymen. Darüber hinaus konnte durch *in vitro* Untersuchungen proteolytische Aktivität von SpWss1b nachgewiesen werden. Hefegenetische *in vivo* Versuche belegen, dass eine Wss1-Deletion sogar unter Stressbedingungen von *S. pombe* kom-pensiert werden kann.

Die Fotosynthese ist ein biochemischer Prozess, bei dem die Sonnenenergie genutzt wird, um aus Kohlendoxid organische Verbindungen aufzubauen. Pflan-zen enthalten spezielle Organellen namens Chloroplasten, die den eigentlichen Schauplatz der Fotosynthese beherbergen: Membranstapel genannt Thylakoide. Die Ferredoxin:NADP(H) Oxidoreduktase (FNR) ist ein Schlüsselenzym im foto-synthetischen Elektronentransport, das für die Bildung von Reduktionsäquivalen-ten benötigt wird. Kürzlich wurden mit Tic62 und Trol zwei Proteine beschrieben, die an der Membranverankerung der FNR durch spezifische Wechselwirkungen eines konservierten Ser/Pro-reichen Motivs beteiligt sind. In Zusammenarbeit mit der Arbeitsgruppe von Prof. Soll (LMU München) wurde die Kristallstruktur eines ternären Komplexes bestehend aus zwei Molekülen FNR und einem synthe-tischen Peptid, welches das FNR-Bindemotiv von Tic62 repräsentiert, mit einer

Auflösung von 1,7 Å bestimmt (Alte et al., 2010). Das Peptid bildet eine Polyprolin-II-Struktur aus und induziert die Selbstassemblierung der beiden FNR-Monomere zu einem Rücken-an-Rücken Dimer, indem es die Kontaktfläche maßgeblich vergrößert. Da diese Zusammenlagerung gegenüber der katalytischen Zentren der FNR stattfindet, ist ihre Aktivität dadurch nicht beeinflusst. Eine Oberflächenplasmonenresonanz-spektroskopie wies eine hohe Affinität der FNR zu dem Bindungsmotiv nach, die im Sauren am stärksten ist. Der pH-Wert des Chloroplastenstromas verändert sich in lichtabhängigerweise von neutral zu leicht sauer wenn es dunkel ist oder zu basisch bei vollem Lichteinfall. Die Rekrutierung der FNR an die Thylakoide könnte somit einen Regulations-mechanismus darstellen, um die FNR-Verfügbarkeit bzw. Aktivität dem fotosyn-thetischen Elektronenfluss anzupassen.

Molekulare Chaperone, die auch als Hitzeschockproteine (Hsps) bezeichnet wer-den, sind die Hauptakteure der zellulären Antwort auf Hitzestress. Sie unterbin-den die thermische Entfaltung und unspezifische Aggregation von Substrat-proteinen und erhalten dadurch sowohl die strukturelle Integrität einzelner Proteine als auch die gesamte Zellorganisation. Die meisten Chaperonklassen umfassen ATP-abhängige Hsp-Systeme, die aktiv unstrukturierte Proteine im Sinne einer „Foldase"-funktion rückfalten. Im Gegensatz dazu weisen kleine Hitzeschockproteine (sHsps) ausschließlich eine „Holdase"-Aktivität auf, indem sie hydrophobe Regionen nicht nativer Proteine abschirmen. In Zusammenarbeit mit der Arbeitsgruppe von Prof. Buchner (TUM) wurde die Kristallstruktur von Hsp17.7, ein sHsp aus dem polyextremophilen Bakterium *D. radiodurans*, mit einer Auflösung von 2,4 Å bestimmt (Bepperling et al., Manuskript in Vorbereitung). Hsp17.7 kristallisierte als Homodimer. Die Monomere nehmen

dabei die charakteristische α-Crystallin Faltung an. Interessanterweise bildet das konservierte C-terminale Ile-x-Ile/Val-Motiv einen definierten Kristallkontakt zu einem benachbarten Dimer aus. Diese intermolekulare Wechselwirkung wird von sHsps üblicherweise zur physiologischen Oligomerisierung genutzt. Hsp17.7 tritt aber dennoch sowohl *in vitro* als auch *in vivo* bevorzugt nur als Dimer auf. Ein Vergleich der erweiterten Loop-Region mit anderen Organismen zeigt signifikante strukturelle Unterschiede, die eine abweichende Dimerpackung vermuten lassen, welche möglicherweise zur untypischen Quartärstruktur von Hsp17.7 beiträgt.

3 Objective

The biophysical properties and biological functions of proteins and their complex macromolecular assemblies are defined by their molecular structure. Thus, analysis of the three-dimensional structure sheds light on the question of how biochemical processes function at atomic level. For instance, the dissection of the structure-function relationship is a powerful tool for unraveling catalytic mechanisms of enzymes, binding modes of interaction partners, the dynamics of a protein and the self assembly of oligomeric complexes. The methods by which one can determine protein structures comprise NMR (nuclear magnetic resonance), EM (electron microscopy) and X-ray crystallography. Over the past decades, NMR and EM have been well established at the department of chemistry of the Technical University of Munich, whereas macromolecular X-ray crystallographic expertise was not available at the faculty. A closer look at the statistics of published structures in the protein data bank points out the need for a crystallographic facility at the department, in the sense of a comprehensive structural biology infrastructure. About 87% of all released entries were determined by X-ray crystallography, roughly 12% by NMR and 0,5% by EM. Consequently, for a first generation coworker, the aim of this thesis was directed towards establishing in-house X-ray structure determination of proteins starting from genomic DNA preparation. The implementation of this objective as a "proof of concept" is demonstrated by three selected projects, two of which have been collaborations with other institutes from the CIPSM cluster.

The first project covers the field of protein degradation pathways. The goal was to structurally and functionally characterize the putative deSUMOylating metallo-peptidase Wss1. SUMOs (small ubiquitin-like modifiers) are ubiquitin-related

proteins that become covalently attached to cellular target proteins, with effects on either the activity, the localization or the interactions of those targets (Geiss-Friedlander and Melchior, 2007). SUMO conjugation is a highly dynamic process that can be rapidly reversed by the action of specific proteases (Mukhopadhyay and Dasso, 2007). In a bioinformatic screen for deSUMOylating enzymes, Wss1p was predicted to function as a Zn-dependent metalloprotease, which would be the first example of a Zincin-like metalloprotease involvement in SUMO-signaling (Iyer et al., 2004). Wss1p was initially characterized as <u>w</u>eak <u>s</u>uppressor of a Δ<u>smt3</u>-phenotype in yeast (Biggins et al., 2001) with SMT3 from *S.cerevisiae* being the first reported SUMO-gene (Meluh and Koshland, 1995). Yet, both the cellular function and the structure of Wss1p were unknown at the beginning of this thesis. A funnel system approach was applied by cloning WSS1-constructs of varying length from different organisms. Heterologous expression conditions were tested and soluble proteins should be purified chromatographically for biochemical characterization and crystal trials. High-throughput screenings for crystallization conditions were set up with automated pipetting robot systems and data sets of resulting crystals should be collected with the new in-house x-ray beamline. For anomalous phasing experiments, additional data sets were collected at the SLS beamline. Analysis of the structure should allow conclusions about the substrate binding mode as well as the reaction mechanism of the metalloprotease. Furthermore, for initial functional analysis, deletion strains should be generated and investigated for putative phenotypes.

In a collaboration project with the group of Prof. Soll (Chair of Plant Biochemistry and Physiology, Ludwig-Maximilians-Universität München) a known interaction of

two plant proteins was structurally and functionally examined. Ferredoxin: NADP(H) Oxidoreductase (FNR) is a key enzyme of photosynthetic electron transport required for generation of reduction equivalents. Recently, two proteins were found to be involved in membrane-anchoring of FNR by specific interaction via a conserved Ser/Pro-rich motif: Tic62 and Trol (Benz et al., 2009; Juric et al., 2009). To date, the functional relevance as well as structural characteristics of FNR membrane recruitment by interaction with Tic62/Trol remain elusive. Therefore, the crystal structure of an artificial complex comprising FNR and a synthetic peptide, representing the conserved binding motif of Tic62, was solved. Moreover, FNR activity measurements dissected the performance of the complex-bound FNR compared to the free enzyme. Finally, SPR analyses should clarify the influence of the pH on the binding affinity of FNR to the peptide.

A second, in-house collaboration project with the group of Prof. Buchner (Chair of Biotechnology, TUM) targeted the structural and functional divergence of the two small heat shock proteins (sHsps) of the stress-tolerant bacterium *Deinococcus radiodurans* (Bepperling et al., manuscript in preparation). Small Hsps are molecular chaperones which prevent protein aggregation as part of the cellular stress response. So far, detailed studies about bacterial sHsp-systems only exist for *E.coli*. Hence, the investigations on *D. radiodurans* aim to either generalize or specify features of the prokaryotic sHsp stress response system. As contribution to this collaboration, crystal structures of both sHsps should be obtained and compared to existing sHsp-structures of other organisms.

4 Materials & Methods

This section mainly covers methods applied for the Wss1-project. For projects carried out in collaboration with other groups only crystallographic procedures are described.

4.1 Materials

4.1.1 Chemicals

Acetic acid (100 %, p.a.)	Roth (Karlsruhe, DE)
Acrylamide/Bis-solution (40 %, 29:1)	Roth (Karlsruhe, DE)
Agar	Merck (Darmstadt, DE)
Agarose (ultra pure)	Roth (Karlsruhe, DE)
Ammoniumperoxodisulfate (APS)	Merck (Darmstadt, DE)
Ampicillin	AppliChem (Darmstadt, DE)
5-Bromo-4-chloro-3-indoylphosphate (BCIP)	Roth (Karlsruhe, DE)
Bromophenol Blue S	Serva (Heidelberg, DE)
Coomassie Brilliant Blue R-250	Serva (Heidelberg, DE)
Ethanol (96 %)	Merck (Darmstadt, DE)
Ethidium bromide	Sigma-Aldrich (St. Louis, US)
Ethylenediaminetetraacetic acid (EDTA)	Merck (Darmstadt, DE)
L-Glutathione (reduced)	AppliChem (Darmstadt, DE)
Glycerol (anhydrous)	Sigma-Aldrich (St. Louis, US)
Glycine (99 %)	Sigma-Aldrich (St. Louis, US)
Hydrochloric acid	Merck (Darmstadt, DE)

Hydroxyurea (98 %)	Sigma-Aldrich (St. Louis, US)
Imidazole	Merck (Darmstadt, DE)
Isopropyl alcohol	Merck (Darmstadt, DE)
Isopropyl β-D-1-thiogalactopyranoside (IPTG)	Sigma-Aldrich (St. Louis, US)
Kanamycin	AppliChem (Darmstadt, DE)
Magnesium chloride hexahydrate	Merck (Darmstadt, DE)
Malt extract	Sigma-Aldrich (St. Louis, US)
2-Mercaptoethanol, pure	Merck (Darmstadt, DE)
Methanol	Merck (Darmstadt, DE)
Nitro blue tetrazolium chloride (NBT)	Roth (Karlsruhe, DE)
Pefabloc SC (protease inhibitors)	Roche (Risch, CH)
Peptone	Merck (Darmstadt, DE)
Ponceau S	Sigma-Aldrich (St. Louis, US)
Sodium chloride	Merck (Darmstadt, DE)
Sodium dodecyl sulfate (SDS)	Roth (Karlsruhe, DE)
Sodium hydroxide	Merck (Darmstadt, DE)
Tetramethylethylenediamine (TEMED)	Roth (Karlsruhe, DE)
PEG(20)sorbitan monolaurate (Tween 20)	Merck (Darmstadt, DE)
Tris(hydroxymethyl)-aminomethane (Tris)	Merck (Darmstadt, DE)
Yeast extract	Merck (Darmstadt, DE)

4.1.2 Kits and ready-made Solutions

peqGOLD Cycle-Pure Kit   peqlab (Erlangen, DE)

peqGOLD Gel Extraction Kit   peqlab (Erlangen, DE)

peqGOLD Plasmid Miniprep Kit I and II   peqlab (Erlangen, DE)

DNA Ladder-Mix (100 - 10000 bp)   peqlab (Erlangen, DE)

dNTP Mix   Bioline (Luckenwalde, DE)

Roti®-Mark STANDARD   Roth (Karlsruhe, DE)

Roti®-Mark PRESTAINED   Roth (Karlsruhe, DE)

4.1.3 Enzymes and Antibodies

Phusion® DNA Polymerase (incl. buffer)   Finnzymes (Vantaa, FI)

Restriction Enzymes (incl. buffer)   NEB (Ipswich, US)

T4 DNA Ligase   Invitrogen (Carlsbad, US)

DNAse I   Sigma-Aldrich (St. Louis, US)

Tev-Protease   produced in-house

Gel Filtration LMW/HMW Calibration Kit   GE Healthcare

                                                      (Chalfont St. Giles, GB)

Monoclonal Anti-Polyhistidine   Sigma-Aldrich (St. Louis, US)

antibody produced in mouse

Anti-Mouse IgG-Alkaline Phosphatase   Sigma-Aldrich (St. Louis, US)

produced in rabbit

Alkaline Phosphatase   Roche (Risch, CH)

4.1.4 Chromatographic Material

HisTrap^{TM} FF Ni-NTA columns (1ml, 5ml)	GE Healthcare
	(Chalfont St. Giles, GB)
Glutathione Sepharose 4B	GE Healthcare
HiPrep 26/10 Desalting	GE Healthcare
HiLoad 26/60 Superdex 75/200 pg	GE Healthcare

The Glutathione Sepharose column was self packed with a volume of 19 ml.

4.1.5 Miscellaneous Material

Electroporation Cuvettes (2 mm)	peqlab (Erlangen, DE)
Amicon Stirred Cells	Millipore (Billerica, US)
Amicon Ultra Centrifugal Filters	Millipore (Billerica, US)
Whatman Filter Paper	GE Healthcare
Nitrocellulose Membrane	Roth (Karlsruhe, DE)
Ultrasonic vessel	G.Heinemann
	(Schwäbisch Gmünd, DE)

4.1.6 Equipment

Balances

Precision balance BP 3100 P	Sartorius (Göttingen, DE)
Analytical balance TE 124S	Sartorius (Göttingen, DE)

Centrifuges

SIGMA1-14 (rotor 12094)	SIGMA laboratory centrifuges (Osterode am Harz, DE)
SIGMA 3-30K (rotors 12150-H and 12154-H)	SIGMA laboratory centrifuges
SIGMA 4K15 (rotor 11150 and 13350)	SIGMA laboratory centrifuges
SIGMA 6-16K (rotor 12500)	SIGMA laboratory centrifuges
SIGMA 8K (rotor 11805 and 13850)	SIGMA laboratory centrifuges

Chromatography Platforms

ÄKTAprime^{TM} plus	GE Healthcare
ÄKTApurifier^{TM}	GE Healthcare

Crystallography

Art Robbins Instruments Phoenix	Dunn Labortechnik (Asbach, DE)
Art Robbins Instruments Intelli-Plates (96-well)	Dunn Labortechnik
MICROLAB$^{®}$ STARlet	Hamilton (Reno, US)
X8 PROTEUM in-house beamline	Bruker AXS (Karlsruhe, DE)
Protein Crystallization Screening Suites	QIAGEN (Hilden, DE)
Cooled Incubator Series 3000	RUMED$^{®}$ Rubarth Apparate (Laatzen, DE)
Zoom stereo microscope SZX10/KL1500LCD	Olympus (Tokio, JP)

Quick Combi Sealer Plus	HJ-Bioanalytik (Mönchengladbach, DE)
SuperClear Pregreased 24 Well Plate	Crystalgen (New York, US)
Siliconized Glass Cover Slides	Hampton (Aliso Viejo, US)
Mounted CryoLoop™	Hampton (Aliso Viejo, US)
CrystalCap HT™ for CryoLoop™	Hampton (Aliso Viejo, US)
CrystalCap HT™ Vial	Hampton (Aliso Viejo, US)
CrystalWand Magnetic™	Hampton (Aliso Viejo, US)
Magnetic caps, vials and pins	Molecular Dimensions (Newmarket, UK)
Vial Tongs/Clamp	Molecular Dimensions
Micro Tool Box	Molecular Dimensions
Foam Dewars	Spearlab (San Francisco, US)
Taylor-Wharton CX100/HC20 cryo tank	tec-lab (Idstein, DE)

Electrophoresis and Blotting

Chamber and tray	Appligene (n.a.)
Electrophoresis Power Supply EPS 600	Pharmacia Biotech (Uppsala, SE)
Mini PROTEAN® Tetra Cell	BioRad (Hercules, US)
Fast Blot B44	Biometra (Göttingen, DE)

G:box for gel imaging   Syngene (Cambridge, UK)

Digital Graphic Printer UP-D897   Sony (Minato, JP)

Additional Equipment

Ultraspec 10 Cell Density Meter   Amersham Biosciences

                                                         (Uppsala, SE)

NanoPhotometer^{TM} Pearl   Implen (München, DE)

inoLab® pH 720 pH-meter   WTW (Weilheim, DE)

SenTix® 81 pH-electrode   WTW (Weilheim, DE)

Incubator Multitron 2   INFORS HT (Bottmingen, CH)

Incubator Innova^{TM} 4230   NBSC (Edison, US)

Thermomixer comfort   Eppendorf (Hamburg, DE)

Techne Dri-Block DB 2A   Bibby Scientific (Stone, UK)

MR Hei-Standard magnetic stirrer   Heidolph (Schwabach, DE)

EQUIBIO Easyject Optima electroporator   peqlab (Erlangen, DE)

MyCycler^{TM} thermal cycler   BioRad (Hercules, US)

petriturn-E   schuett-biotec (Göttingen, DE)

AXIO Scope.A1 microscope/manipulator   Carl Zeiss (Oberkochen, DE)

Vacuum pump   vacuubrand (Wertheim, DE)

Branson Digital Sonifier 250   G.Heinemann

                                                        (Schwäbisch Gmünd, DE)

Laboklav 25/195   SHP Steriltechnik

                                                     (Magdeburg, DE)

CL-1000 UV Crosslinker   UVP (Upland, US)

4.1.7 Computer Software

Adobe Photoshop CS4   Adobe (San Jose, US)

Adobe Acrobat 9 Pro   Adobe (San Jose, US)

Microsoft Office 2007   Microsoft (Redmond, US)

EndNote Web   myendnoteweb.com

UNICORN^{TM} control software   GE Healthcare

XDS Program Package   MPI (Heidelberg, DE)

PHASER   www.phaser.cimr.cam.ac.uk

SHARP   www.globalphasing.com

SHELXC/D/E   http://shelx.uni-ac.gwdg.de

CCP4 Software Suite   www.ccp4.ac.uk

REFMAC   www.ccp4.ac.uk

MAIN   http://bio.ijs.si/sbl

PyMOL   www.pymol.org

MolScript/Bobscript   www.avatar.se/molscript

GRASP   honiglab.cpmc.columbia.edu

4.2 Organisms and Cultivation

4.2.1 Strains

The following bacterial strains were used in this work (Table 1).

Strain	Genotype	Source
E. coli XL1 Blue	*recA1 endA1 gyrA96 thi-1 hsdR17 supE44 relA1 lac* [F' *proAB lacI^{q}ZΔM15* Tn*10* (Tet^r)]	Stratagene (La Jolla, US)
E. coli BL21 DE3	F$^-$ *ompT hsdS*$_B$(r$_B$$^-$ m$_B$$^-$) *gal dcm* (DE3)	Novagen/Merck (Darmstadt, DE)

Table 1:

List of *E. coli* strains used in this work

The following yeast strains were used in this work (Table 2).

Strain	Genotype	Source
S. pombe Lindner var. *pombe*	*leu1*-32 *his5*-303	DSMZ 3796 (Braunschweig, DE)
S. pombe BG_0000H5	h$^-$, *ade6*-M210 *ura4*-D18 *leu1*-32	Bioneer (Daejeon, KR)
S. pombe BG_6129H	SPBC365.06Δ: kanMX4 h$^+$, *ade6*-M210 *ura4*-D18 *leu1*-32	Bioneer (Daejeon, KR)
S. pombe BG_1771H	SPAC521.02Δ: kanMX4 h$^+$, *ade6*-M210 *ura4*-D18 *leu1*-32	Bioneer (Daejeon, KR)
S. pombe BG_4334H	SPCC1442.07cΔ: kanMX4 h$^+$, *ade6*-M210 *ura4*-D18 *leu1*-32	Bioneer (Daejeon, KR)

Table 2:

List of *S. pombe* strains used in this work

4.2.2 Media

The following media were prepared for the cultivation of *E. coli*.

LB$_0$:	Peptone	10 g/L
	Yeast extract	5 g/L
	Sodium chloride	5 g/L
	(Agar	20 g/L; optional)

Antibiotic concentrations used for the cultivation of *E. coli*.

Ampicillin:	100mg/L or 180mg/L
Kanamycin:	50mg/L

The following media were prepared for the cultivation of *S. pombe*.

YES:	Yeast extract	5 g/L
	Glucose	30 g/L
	Adenine-Hemisulfate	225 mg/L
	Histidine	225 mg/L
	Leucine	225 mg/L
	Uracil	225 mg/L
	Lysine-Hydrochloride	225 mg/L
	(Geneticin Disulfate Salt	200 mg/L; optional)
	(Agar	20 g/L; optional)

ME:	Malt extract	30 g/L
	Glucose	30 g/L
	Adenine-Hemisulfate	225 mg/L
	Histidine	225 mg/L
	Leucine	225 mg/L
	Uracil	225 mg/L
	Agar	20 g/L
	pH	5.5 (NaOH)

4.2.3 Cultivation and Storage of *E. coli*

E. coli strains were streaked on agar plates containing the appropriate antibiotic with a sterile inoculation loop. Plates were incubated at 37 °C for 16 to 18 hours and kept at 4 °C in the fridge for short term storage. Precultures were inoculated from single colonies on the plate into liquid medium containing the appropriate antibiotic. Depending on the volume of the main culture, preculture volumes ranged from 30 to 500 mL. Preculture flasks were put in an incubator shaker at 37 °C. Growth of *E. coli* was monitored photometrically at a wavelength of 600 nm. An OD_{600} of 1 roughly equals 10^9 cells/mL. For long term storage, 2 mL of a stationary culture were centrifuged for 5 minutes at 2500 rcf. The pellet was resuspended in 1 mL of LB_0 containing 30 % glycerol, transferred in a cryo tube, shock frozen in liquid nitrogen and stored at -80 °C.

4.2.4 Cultivation and Storage of *S. pombe*

S. pombe strains were streaked on agar plates containing Geneticin if required with a sterile inoculation loop. Plates were incubated at 30 °C for 3 to 4 days and kept at 4 °C in the fridge for short term storage. Precultures were inoculated from single colonies on the plate into liquid medium. The preculture volume was 30 mL. Preculture flasks were put in an incubator shaker at 30 °C. Growth of *S. pombe* was monitored photometrically at a wavelength of 600 nm. An OD_{600} of 1 roughly equals 1.5×10^7 cells/mL. For long term storage, 4 mL of a stationary culture were centrifuged for 5 minutes at 2500 rcf. The pellet was resuspended in 1 mL of YES containing 30 % glycerol, transferred in a cryo tube, shock frozen in liquid nitrogen and stored at -80 °C.

4.3 Molecular Cloning with *E. coli*

4.3.1 Primers

The following primers were used for cloning (Table 3).

Primer Name	Sequence (5' → 3')
Wss1_Sc_for	CTAGGATCCAAGACAGAAGGAATAAAAAGCC
Wss1_Sc_rev	CTACTGCAGTTACCAGCGATCATCTCTATATC
Wss1_Sc_dom_for_1	CTAGGATCCCACATTCAAAAAGTGGCTGTTTTG
Wss1_Sc_dom_rev_1	CTACTGCAGTTATTGTTCAATAACCCATTGCCTTC
Wss1_Sc_dom_rev_2	CTACTCGAGTTATTGTTCAATAACCCATTGCCTTC
Wss1_oSS_Sp_for	CTAGGATCCTTTATATCTGCTATAAAAGGAGATTTC
Wss1_oSS_Sp_rev	CTACTGCAGTTATTCTACTACGAAATAGTTTTCC
Wss1-oSS_Sp_FWk	CTAGGATCCAAAATAGGATTTATATCTGCTATAAAGGAGATTTC
Wss1-oSS_Sp_RVk	CTACTGCAGTTAGGCGTAAAGAGCAATCA
SpWss1a_RVk2	CTACTCGAGTTAGGCGTAAAGAGCAATCA
Wss1_Sp_for	CTAGGATCCGAGTTGAAATTTAGTTGCAGAGG
Wss1_Sp_rev	CTACTGCAGTTACTCCTTTTGGACTTTACTACC
Wss1_domain_Sp_for	CTAGGATCCGCAAGTATATACACATTTAATGAACTTG
Wss1_UBQ_Sp_rev	CTACTGCAGTTATCTAATTAGACACATAATCTTCGATTC
Wss1_UBQ_Sp_RV2	CTACTGCAGTTACAAGCTGTATGTATTCGTGCTATAATC
Wss1_dom_Sp_for_2	CTAGGATCCATATACACATTTAATGAACTTGTGGTTTTAG
Wss1_dom_Sp_rev_2	CTACTGCAGTTACAAATCTGCTGCATCTGC
Wss1_dom_Sp_rev_3	CTACTCGAGTTACAAATCTGCTGCATCTGC
Wss1_dom_Sp_for_4	GCTAGGTCTCGGATCCATGTCGGACTCAGAAGTCAATC
Wss1_Sp_rev_2	CTACTCGAGTTACTCCTTTTGGACTTTACTACC
Sp_Wss1b_E203Q_FW	GTACATTAATTCACCAATTGACGC
Sp_Wss1b_E203Q_RV	GCGTCAATTGGTGAATTAATGTAC

Table 3:

Primers used for cloning in this work.

For both *Ostreococcus* constructs, synthetic genes were purchased from Mr.
Gene (http://mrgene.com/legal) with optimized *E. coli* codon usage.

4.3.2 Plasmids

The following plasmids were created (Table 4).

Plasmid and Insert	Restriction Sites
pRSETA His Tev Wss1 O.lucimarinus	BamHI / PstI
pRSETA His Tev Wss1 O.tauri	BamHI / PstI
pRSETA His Tev Wss1 S.cer	BamHI / PstI
pRSETA His Tev Wss1-oSS S.pombe a	BamHI / PstI
pRSETA His Tev Wss1 UBQ-Wss1 S.pombe b	BamHI / PstI
pRSETA His Tev Wss1 UBQ-Domäne S.pombe b	BamHI / PstI
pRSETA His Tev Wss1-Domäne S.pombe b	BamHI / PstI
pRSETA GST Tev Wss1 O.lucimarinus	BamHI / PstI
pRSETA GST Tev Wss1 O.tauri	BamHI / PstI
pQE30 His Wss1 S.c.	BamHI / PstI
pQE30 His Wss1 S.p.a	BamHI / PstI
pQE30 His Wss1 S.p.b	BamHI / PstI
pQE30 His Tev Wss1 S.c.k	BamHI / PstI
pQE30 His Tev Wss1 S.p.ak	BamHI / PstI
pQE30 His Tev Wss1 S.p.bk	BamHI / PstI
pRSETA GST PP Wss1 S.c.k	BamHI / PstI
pRSETA GST PP Wss1 S.p.ak	BamHI / PstI
pQE30 His Tev S.p.Wss1a k	BamHI / PstI
pQE30 His Tev S.p.Wss1b UBQ	BamHI / PstI
pQE30 His Tev S.p.Wss1b UBQk	BamHI / PstI
pQE30 GST PP S.c.Wss1	BamHI / PstI
pQE30 GST PP S.c.Wss1k	BamHI / PstI
pQE30 GST PP S.p.Wss1a	BamHI / PstI
pQE30 GST PP S.p.Wss1ak	BamHI / PstI
pQE30 His Tev S.p.Wss1bf	BamHI / PstI
pRSETA GST Tev S.p.Wss1bk	BamHI / PstI
pQE30 His S.p.Wss1b E203Q	BamHI / PstI
pET28b SUMO Ser S.c.Wss1k	BamHI / XhoI
pET28b SUMO Ser S.p.Wss1ak	BamHI / XhoI
pQE30 His Tev S.p.Wss1b E203Q	BamHI / PstI

pQE30 His Tev S.p.Wss1bk E203Q	BamHI / PstI
pET28b SUMO Ser S.c.Wss1k E116Q	BamHI / XhoI
pET28b SUMO Ser S.p.Wss1ak E118Q	BamHI / XhoI
pET28b SUMO Ser S.p.Wss1bk	BamHI / XhoI
pET28b SUMO Ser S.p.Wss1bk E203Q	BamHI / XhoI
pRSETA GST Tev SUMO S.p.Wss1bk	BsaI / BamHI / PstI
pET28b SUMO Ser SpWss1bf	BamHI / XhoI

Table 4:
Plasmids created in this work.

4.3.3 Solutions

TAE (50x):	Tris/Acetate pH 8.2	2 M
	EDTA	0.1 M
DNA loading dye (10x):	Tris/HCl pH 8.2	10 mM
	EDTA	1 mM
	Glycerol	50 % (v/v)
	Bromophenol blue	0.25 % (w/v)
	Xylene cyanole	0.25 % (w/v)
Agarose solution:	Agarose	0.5 g
	TAE (1x)	50 mL
EtBr solution:	Ethidium bromide	1 mg/L

For molecular cloning sterile material and solutions were utilized. If not stated otherwise, work was performed at room temperature.

4.3.4 Preparation of genomic DNA from *S. pombe*

A stationary overnight culture (10 mL) was harvested for 5 minutes at 3500 rcf and 4 °C. The pellet was washed with 1 mL of sterile ddH$_2$O, resuspended in 500 µL lysis buffer (100 mM Tris/HCl pH 8.0; 50 mM EDTA; 1 % SDS (w/v)), and approximately 400 µL glas beads were added. After 2 minutes of vigorous vortexing, the sample was chilled on ice until the beads had sedimented. The supernatant was transferred to a fresh tube and 275 µL of a 7 M ammonium acetate solution (pH 7.0) were added. The sample was incubated for 5 minutes at 65 °C, and subsequently cooled on ice for 5 minutes. Proteins were precipitated by adding 500 µL of chloroform (fume hood!) and by mixing the aqueous and the organic phases. The emulsion was centrifuged for 2 minutes at 13000 rcf, and the supernatant (aqueous phase) was transferred to a fresh tube. DNA was precipitated by adding 1 mL of isopropanol. The sample was incubated for 5 minutes at room temperature and subsequently spun down for 5 minutes at 13000 rcf. The pellet was washed with 200 µL of 70 % ethanol and dried afterwards. Finally, the DNA pellet was dissolved in 45 µL of sterile ddH$_2$O and 5 µL of RNAse A (25 mg/mL). RNA was digested for 15 minutes at 37 °C.

Genomic DNA from *S. cerevisiae* was prepared by Kathrin Gärtner (technician).

4.3.5 PCR Amplification

PCR was applied to selectively amplify DNA segments from coding regions of genomic DNA or plasmids. Genomic DNA template was used undiluted, whereas plasmid DNA template was diluted 1:10 in sterile ddH$_2$O. Primers were designed to have a melting temperature between 50 °C and 60 °C. The melting tempera-

ture was calculated with the help of the online OligoAnalyzer 3.1 by IDT (http://eu.idtdna.com/analyzer/Applications/OligoAnalyzer/). Generally, the following standard mixture was used:

PCR mix:	sterile ddH$_2$O	add to 100 µL
	Phusion® buffer (5x)	20 µL
	dNTP mix (50x)	2 µL
	template DNA	1 µL
	primer stock solution	1 µL each
	Phusion® polymerase	1 µL

The PCR sample was mixed with a pipette. The settings of the following thermal cycler program were adjusted according to the length of the desired DNA fragment and the melting temperature of the primers.

Initial denaturation:	95 °C / 3 min	1x
Cyclic denaturation:	95 °C / 30 sec	
Cyclic annealing:	50 °C / 30 sec	35x
Cyclic elongation:	72 °C / 45 sec	
Final elongation:	72 °C / 10 min	1x
Cooling:	4 °C / ∞	

PCR results were analyzed by agarose gel electrophoresis.

4.3.6 Preparation of Plasmid DNA from *E. coli*

For analytical preparation of plasmid DNA the peqGOLD Plasmid Miniprep Kit I was utilized, for preparative purposes Kit II was applied. DNA was purified according to the manufacturer's protocol.

4.3.7 Agarose Gel Electrophoresis

Both analytical and preparative separations of DNA were carried out in 1 % (w/v) agarose gels. Electrophoresis was performed for about 40 minutes in 1x TAE running buffer with a constant voltage of 120 V. The gel was stained for 30 minutes in an ethidium bromide solution and the bands were visualized with the help of the G:Box detection system (365 nm). The molecular weight standard was a DNA Ladder-Mix (100 - 10000 bp).

4.3.8 DNA Isolation from Agarose Gels

The desired DNA bands were excised from the gel using a scalpel under UV light exposure (365 nm; eye protection!). The agarose piece was treated with the peqGOLD Gel Extraction Kit according to the manufacturer's protocol.

4.3.9 Purification of DNA

DNA fragments and plasmids were purified with the peqGOLD Cycle-Pure Kit according to the manufacturer's protocol. Purified DNA was stored at -20 °C.

4.3.10 DNA Restriction

Restriction digests were carried out for both analytical and preparative purposes.

In general, the following standard mixtures were prepared:

Analytical mix:	sterile ddH$_2$O	add to 10 µL
	desired DNA	3 µL
	appropriate NEB buffer (10x)	1 µL
	BSA (1 mg/mL, 10x)	1 µL (optional)
	NEB enzyme A	0.5 µL
	NEB enzyme B	0.5 µL

Depending on the sample number, a master mix without the desired DNA was set up. Analytical samples were mixed with a pipette, incubated for 1.5 hours at the respective temperature and subsequently mixed with 1 µL DNA loading dye for electrophoresis.

Preparative mix:	sterile ddH$_2$O		add to 70 µL
	desired DNA,	either	40 µL (PCR product)
		or	8 - 15 µL (plasmid)
	appropriate NEB buffer (10x)		7 µL
	BSA (1 mg/mL, 10x)		7 µL (optional)
	NEB enzyme A		2 µL
	NEB enzyme B		2 µL

Preparative samples were mixed with a pipette, incubated for 3 hours at the respective temperature and subsequently purified.

4.3.11 Ligation of DNA fragments

Standard ligation mixtures contained approximately 50 ng of DNA, with a molar ratio between plasmid DNA and PCR product ranging from 1:1 to 1:3. The following mixture was usually prepared:

Ligation mix:	sterile ddH$_2$O	add to 7.5 µL
	plasmid DNA	1 µL
	PCR product	5 µL

This mixture was incubated at 55 °C for 10 minutes and then chilled on ice for 5 minutes. After that, 2 µL of T4-Ligase buffer (5x) and 0.5 µL of T4-Ligase were added and the whole sample was gently mixed. After 2 hours of incubation at room temperature, the ligation was ready for transformation of *E. coli*.

4.3.12 Transformation of *E. coli*

Transformation of *E. coli* cells was carried out by electroporation. Electro-competent cells had been prepared by the technician Kathrin Gärtner using standard procedures. The competent cells (40 µL) were thawed on ice, mixed with 1 µL of the respective ligation mixture and afterwards transferred to a precooled electroporation cuvette. A pulse was performed in an electroporation device according to the manufacturer's instructions (EQUIBIO). Cold SOC-Medium (1 mL; see below) was immediately added to the cells in the cuvette and cells were gently resuspended. The suspension was transferred to a reaction tube and incubated at 37 °C for 1 hour. Finally, cells were plated on the appropriate selective agar medium.

SOC medium:	Yeast Extract	5 g/L
	Peptone	20 g/L
	Sodium chloride	10 mM
	Potassium chloride	2.5 mM
	Magnesium chloride	10 mM
	Magnesium sulfate	10 mM
	Glucose	20 mM

4.3.13 DNA sequencing

All new constructs were sequenced by GATC Biotech (Konstanz, DE) before their further use. To this end, 15 µL of the respective plasmid DNA were mixed with an equal volume of sterile ddH$_2$O. Sequencing results were verified by comparison with the corresponding database entries (http://www.uniprot.org/).

4.4 *S. pombe* Genetics and Phenotype Analysis

4.4.1 Strain Crossing

Relevant *S. pombe* strains were purchased from Bioneer Corporation (see chapter 4.2.1). Haploid *S. pombe* strains of different mating types were crossed by the following procedure. Using a sterile toothpick, a visible glob of cells from strain 1 was taken and a small patch on a ME mating plate was made (5 mm in diameter). With a second sterile toothpick, an equivalent amount of strain 2 was taken and added to the previous patch. After adding 5 µL of sterile ddH$_2$O, strains were mixed gently on the surface of the agar with a third sterile toothpick.

The ME plate was incubated at 25 °C for 3 to 4 days and formation of asci was monitored microscopically.

4.4.2 Tetrad Analysis

A mating/sporulation plate which had been grown for 3 to 4 days at 25 °C was examined under a microscope to identify ripe asci, which were still intact but had clearly distinguished spores. If necessary, cells in the mating patch were spread along the agar with a sterile toothpick to make them more apparent. With the help of a second sterile toothpick, cells were transferred and laid across a YES plate upon which dissection would be performed. The following steps were carried out on a micromanipulator. Upon identification of a ripe intact ascus, a dissecting needle was used to manipulate the ascus to fixed position on the plate. Each additional ascus was placed 0.5 cm to one side of the preceding tetrad. The plate was then incubated at 35 °C to 36 °C for 4 to 5 hours to stimulate ascus breakdown. Upon returning the plate to the micromanipulator, tetrads that have popped by the four free spores were identified. Occasionally, gentle tapping of the dissecting needle helped to breakdown the ascus. Finally, the four free spores of a tetrad were linearly moved down the plate. Once a plate had been completed, it was incubated at 30 °C for 4 to 6 days, until individual colonies could be observed.

4.4.3 Mating Type Testing

When fission yeast cells complete meiosis and sporulation, they produce starch that can be stained easily by exposure to iodine vapor. However, iodine vapor

kills the cells, so this method cannot be used if further analysis of the meiotic products is required. The following protocol was applied: Known h^+ and h^- tester strains were patched vertically on a first YES plate, whereas the uncharacterized strains were patched horizontally on a separate YES plate. The 2 plates were incubated at 30 °C until all patches were grown up (1 to 2 days). The patches of both plates were replica plated onto a ME mating plate so that patches of tester strains and unknowns intersected. The ME plate was then incubated at 25 °C for 3 to 4 days. An iodine plate was prepared by scattering few iodine crystals on the lid of an empty petri dish in a fume hood. The lid of the ME plate was removed and the ME plate was inverted over the iodine crystals. The ME plate was incubated for 5 to 10 minutes until the positive control became dark brown where the streak intersected the tester strain of the opposite mating type. The mating type of an uncharacterized strain was determined by identifying the junctions in which a strain of known mating type had generated a dark patch with the strain being tested.

4.4.4 Phenotype Analysis

Disruption mutants of *S. pombe* were examined for their sensitivity to certain environmental stimuli by the following plate assay. YES medium (20 mL) was inoculated with a single colony of the respective strain and incubated overnight at 30 °C. Once an OD_{600} of 0.2 to 0.5 was reached, equal cell amounts were harvested by centrifugation at 5000 rcf and 20 °C for 2 minutes. For *S. pombe* an OD_{600} of 0.25 roughly equals 0.5×10^7 cells/mL and linearity is assumed to be valid up to an OD_{600} of 0.5. Before resuspending, fresh YES medium was added to each cell pellet to a final total volume of 1 mL. After resuspending the cells, a

dilution series was pipetted on a plane YES plate. Droplets were dried, the respective stimulus was applied and plates were incubated at the desired temperature for 3 to 5 days.

4.5 Heterologous Gene Expression with *E. coli*

4.5.1 Expression Tests

Expression tests were carried out prior to large scale cultivations in order to optimize the amount of solubly produced protein. To this end, prewarmed LB medium (30 mL, 37 °C) containing the respective antibiotic was inoculated with 600 µL of a stationary overnight culture of the desired *E. coli* expression strain. This main culture was then grown to an OD_{600} of 0.5 to 0.7. At this stage, a sample (1 mL) was taken from the culture, the temperature of the culture was adjusted in a cold (4 °C) water bath (optional) and IPTG was added to a final concentration of 0.5 mM to 1 mM. Further samples were taken from the culture every hour and analyzed by SDS-PAGE (see chapter 4.7.2). To this end, fresh samples were spun down for 1 minute at 13000 rcf, and the pellet was resuspended in 1 mL of TBS-buffer (100 mM Tris/HCl pH 8.0; 500 mM NaCl). Cells were disrupted with the help of an ultrasonication device (amplitude: 20 %; time: 10 sec; pulse time: 0.5 sec; pause: 0.5 sec; 2 repetitions; cooling on ice). A sample (50 µL) was taken from the lysed cells and mixed 1:1 with SDS loading buffer (see chapter 4.7.1). The lysate was centrifuged for 10 minutes at 13000 rcf. Another sample (50 µL) was taken from the supernatant and mixed 1:1 with SDS loading buffer. The samples were boiled for 10 minutes at 95 °C and subsequently examined by SDS-PAGE (see chapter 4.7.2).

4.5.2 Large Scale Gene Expression

After identification of ideal conditions for the expression of the target gene, large scale cultivations were performed in order to produce high protein quantities. Depending on the results of the expression tests, either *E. coli* XL1 blue or *E. coli* BL21 (DE3) strains were used. Prewarmed LB medium (3 L to 9 L, 37 °C) containing the respective antibiotic was inoculated with 1:50 volume of a stationary overnight culture of the *E. coli* expression strain. This main culture was then grown to an OD_{600} of 0.5 to 0.7. At this stage, the temperature of the culture was adjusted in a cold water bath (optional) and IPTG was added to a final concentration of 0.5 mM to 1 mM. Expression was stopped at the optimal time determined by the expression tests and cells were harvested by centrifugation for 30 minutes at 5500 rcf and 4 °C.

4.5.3 Large Scale Cell Disruption

Prior to purification of the recombinantly produced proteins, cells had to be disrupted. For this purpose, cell pellets were resuspended to homogeneity in lysis buffer, which usually was buffer A of the first chromatography step supplemented by a small amount of DNAse I (AppliChem, Darmstadt, DE) and Pefabloc SC protease inhibitor (Roche, Risch, CH). The suspension was transferred to a special rosette jar, which allows efficient cooling in an ice bath. Cells were lysed with the help of an ultrasonication device (amplitude: 80 %; time: 3.5 min; pulse time: 1.0 sec; pause: 1.0 sec; cooling in ice bath). To clear the lysate it was centrifuged for 30 minutes at 40000 rcf and 4 °C. The supernatant was then used for protein purification.

4.6 Protein Purification

4.6.1 Affinity Chromatography

Solutions

Buffer A:	Tris/HCl pH 8.0	100 mM
	Sodium chloride	500 mM
	Imidazole	20 mM
Buffer B:	Tris/HCl pH 8.0	100 mM
	Sodium chloride	500 mM
	Imidazole	500 mM

Procedure

Protein purifications were carried out on the respective chromatography platforms (ÄKTA^{TM}). For this purpose, the supernatant originating from the preceding large scale cell disruption (see chapter 4.5.3) was loaded on a HisTrap^{TM} FF Ni-NTA column, in case of a His-tagged target protein. After that, the column was washed with buffer A until the baseline of UV-absorption was reached. Finally, the protein was eluted by applying a linear gradient with a final concentration of 100 % buffer B. Fractions were collected according to the course of the UV-chromatogram. Relevant fractions were analyzed by SDS-PAGE (see chapter 4.7.2). For GST-tagged proteins, a self packed Glutathione Sepharose column was employed and buffer A was prepared without Imidazole, whereas buffer B contained 10 mM reduced glutathione instead of imidazole.

4.6.2 Desalting

After the first purification step (see chapter 4.6.1), fractions containing the target protein were united and subsequently dialysed by passing the fraction pool through a HiPrep 26/10 desalting column. The desalting buffer usually consisted of 10 mM Tris/HCl pH 8.0 and optionally low salt concentrations (10 mM to 50 mM NaCl). Fractions were collected according to the course of the UV-chromatogram.

4.6.3 Tag Removal

In order to increase the crystallization tendency of the target protein, the affinity tag was removed by enzymatic digestion. To this end, the respective protease (either TEV- or SUMO-protease) was added to the dialysed target protein in a mass ratio of 1:100, 1:50 or 1:10. Both proteases had been prepared by the technician Kathrin Gärtner using standard procedures. Tag cleavage was performed at either 20 °C or 4 °C for several days, depending on the cutting velocity. Cleavage efficiency was monitored by taking 2 samples per day, followed by SDS-PAGE analysis. Occasionally occurring precipitate was removed by either centrifugation for 3 minutes at 13000 rcf and/or by sterile filtration. For removal of the protease, the cleaved His-tag and the uncleaved target protein, the sample was passed through another chromatographic column, yielding the cleaved target protein in the flowthrough.

4.6.4 Gel Filtration

In order to increase protein purity, gel filtration was optionally applied as a final purification step, and depending on the required separation range, either a Superdex^{TM} 75 or Superdex^{TM} 200 column was used. The running buffer usually consisted of 50 mM Tris/HCl pH 8.0 and 200 mM NaCl. Fractions were collected according to the course of the UV-chromatogram and protein purity was analyzed by SDS-PAGE (see chapter 4.7.2).

4.6.5 Concentration of Proteins

Crystallization trials require high protein concentrations ranging from approximately 5 mg/mL to more than 100 mg/mL. Thus, the target protein was concentrated either using Amicon stirred cells or Amicon Ultra centrifugal filters. For large sample volumes stirred cells were utilized, which are operated at a nitrogen gas pressure of approximately 5 bar. In order to concentrate protein solutions with less than 15 mL volume, centrifugal filters were applied by centrifuging the respective sample at 4000 rcf and 4°C until the desired concentration was reached. Depending on the size of the target protein, filter membranes with different molecular weight cutoff were employed (3 kDa, 5 kDa or 10 kDa). Intermediate mixing by gentle pipetting prevented protein aggregation at the filter membrane surface.

4.7 Protein Analytics

4.7.1 Solutions

SDS loading buffer:	Tris/HCl pH 6.8	60 mM
	Glycerol	30 % (v/v)
	Sucrose	10 % (w/v)
	SDS	5 % (w/v)
	2-Mercaptoethanol	3 % (v/v)
	Bromophenol blue	0.02 % (w/v)
Stacking gel buffer:	Tris/HCl pH 6.8	500 mM
	SDS	0.4 % (w/v)
Separating gel buffer:	Tris/HCl pH 8.8	1.5 M
	SDS	0.4 % (w/v)
SDS running buffer:	Tris/HCl pH 8.3	25 mM
	Glycine	200 mM
	SDS	0.1 % (w/v)
Gel staining solution:	Isopropanol	25 % (v/v)
	Glacial acetic acid	10 % (v/v)
	Coomassie Brilliant Blue R250	0.05 % (w/v)
Destainer:	Glacial acetic acid	10 % (v/v)
Transfer buffer:	SDS running buffer	800 mL
	Methanol	200 mL

Ponceau S solution:	Trichloroacetic acid	3% (w/v)
	Ponceau S	0.02 % (w/v)
TBS buffer:	Tris/HCl pH 7.2	50 mM
	Sodium chloride	150 mM
	(Tween 20	0.1 % (v/v), optional)
AP buffer:	Tris/HCl pH 9.6	100 mM
	Sodium chloride	100 mM
	Magnesium chloride	5 mM

4.7.2 SDS-PAGE

Discontinous SDS-Polyacrylamide gel electrophoresis (SDS-PAGE) was conduc-
ted to analyze cell lysates and protein extracts (Fling and Gregerson, 1986). The
separation takes place in a vertical gel which is put in an electrophoresis
chamber applying a constant current of 30 mA per gel for 45 to 60 minutes.
Before loading samples on the gel, 5 µL to 15 µL of the protein solution had been
mixed with 5 µL of the SDS loading buffer and subsequently boiled at 95 °C for
10 minutes. For ordinary SDS gels a Roti$^{®}$-Mark STANDARD molecular weight
marker was used. SDS gels for Western blotting were loaded with a prestained
marker.

4.7.3 SDS Gel Staining

In order to visualize proteins after SDS-PAGE, gels were stained by putting them
into approximately 100 mL of a Coomassie staining solution for 30 minutes. After
pouring off the staining solution, the gel was washed once with dH$_2$O and put into

approximately 100 mL of destaining solution. Fresh destaining solution was added after 30 minutes. After another approximately 45 minutes protein bands were visible.

4.7.4 Determination of Protein Concentration

The concentration of protein solutions was determined by UV spectroscopy on a NanoPhotometer^{TM}. The molar extinction coefficient of the desired protein, which was computed with the ProtParam tool (http://web.expasy.org/protparam), allows calculation of the protein concentration applying the Lambert-Beer law. The UV absorption of the protein was measured at 280 nm.

4.7.5 Western Blot (Immunoblotting)

Proteins that had been separated by SDS-PAGE were transferred to a membrane by the following procedure. The SDS-PAGE gel, a nitrocellulose membrane and 6 Whatman filter papers were soaked in transfer buffer for 5 minutes. After that, a stack was formed with 3 Whatman papers at the bottom, the nitrocellulose membrane and the SDS gel in the middle and three Whatman papers on the top. This stack was clamped in the blotting device and the transfer was performed at 100 mA per gel for 1 hour. Blotting quality was controlled by Ponceau S staining of the membrane. The membrane was blocked in 10 mL TBS-Tween20 supplemented with 5 % milk powder (milk solution) for 45 minutes (optionally overnight). The primary antibody (3 µL) was diluted in fresh milk solution (10 mL) and this mixture was added to the membrane without discarding the first milk solution. After shaking for 45 minutes (or overnight), the membrane

was washed 6 times for 5 minutes each with 10 mL TBS-Tween20. Next, the membrane was incubated with the secondary antibody fused to alkaline phosphatase (AP). This antibody had also been diluted in milk solution (2 µL antibody in 10 mL milk solution). After 45 minutes of shaking, the membrane was washed 3 times for 5 minutes each with 10 mL TBS-Tween20 and then 3 times for 5 minutes each with 10 mL pure TBS buffer. Target bands were detected by a chromogenic reaction, catalyzed by AP. To this end, 66 µL NBT and 33 µL BCIP were diluted in 10 mL AP buffer and added to the membrane, discarded again as soon as bands appeared, and finally the membrane was washed with dH_2O.

4.8 Protein Crystallization and Structure Determination

4.8.1 Protein Crystallization

Proteins of all projects have been crystallized according to the following protocol. Highly concentrated protein solutions were used for initial screens of crystallization condition, which were performed on a Phoenix robot in the 200 nL scale. Buffers of the respective protein crystallization screening suite (Qiagen) were transferred on a 96-well format microplate at 20 °C and 70 % humidity. The protein was added likewise so that droplets consisted of 1 volume buffer and either 1, 2 or 3 volumes of protein solution. Plates were hermetically sealed immediately with a transparent plastic foil and stored at 20 °C. Thus, crystals grew by the sitting drop vapor diffusion method within several weeks or months, and crystal formation was periodically monitored with a stereo microscope. Initial hit conditions were optimized either on a MICROLAB® STARlet robot, using 96-well format microplates (sitting drop) or manually, utilizing pregreased 24-well

plates sealed by glass cover slides (hanging drop). In the latter case droplets were pipetted in the 2 μL scale.

4.8.2 Data Collection and Processing

For all projects optimization of cryo buffers for subsequent shock freezing of crystals in a stream of nitrogen gas at 100 K, as well as initial X-ray diffraction analysis and native data collection were carried out on the X8 PROTEUM in-house generator, featuring a MICROSTAR microfocus CuKα rotating anode X-ray source, a PLATINUM[135] CCD detector and a 4-cirlce KAPPA goniometer. Diffraction images were collected using 0.5 ° rotations per frame and processing was performed using the PROTEUM2 software suite.

In addition to in-house collection of native data sets for the Wss1-project, both high resolution native and anomalous data sets (single wavelength anomalous dispersion, SAD) were recorded at the beamlines of the Swiss Light Source (SLS, Paul Scherrer Institut, Villigen, CH). Fluorescence energy scans for different Wss1-crystals identified Ni as anomalous scatterer. Anomalous data sets were obtained both at the peak and the inflection point of the respective absorption edge (Ni: 1.49 Å). SLS data were processed applying programs included in the CCP4 software suite (Collaborative Computational Project, 1994) and XDS (Kabsch, 2010).

4.8.3 Structure Determination, Model Building and Refinement

For structure determination of Wss1 the site of the anomalous scatterer was computed with the program SHELX (Sheldrick, 2010). Heavy atom location allowed subsequent experimental phasing with SHARP (Bricogne et al., 2003). Solvent flattening using SOLOMON (Abrahams and Leslie, 1996) was performed for improving experimental phases of Wss1.

The crystal structures of both collaboration projects (FNR:Tic62 and Hsp17.7) were determined by molecular replacement employing the program PHASER (McCoy et al., 2007).

For all crystal structures water molecules were selected and placed with the help of ARP/wARP (Langer et al., 2008). Furthermore, all structures were refined with REFMAC (Murshudov et al., 1997; Vagin et al., 2004) and models were finalized in successive rounds using the interactive 3D graphic program MAIN (Turk, 1992).

4.8.4 Graphic Representations

Graphic representations of molecules were created by the programs MOLSCRIPT (Kraulis, 1991), BOBSCRIPT (Esnouf, 1997) and PyMOL (DeLano, 2002). Surface images were calculated and depicted with GRASP (Nicholls et al., 1991). Pictures were finally edited with Photoshop CS4 (Adobe).

5 Introduction to X-ray Crystallography of Proteins

Since the elucidation of the 3D structure of the DNA double helix (Watson and Crick, 1953) and the determination of the first protein structures of myoglobin (Kendrew et al., 1960) and hemoglobin (Perutz et al., 1960), X-ray crystallography has become an essential method in the fields of biology, chemistry and medicine over the past decades. The combination of structural and functional information of a protein allows investigations on the catalytic mechanism and the binding properties of ligands at the atomic level, and can thus be applied for the design of drugs and therapeutic agents. X-ray crystallography is based on the phenomenon that electromagnetic waves interfere with matter that means with molecules that are arranged in a 3 dimensional (3D), highly ordered, repeating pattern, termed as crystal. A crystal typically contains 10^{12} - 10^{14} molecules, resulting in a usual size of 100^3 - 200^3 μm^3. Crystal quality critically influences the course of structure determination, therefore the primary aim is to obtain good crystals.

5.1 Protein Crystals

In order to form a protein crystal, protein molecules must separate from solution and pack into a periodic crystal lattice (Rupp, 2010). Various methods for the generation of protein crystals have been reported up to now (Friedmann et al., 2011; McPherson, 1990; McPherson, 2004; Ochi et al., 2009), the most popular of which is the vapour diffusion method (Figure 1). With this technique, a precipitant is added to a protein solution with a defined concentration. A drop of this mixture is placed in a sealed well, containing the undiluted precipitant reservoir. Due to the lower precipitant concentration in the drop, water

evaporates from the drop into the reservoir, which causes a slow increase of the protein concentration in the drop until the solution gets supersaturated. Nucleation as well as phase separation occurs and crystals may start to grow (Rupp, 2010).
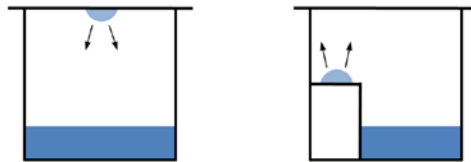
Figure 1:
Schematic representation of the vapor diffusion method, either as hanging drop (left) or as sitting drop (right). The small droplet consisting of protein and reservoir solution is put in vapour equilibrium with a high volume of the pure reservoir in a closed system. Due to water evaporation, the concentration of the solutes in the drop slowly increases until supersaturation is reached (Drenth, 2007).

A solubility diagram visualizes the phase transition behaviour of a protein as a function of the concentrations of the precipitant and the protein (Figure 2).

Crystal formation is influenced by many parameters such as temperature, protein purity, protein concentration, defined precipitants, buffers, pH and different salt concentrations. The protein crystals are rather loosely packed, owing to a usually high solvent content, ranging from 30 % to 90 %. Moreover, only few inter-molecular contacts are responsible for maintaining the crystalline state, thus protein crystals are very fragile.
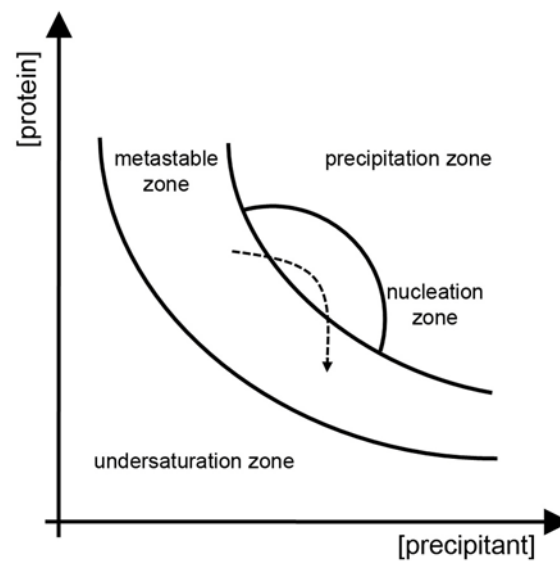
Figure 2:
Crystallization phase diagram. Starting from the undersaturation zone, the aim of any crystallization trial is for the system to enter the nucleation zone, such that nuclei form, and then to reenter into the metastable zone, so that nuclei can grow to crystals (Sherwood and Cooper, 2011).

The molecules in a crystal are arranged in a regular, periodic way, which manifests in the translation of the unit cell in each spatial direction. Each unit cell contains the same number of identically located atoms, hence dividing a crystal in repetitive, identical components. For the description of a whole crystal, it is therefore sufficient to characterize the unit cell. The latter is defined by the length of its 3 axes (a, b, c) and their angles (α, β, γ) to each other. The unit cell is generated by applying all symmetry operators of the respective crystallographic space group to the asymmetric unit, which is the smallest repetitive element of a crystal.

5.2 X-ray Diffraction

When electromagnetic waves such as X-rays encounter matter, their electric field vector interacts with the electron shell of atoms and the waves are being scattered. The radiation energy induces oscillations of the electrons, which therefore emit secondary waves on their part. Constructive interference can be observed, when waves are in phase, whereas phase shifts attenuate wave superposition, causing destructive interference. Hence, discrete scattering of X-rays on atoms arranged in periodic crystal lattice, a phenomenon termed as diffraction, can be observed, when all 3 Laue equations are satisfied simultaneously by a distinct value of the scattering vector Δk (Rupp, 2010). This vector describes the change in direction between the incident and the reflected wave, and the Laue equations define the diffraction conditions an all 3 spatial dimensions as follows (Sherwood and Cooper, 2011):

$$\Delta k \cdot a = h \cdot 2\pi\,; \qquad \Delta k \cdot b = k \cdot 2\pi\,; \qquad \Delta k \cdot c = l \cdot 2\pi$$

Diffraction on a periodic array of molecules in a crystal can be described by Bragg's law as reflection of X-rays on sets of parallel lattice planes (Rupp, 2010).

$$2d \cdot \sin\theta = n \cdot \lambda$$

For a given lattice plane spacing d, constructive interference occurs only under a defined incidence angle θ, resulting in integer multiples of the reflected wave $(n \cdot \lambda)$ (Figure 3). Thus, very close lattice planes effect high diffraction angles and vice versa.
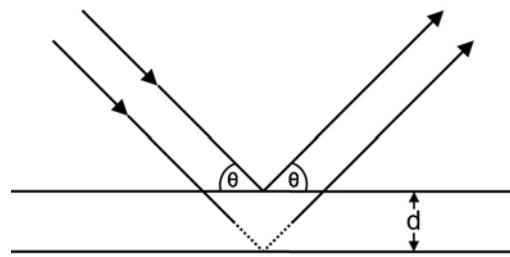
Figure 3:
Schematic illustration of Bragg's law. The dotted line represents the additional path length, that the second wave has to travel (Drenth, 2007).

Since the unit cell axes run parallel to the crystal axes, the lattice planes intersect the unit cell axes at the a/h, b/k and c/l coordinates. The integers h, k and l are designated as Miller indices (Sherwood and Cooper, 2011) and determine the spatial orientation of the respective lattice planes. Countless lattice planes virtually traverse the unit cell. Each of them has to be oriented relative to the incident wave in a way that Bragg's diffraction condition is met, in order to observe as much reflections as possible. Each set of parallel lattice planes can be represented by a perpendicular vector with the associated length d. Thus, each spot on the detector corresponds to the endpoint of the related d-vector.

Rearranging the Bragg equation reveals the inverse relationship between the diffraction angle θ and the lattice plane spacing d or the d-vector, respectively.

$$2 \cdot \sin \theta = \frac{n \cdot \lambda}{d} \Rightarrow \theta \sim \frac{1}{d}$$

Furthermore, the direction of the d-vector cannot easily be deduced, due to its reciprocal definition by the axial intercepts a/h, b/k and c/l. The introduction of reciprocal dimension facilitates this situation. So, the reciprocal axes a*, b* and

c* are defined by the cross product of the according real unit cell axes. To obtain

reciprocal length units, division by the unit cell volume V is necessary.

$$a* = \frac{b \times c}{V}; \quad b* = \frac{a \times c}{V}; \quad c* = \frac{a \times b}{V}$$

The axes a*, b*, c* span the reciprocal lattice and the reciprocal d*-vector is

defined by its coordinates h, k, l. The endpoints of all d*-vectors represents the

grid points of the reciprocal lattice. In general, the reciprocal axes are

perpendicular to the real lattice planes and vice versa.
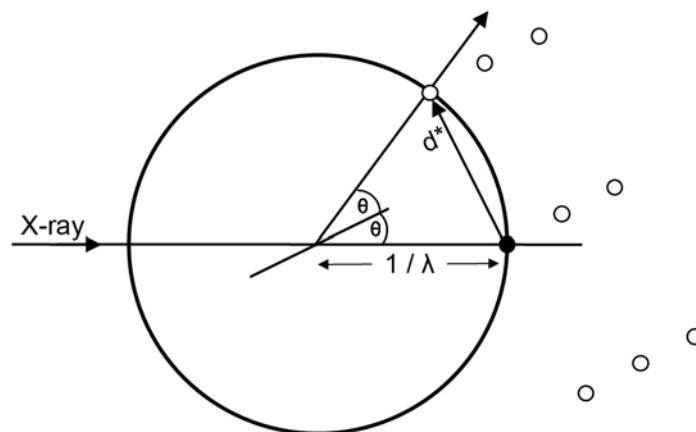
Figure 4:
The Ewald construction.

The Ewald construction illustrates Bragg's law by depicting the diffraction

condition both for the real and the reciprocal space at the same time (Figure 4).

When Bragg's law is fulfilled, the reflected beam occurs at an angle of 2θ relative

to the incident beam in real space. In reciprocal space, the same direction for the

reflection holds true and can be explained by the geometric connection between

θ and d*. The starting point of d* is located on the intersection of the elongated

incident beam and a sphere (Ewald sphere) around the crystal with a radius of $1/\lambda$. This point is also the origin of the reciprocal lattice. The endpoint of d* crosses the Ewald sphere in the corresponding reciprocal grid point and thus determines the direction of the reflection. Since a reciprocal plane which intersects the Ewald sphere yields several discrete reflections and since rotation of the crystal brings different planes into Bragg's law, a diffraction pattern, consisting of concentric spots, can be observed on a detector.

5.3 Crystal Symmetry

Besides their 3D periodic arrangement, most crystals also feature symmetry properties. Based on all distinguishable symmetry options, the following 7 crystal systems are defined for a translational lattice: triclinic, monoclinic, orthorhombic, tetragonal, trigonal, hexagonal and cubic. They differ in their specification of the respective unit cell parameters. The limits of a unit cell are usually given by the grid points, so the unit cell represents the smallest volume entity of the whole lattice, which is called primitive cell. In some cases it is more favourable for the description of symmetric properties, to expand the volume of the unit cell, resulting in so called centred cells that contain additional grid points. Thus, the 7 crystal systems can be subdivided into 14 Bravais lattices.

In general, all distinguishable combinations of the main symmetry operations such as mirroring, inversion and rotation can be categorized in 32 crystallo-graphic point groups. In addition, the application of translational elements (i.e. the combination of point groups with Bravais lattices) yields 230 possible space groups. Since mirroring and inversion change the handedness of a chiral

molecule, these operations are not allowed for proteins. Therefore, the available symmetry operations are restricted to plain rotation axes and screw axes. Required compatibility with translational periodicity of the lattice limits rotations and screw axes to 2-, 3-, 4- and 6-fold operations (Rupp, 2010). Hence, the 32 general point groups are reduced to 11 chiral ones and accordingly the number of 230 general space groups decreases to 65 chiral ones.

The unit cell is composed of the asymmetric unit, which is defined as the smallest possible set of atoms that can be used to generate the unit cell by applying all symmetry operations of the respective space group. When several identical molecules appear in the asymmetric unit, they are related by non-crystallographic symmetry (NCS), which can be useful information for structure determination. Detailed descriptions about crystal symmetry are provided by the International Tables for Crystallography.

5.4 Structure Factor and Electron Density

The structure factor F_{hkl} is a vector, describing the sum of the partial scattering contributions of all atoms j with their fractional coordinates x_j, y_j and z_j in the unit cell (Sherwood and Cooper, 2011).

$$F_{hkl} = \sum_j f_j \cdot e^{i \cdot 2\pi(hx_j + ky_j + lz_j)}$$

Thus, each atom contributes a scattered wave, which has the amplitude f_j and a phase of $2\pi(hx_j+ky_j+lz_j)$. (Figure 5) In the Argand diagram the amplitude is given by the absolute value of the vector length and the phase by the angle between the vector and the abscissa. Due to the additional phase information, the

scattered wave constitutes a complex number, recognizable by the introduction

of the imaginary exponent i.
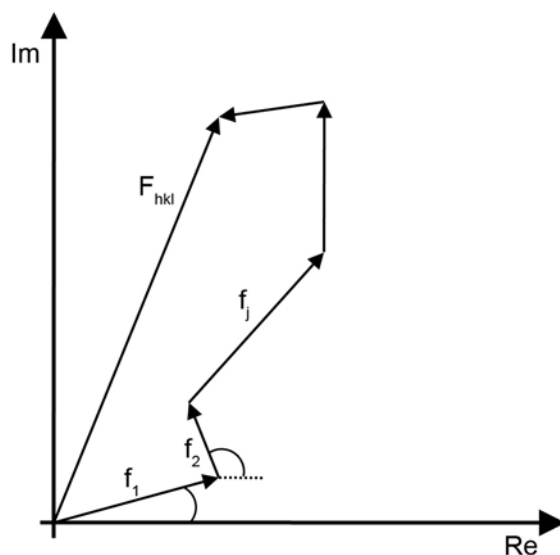
Figure 5:

Graphical representation of the structure factor in an Argand diagram. Each atom j in
the unit cell contributes a wavelet of amplitude f_j to the structure factor (Sherwood
and Cooper, 2011).

The atomic scattering factor f_j is directly proportional to the number of electrons,

but it declines with increasing diffraction angle. Displacement of the atoms from

their mean position, which results from thermal vibration as well as from disorder

in the crystal lattice, additionally reduces the amplitude of f_j (Rupp, 2010). The

Debye-Waller factor T_s considers this relative vibrational motion of different parts

of a molecule through the B-factor attenuation (Rupp, 2010; Sherwood and

Cooper, 2011). Atoms with high B-factors are generally flexible and thus

contribute less to the overall diffraction.

Since X-rays are scattered at the atomic shell, the exact atomic positions are not

directly accessible. A 3D map showing the spatial distribution of the electron

density is generated instead. The electron density ρ for each point (x,y,z) of a

crystal is calculated from both the magnitude of the structure factor $\left|F_{hkl}\right|$ and the respective phase Φ_{hkl} as well as the volume V of the unit cell by Fourier transform (Sherwood and Cooper, 2011).

$$\rho(x,y,z) = \frac{1}{V} \sum_{h} \sum_{k} \sum_{l} \left|F_{hkl}\right| \cdot e^{i \cdot \Phi_{hkl}} \cdot e^{-i \cdot 2\pi(hx+ky+lz)}$$

The magnitude of the structure factor reflects the amplitude of the scattered wave, the square of which is measured as intensity during a diffraction experiment. However, the corresponding phases cannot be directly derived from the measurements, a fact which is known as the phase problem of crystallography.

5.5 Solutions to the Phase Problem

Different methods have been developed for solving the phase problem, such as single/multiple isomorphous replacement (SIR/MIR), single-/multi-wavelength anomalous dispersion (SAD/MAD) and molecular replacement (MR). With the help of the Patterson function (see below) anomalous scattering information as well as coordinates of a suitable search model can be exploited to determine phase values for the unknown structure.

$$P(u,v,w) = \frac{1}{V} \sum_{h} \sum_{k} \sum_{l} \left|F_{hkl}\right|^2 \cdot e^{-i \cdot 2\pi(hu+kv+lw)}$$

The Patterson function is an inverse Fourier transform of the intensities $\left|F_{hkl}\right|^2$, thus no phase information is included, resulting in a map of interatomic distance vectors (Sherwood and Cooper, 2011). For the Patterson coordinates the

symbols u,v,w are utilized in order to differentiate them from the "normal" Fourier synthesis.

For isomorphous replacement both a native data set and several independent data sets originating from isomorphous heavy atom derivatives are necessary. The unit cell dimensions of native and derivatized crystals must be isomorphic, hence no molecular rearrangements should occur upon addition of the heavy atom. Owing to their strong scattering, the positions of the heavy atoms can be obtained by a difference Patterson function. In the next step, the amplitude and the phase of the wave scattered by the heavy atom are calculated. The phase corresponding to the native structure factor can then be determined geometrically, because the structure factors of the heavy atoms and those of the native crystal add up to the structure factor of the whole derivative (Drenth, 2007; Rhodes, 2006).

Anomalous dispersion experiments exploit the characteristic scattering properties of several elements for phasing. When the wavelength of the X-ray beam is adjusted to the absorption edge of the respective element, anomalous scattering can be observed. This phenomenon describes the absorption of the incident wave by electrons of the inner shell. Reemission at lower energy causes inelastic scattering with a typical phase shift distinct from the usually observed phase shift of the scattered wave. The phase shift is reflected by an additional imaginary component. In consequence, Friedel's law, which states that related reflections have the same amplitude but opposite phases, is broken. The difference between the amplitudes of the respective Friedel pairs allows calculation of an anomalous difference Patterson map, which helps to locate heavy atom positions (Drenth, 2007; Rhodes, 2006).

Structure determination by molecular replacement uses the phase information of a sufficiently similar crystal structure, termed the search model. Since crystal parameters may differ substantially between the unknown structure and the search model, the latter has to be aligned correctly in the unit cell of the unknown structure by a Patterson search. First, the model is oriented by rotating the Patterson vectors in 3 dimensions, followed by a 3D translation function, which ultimately positions the search model. Structure factors as well as phases can be calculated from the coordinates of the model. Finally, an electron density map is generated using the phases of the search model and the experimental structure factors of the unknown structure (Drenth, 2007; Rhodes, 2006; Sherwood and Cooper, 2011).

5.6 Data Collection & Processing, Model Building & Refinement

To protect protein crystals from radiation damage caused by the ionizing high energy X-ray beam, they have to be amorphously supercooled to a cryogenic temperature (100 K) (Drenth, 2007). Concomitant formation of ice can be avoided by soaking crystals in a cryoprotectant buffer. Subsequently, serial diffraction images are collected by rotating the crystal by small angle increments during X-ray exposure (Rupp, 2010).

In the next step, the collected data are processed. After determination of the unit cell parameters as well as the space group (indexing), spot intensities are integrated using iterative postrefinement. Corrections of their estimated errors yield the actual reflection intensities (Rupp, 2010). Afterwards, data are scaled and symmetry related reflections are averaged, thus structure factor amplitudes

are received from the merged intensities (Rhodes, 2006). The discrepancy between symmetry related reflections is given by the quality parameter R_{merge}, which also considers the redundancy of the data. As a result of data reduction, the intensity I and the corresponding standard deviation $\sigma(I)$ are identified for each reflection hkl (Sherwood and Cooper, 2011).

Electron density maps can be calculated either by using the phases from a search model (molecular replacement) or with the help of experimental phases. The latter procedure begins with the localization of the heavy atom position in real space by calculating anomalous or isomorphous difference Patterson maps (Rhodes, 2006). After cyclic refinement of the occupancy and the B-factor of the heavy atom coordinates, initial experimental phases are calculated, which are further improved by solvent flattening techniques (Rupp, 2010).

In the following step, the molecular model is built into the electron density map, if experimental phasing had been applied before. In the case of molecular replacement, the search model has to be correctly positioned in the unit cell of the unknown structure. Since initial models - either from experimental phasing or from molecular replacement - contain errors, successive rounds of rebuilding, error correction and refinement are necessary to get a good final protein model (Drenth, 2007; Rupp, 2010). During the refinement procedure, the parameters describing the structure model - generally the model coordinates, B-factors, and overall parameters such as scale factor, overall B-factors, bulk solvent corrections and anisotropy corrections - are optimized against all experimental data, in order to obtain the best fit between the observed structure factor amplitudes (F_{obs}) and the calculated model structure factor amplitudes (F_{calc}) (Rupp, 2010). This best-fit problem is mathematically implemented by the

minimization of a target function, usually a maximum likelihood target. The quality of the refinement can be accessed by the R-factor, which defines the agreement between F_{obs} and F_{calc} as follows (Rhodes, 2006):

$$ R = \frac{\sum \left| F_{obs} - F_{calc} \right|}{\sum \left| F_{obs} \right|} $$

Generally, owing to a low observation-to-parameter ratio, the target function is underdetermined. The introduction of restraints such as bond lengths and bond angles provide "artificial" observations, whereas constraints correlate appropriate parameters, thus reducing the overall number of parameters to be satisfied (Sherwood and Cooper, 2011). Additionally, cross validation avoids overpara-meterization by excluding a fraction of data from the refinement, yielding the R_{free}-value as an unbiased indicator for the quality of the structure (Rupp, 2010). The R_{free}-value usually exceeds the conventional R-value by approximately 5 %.

After completion of refinement, the model is validated in different ways, for instance by checking the main-chain torsion angles in a Ramachandran plot or by eradicating nonsense physical contacts.

6 The Wss1 Metallopeptidase

6.1 Introduction - The Role of Wss1 in SUMOylation

Posttranslational modification constitutes a major regulatory mechanism for the biological functions of many proteins. Besides well studied small molecule tags, such as phosphoryl and acetyl groups, proteinaceous modulators have emerged over the past decades, the first example of which is Ubiquitin (Ciechanover et al., 1978). The latter and its related U̲biquitin-l̲ike modifiers (UBLs), such as SUMO (s̲mall U̲biquitin-like mo̲difier), are reversibly attached to target proteins, thereby altering their conformations or interaction surfaces (Schwartz and Hochstrasser, 2003). Figure 6 depicts the generalized conjugation cycle for UBLs.
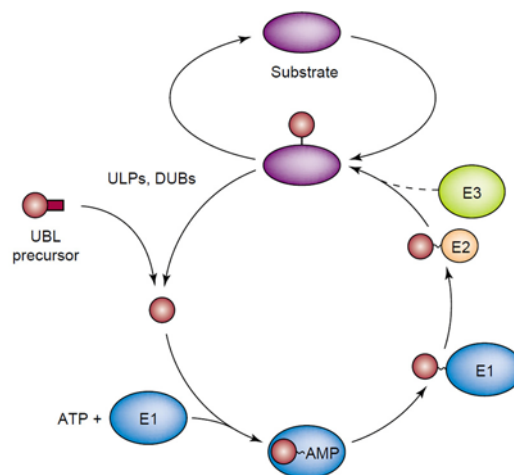
Figure 6:
Generalized UBL conjugation cycle (Schwartz and Hochstrasser, 2003). UBL conjugation requires an ATP-dependent E1-activating enzyme, an E2-conjugating enzyme and an E3 ligase. The product is an isopeptide bond between the C-terminal glycine of mature SUMO and a lysine side chain of substrate proteins. DUBs or ULPs catalyze deconjugation.

In the case of modification by SUMO, a variety of cellular processes including DNA-repair, signal transduction, gene expression and cell cycle progression are controlled (Johnson, 2004; Kerscher et al., 2006; Meulmeester and Melchior,

2008). Coupling and removal of UBLs are equally important for flexible responses to environmental stimuli. While UBLs are linked to the respective substrate by a cascade of E1, E2 and E3 enzymes, a single UBL-specific protease (ULP, or DUB in the case of Ubiquitin) catalyzes the detachment of the tag. For instance, the uncoupling of SUMO from client proteins in *S. cerevisiae* (Smt3) is performed either by ULP1 or ULP2 (Li and Hochstrasser, 1999; Li and Hochstrasser, 2000).

Recently, another protein with SUMO-directed protease activity was reported for yeast, namely Wss1 (Mullen et al., 2010). Wss1 was initially described in a study about genes which are involved in accurate chromosome behavior during mitosis (Biggins et al., 2001). The yeast SUMO gene (SMT3 in *S. cerevisiae*) was found to be required for proper chromosome segregation at the anaphase, since a temperature sensitive Δ*smt3* mutant exhibited abnormal sister chromatid separation. Furthermore, SMT3 deletion considerably impaired cell growth, whereas overexpression of WSS1 partially rescued this growth defect.

A genome wide screen in *S. cerevisiae* disclosed significant UV radiation sensitivity for the Δ*smt3* strain (Birrell et al., 2001). This finding was corroborated by another group (O'Neill et al., 2004), who also provided additional lines of evidence that relate Wss1 function to the maintenance of genome integrity, such as a physical interaction between the Wss1 and Tof1 proteins. Tof1, which functions in the stabilization of stalled replication forks, also interacted genetically with Wss1, when the according double mutant encountered DNA lesion. Disruption of several other genes that are important for DNA recombination, cell cycle control, repair of replication forks and the establishment of sister chromatid cohesion, resulted in synergistic intensification of DNA damage susceptibility

when WSS1 was absent at the same time. Beyond the genetic outcomes, a slow growth phenotype was observed for a double mutant of WSS1 and the SGS1 DNA helicase, whereas the loss of WSS1 alone did not reveal adverse effects on cell growth. Consistent with a possible role in DNA preservation, Wss1 protein resides near the nuclear membrane (van Heusden and Steensma, 2008). In dividing cells, it is exclusively present in the mother cell.

Bioinformatic investigations predicted Wss1 as a peptidase candidate involved in the Ubiquitin signaling system (Iyer et al., 2004). In particular, a globular domain containing a conserved HExxHx(5)H-motif typical for Zn-dependent proteases, provided the basis for the classification of a broadly distributed number of plant and fungal proteins into a novel family of presumable metalloproteases. This class was termed after the so far solely characterized member as the WLM family (Wss1-like metalloproteases). The WLM-family can be subdivided into 2 groups, 1 of which bears 1 or 2 C-terminal Little Fingers, a distinct version of a Ubiquitin binding domain, whereas the second group carries a N-terminal Ubiquitin-like domain. Since Wss1 had been implicated in a variety of SUMOylation dependent cellular processes (see above), it was speculated that it might be the first example of a metalloprotease, which appears as a specific deSUMOylating enzyme within the Ubiquitin Proteasome System (UPS).

This hypothesis implies that SUMO and Ubiquitin pathways converge (Denuc and Marfany, 2010), an idea that is supported by the identification of SUMO-targeted Ubiquitin ligases, which ubiquitinate substrates that have already been labelled with SUMO (Geoffroy and Hay, 2009; Perry et al., 2008). In this context, a very recent publication characterized Wss1 protein as a SUMO-dependent isopeptidase that apparently chops off both Ubiquitin and SUMO from model

targets (Mullen et al., 2010). Moreover, it was reported that Wss1 physically interacts with SUMO but not with Ubiquitin, which is in line with the presence of 2 predicted SUMO-interaction motifs (SIMs) located in the C-terminal part of Wss1 (Uzunova et al., 2007).
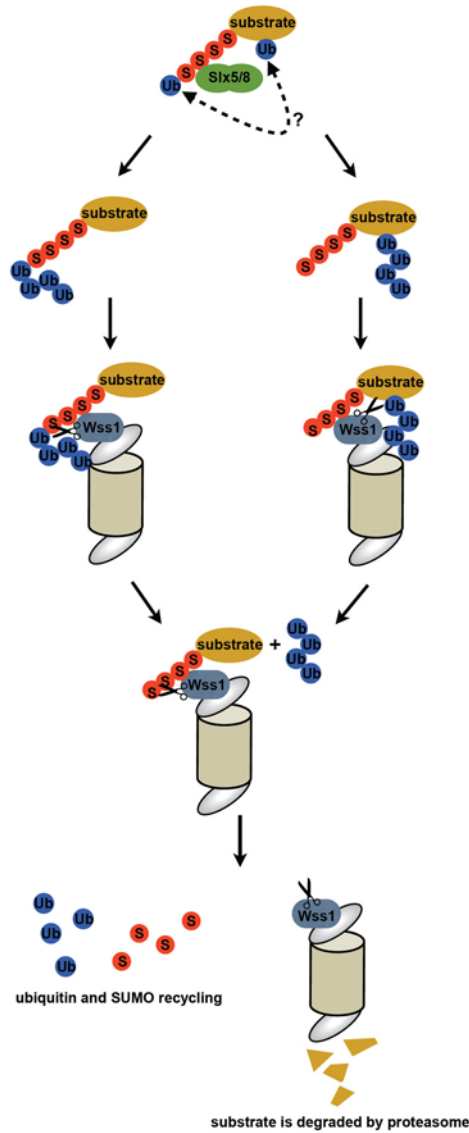
Figure 7:
Potential role of Wss1 (Su and Hochstrasser, 2010). The SUMO-targeted Ubiquitin ligase Slx5-Slx8 labels SUMOylated substrates with Ubiquitin. The exact conjugation pattern is still unclear. Wss1 may associate with the proteasome and recognize the SUMO-tags of substrates. This association induces the removal of Ubiquitin (and perhaps also of SUMO) from the target protein.

While Wss1 protein obviously denies pure poly-Ubiquitin chains as a substrate, it yet cleaves Ubiquitin when attached to monomeric SUMO or a SUMO-chain. Assays employing a fusion protein consisting of Ubiquitin, SUMO and a peptide tag yielded comparable results, indicating a SUMO-targeted deubiquitylating task for Wss1 (Su and Hochstrasser, 2010). In this scenario Wss1 would preferably cut off Ubiquitin, depending on prior binding to SUMO. Taken together, the results are consistent with the idea that Wss1 behaves inversely to a SUMO-targeted Ubiquitin ligase, such as Slx5-Slx8, for which a genetic interaction with WSS1 was also described (Mullen et al., 2010; Su and Hochstrasser, 2010). Furthermore, association of Wss1 with proteasomal subunits suggested a possible direct link to the proteasome. The model shown in Figure 7 illustrates the potential role of Wss1.

6.2 Results

6.2.1 Construct Planning and Testing

Since the initial description of Wss1 as weak suppressor of a Δ*smt3*-mutation in *Saccharomyces cerevisiae* (Biggins et al., 2001), further investigations on the putative metallopeptidase focused only on baker's yeast as a model organism. However, PSI-BLAST similarity searches, using different sections of the ScWss1 amino acid sequence as a query, recovered homologous proteins with highly significant E-values not only in fungi, but also in plants (Iyer et al., 2004). Consequently, in the sense of a funnel system approach, alternative Wss1-constructs were considered both from a second yeast strain and from a plant organism.

Interestingly, *Schizosaccharomyces pombe*, the second well-established fungal model organism, carries two homologous Wss1-genes, which are termed SpWss1a and SpWss1b in this thesis. SpWss1a (UniProt-ID: Q9P7B5) corresponds to ScWss1; SpWss1b (UniProt-ID: O94580) possesses an additional N-terminal Ubiquitin-like domain (UBL-domain) (Matsuyama et al., 2006; Wood et al., 2002). Both SpWss1a and b contain a WLM-domain (Wss1-like metalloprotease). They may be evolutionary related by gene duplication and therefore may have different functions, but as members of the WLM-family, they were also included in this study.

As plant representatives for Wss1, genes from two *Ostreococci*-strains were used (UniProt-IDs: A4RTT7 and Q013P3). *Ostreococcus lucimarinus* and *Ostreococcus tauri* are unicellular, spherically shaped green algae and their genomes encode a very short version of a Wss1-homologue each (Derelle et al., 2006; Palenik et al., 2007). In general, short sequences are particularly suitable

for crystallographic experiments as the corresponding proteins tend to form less flexible regions, which in turn raises their crystallization probability.

Figure 8 shows a multiple ClustalW amino acid sequence alignment of the five fulllength constructs selected for this thesis (Waterhouse et al., 2009).
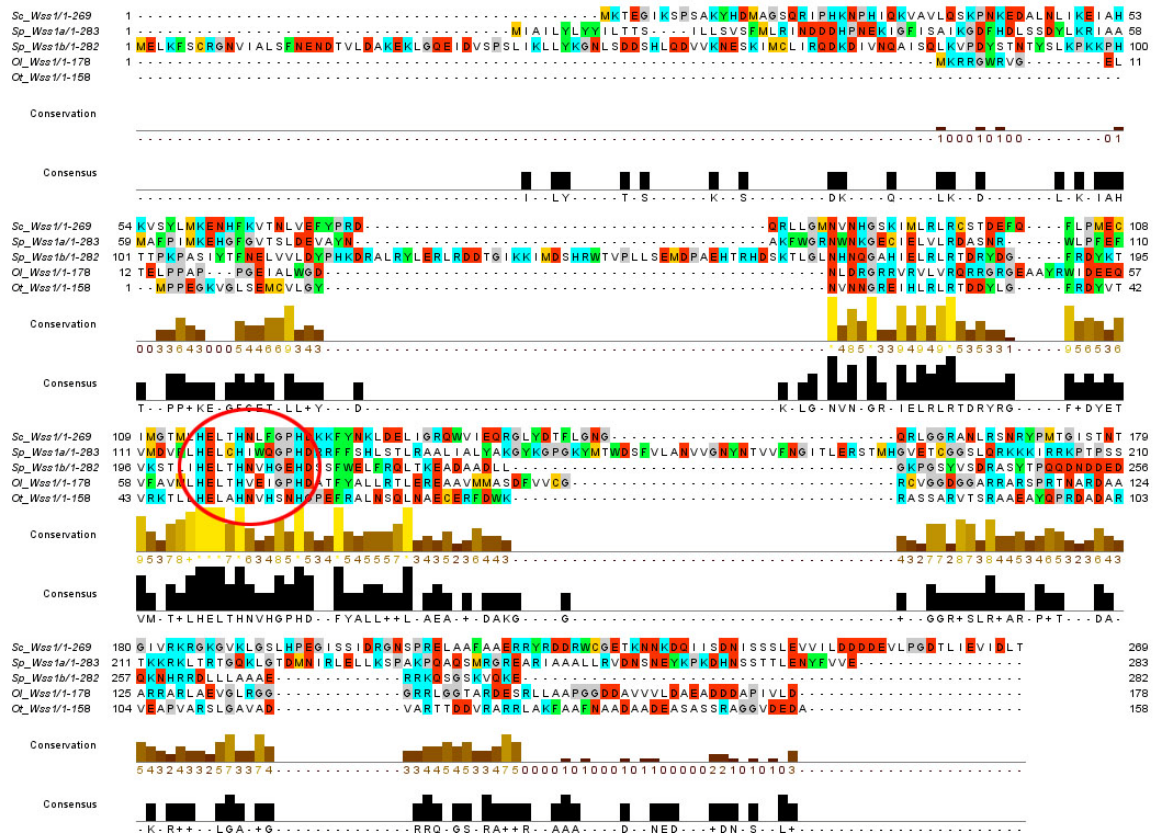
Figure 8:
Alignment of amino acid sequences from 5 Wss1 proteins (Waterhouse et al., 2009). Abbreviations stand for: Sc: *Saccharomyces cerevisiae*, Sp: *Schizosaccharomyces pombe*, Ol: *Ostreococcus lucimarinus*, Ot: *Ostreococcus tauri*. The degree of conservation and the consensus sequence are indicated as well.

A conserved core region, reaching from Asn83 to Leu136 (numbers according to fulllength ScWss1) comprises the predicted Zn-binding motif HExxHx(5)H, marked by a red ellipse. Early studies on Zn-endopeptidases revealed that the three histidine residues serve as Zn-ligands, whereas the glutamic acid residue polarizes a water molecule for the nucleophilic attack of the substrate (Bode et

al., 1992; Murphy et al., 1991; Rawlings and Barrett, 1993; Stocker et al., 1990). The remaining protein segments exhibit only low or even no conservation, especially the N-terminal region. Thus, beside the fulllength genes, individually truncated constructs were generated based on secondary structure predictions calculated with Jalview (Waterhouse et al., 2009). Sequence cutting may help to remove terminal, putative flexible regions that might be deleterious for crystallization tendency. Figure 9 illustrates the secondary structure prediction for fulllength ScWss1 and exemplifies possible truncation sites either at the beginning or the end of secondary structures.
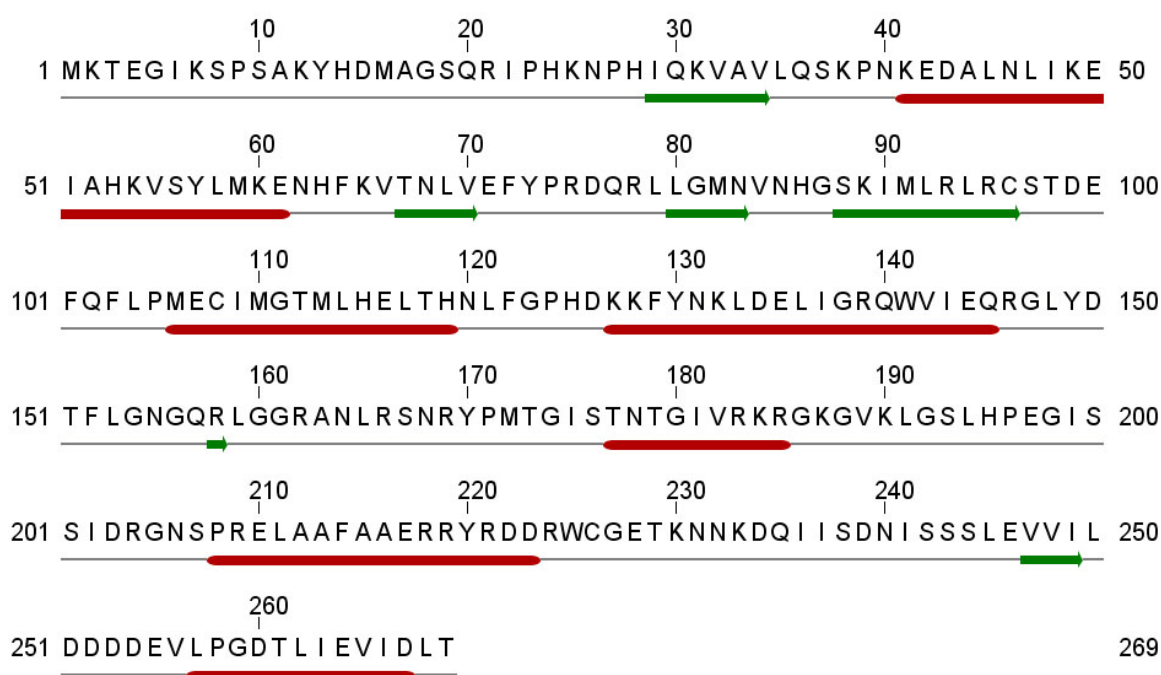
Figure 9:
Secondary structure prediction of ScWss1 using Jalview (Waterhouse et al., 2009).

The HExxH-motif (His115 - His119) is supposed to be integrated into an "active-site helix" (Bode et al., 1993) and the distribution pattern of helices and strands suggests an overall structure similar to Zincin-like metalloproteases (Dhanaraj et al., 1996; Iyer et al., 2004). Both an N-terminal stretch of 27 amino acids (Met01

- Pro27) as well as a C-terminal part of 44 amino acids (Cys226 - Thr269) are predicted as unstructured regions and therefore, these sections were eliminated in ScWss1 by molecular biology methods. Accordingly, a putative N-terminal signal sequence in SpWss1a (Met01 - Glu33) was clipped off. For SpWss1b, the presumed N-terminal Ubiquitin-like domain (Met01 - Arg69) as well as the WLM-domain were cloned as separate constructs. Met01 was generally deleted.

	ScWss1		SpWss1a		SpWss1b					Ol	Ot
	2-225 full	28-145 WLM	37-283 full	34-147 WLM	2-282 full	108-282 WLM	108-232 WLM	2-69 UBQ	2-94 UBQ	2-178 full	4-158 full
BL21DE3 pRSETA-6xHis	37°C 30°C 20°C	—	37°C 30°C 20°C	—	—	37°C 30°C 20°C	—	—	—	37°C 30°C 20°C	37°C 30°C 20°C
BL21DE3 pRSETA-GST	—	37°C 30°C 20°C	—	37°C 30°C 20°C	—	—	20°C	—	—	37°C 30°C 20°C	37°C 30°C 20°C
XL1blue pQE30-6xHis	37°C 30°C 20°C	37°C 30°C 20°C	37°C 30°C 20°C	37°C 30°C 20°C	37°C 30°C 20°C	37°C 30°C 20°C	20°C	37°C 30°C 20°C	37°C 30°C 20°C	—	—
XL1blue pQE30-GST	37°C 30°C 20°C	37°C 30°C 20°C	37°C 30°C 20°C	37°C 30°C 20°C	—	—	—	—	—	—	—
BL21DE3 pET28b-SUMO	—	37°C 30°C 20°C	—	37°C 30°C 20°C	20°C	—	—	—	—	—	—

Table 5
Overview of expression test results of the Wss1 constructs generated in this thesis.
Red colour indicates no or only insoluble expression at the given temperature.
Green colour represents soluble expression.

Resulting gene versions of all organisms were cloned in several *E. coli*-based expression systems and tested for soluble expression under varying conditions as described in the materials and methods chapter. Expression tests were analyzed by SDS-PAGE and Table 5 summarizes the respective results. Most

constructs were insoluble or not expressed at all under the tested conditions, as indicated by the red colour. Soluble protein was only produced from 3 SpWss1b gene versions (green). Since initial experiments focused on the WLM-domain, the SpWss1b segment 108-282 is the starting point for the further considerations.

6.2.2 Characterization of SpWss1b Protein

After expression of a His-tagged version of the SpWss1b long WLM-domain (108-282), affinity chromatographic purification yielded a major band of the expected 22 kDa protein on the SDS-gel. Putative impurities of smaller sizes down to approximately 16 kDa showed only weak intensities. Intriguingly, a time dependent inversion of the band intensities was observed, with transitorily strong bands in a size range from 22 kDa to 16 kDa, finally resulting in a single, stable 16 kDa fragment after 17 days (Figure 10A, upper row). No other bands could be detected anymore after that period of time. A peptide mass fingerprint identified 3 of the ambiguous bands, including the 16 kDa protein, as fragments of the purified SpWss1b WLM-domain (Figure 10B, red arrows). This observation could have been an outcome of mere, arbitrary protein disintegration, which in turn would however not be consistent with the stability of the 16 kDa band. Degradation effects by endogenous *E. coli* proteinases could be excluded most likely, as a proteinase inhibitor mixture had been added to the experiment. Hence, in order to rule out the phenomenon of random protein decay, an E203Q mutant of the WLM-domain construct (108-282) was generated. This mutation replaces the active site glutamic acid side chain with a glutamine side chain, supposedly lowering proteolytic activity, owing to reduced polarization of the

attacking water molecule. Indeed, for the E203Q mutant protein, the noticeable band degradation pattern occurred much slower compared to the wildtype (Figure 10A, bottom row). Even after 35 days, the 22 kDa band was still the most prominent one. Smaller bands showed up delayed and with much weaker intensities. Thus, these results suggest, that the observable band inversion phenomenon is much more likely due to autoproteolytic processing of the SpWss1b WLM-domain construct than due to random protein decay. Whether this self-cutting arose in *cis* or in *trans* remained elusive at this stage.
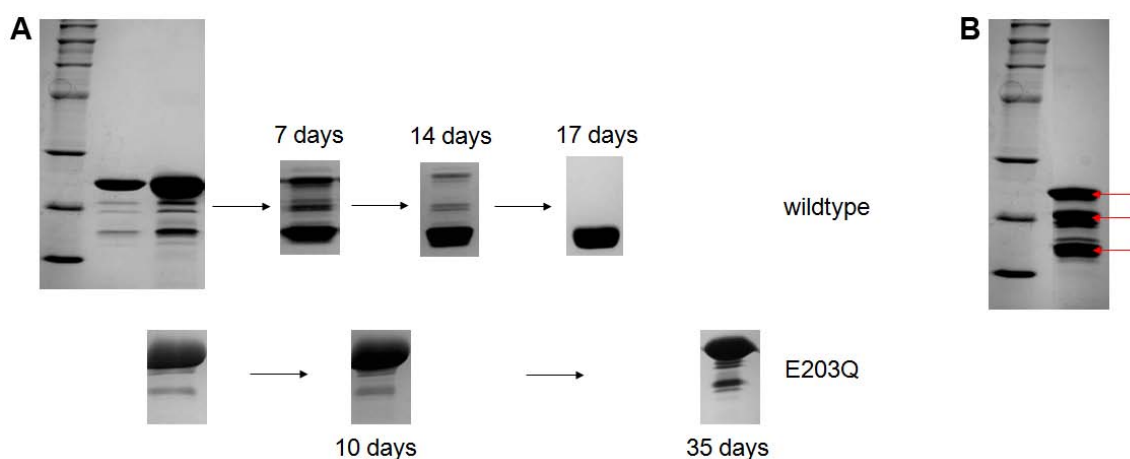
Figure 10:

Time course of SpWss1b self digestion. A: The wildtype 22 kDa SpWss1b construct (108 - 282) exhibits considerable autoproteolysis, resulting in a stable 16 kDa fragment after 17 days (upper row). Self truncation of the respective E203Q-mutant is significantly impaired (lower row). B: The intermediates of self digestion, which were analyzed by peptide mass fingerprinting, are indicated by a red arrow. Molecular weight of size marker bands in kDa from top to bottom: 200, 119, 66, 43, 29, 20, 14.

Further characterization experiments aimed at the wildtype 16 kDa SpWss1b WLM-domain fragment. A total mass determination of the self truncated protein yielded a size range from 15.2 to 16.8 kDa, which means that a population of proteins of similar but still different size was produced. Referring to the amino acid sequence, an exact allocation of the cleavage site was therefore not

possible. Furthermore, it remained to be elucidated which terminus was subject to the self truncation. To this end, a Western Blot using an anti-His antibody detected the intact His-tag on the stable 16 kDa fragment, supplying strong evidence, that the presumed self cleavage of the SpWss1b WLM-domain (108-282) had exclusively taken place at the C-terminus. Although it has to be mentioned, that the existence of a C-terminal 16 kDa particle, lacking the His-tag, could not be excluded definitively. Based on these findings, a C-terminally shortened construct was cloned according to the secondary structure prediction (Figure 11).
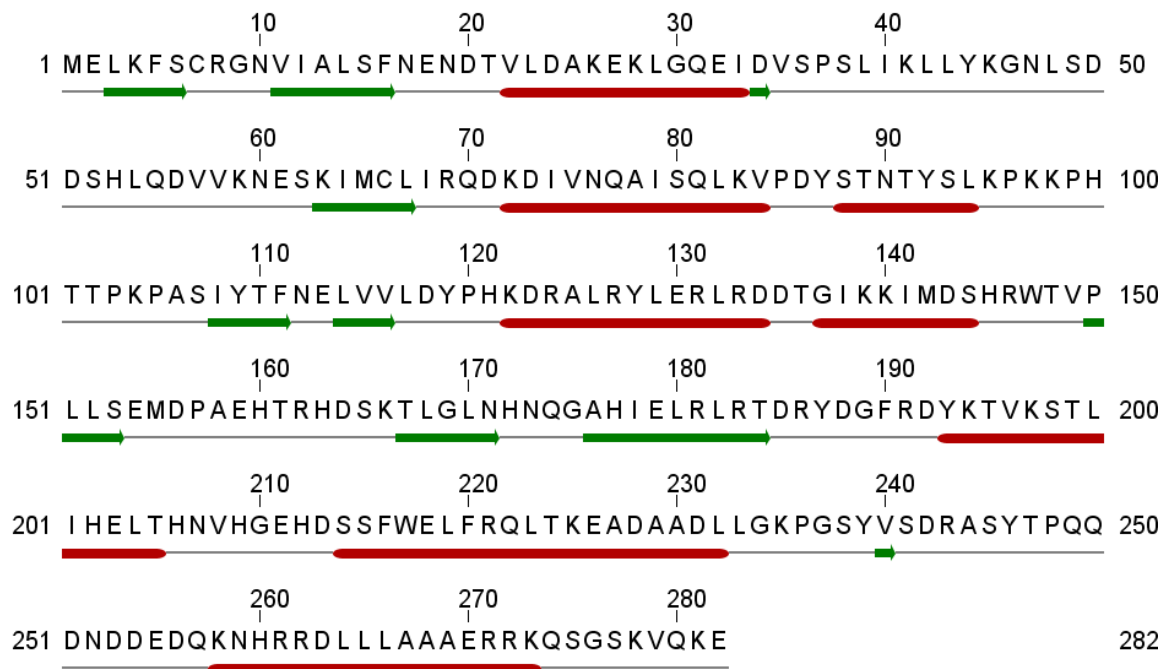
Figure 11:
Secondary structure prediction of SpWss1b using Jalview. (Waterhouse et al., 2009)

Assuming a size of approximately 16 kDa, the most plausible C-terminus locates at the end of the second last helix that stretches from Ser214 to Leu232. Thus, the new SpWss1b short WLM-domain reaches from Ile108 to Leu232.

The autoproteolytic digestion manifests itself in an indistinct pattern of bands on the SDS-gel, not indicating a defined target site of the protease. Animated by the assumed metalloprotease function (Iyer et al., 2004) as well as first functional studies on ScWss1 (Mullen et al., 2010), the obvious catalytic activity of the SpWss1b WLM-domain was tested on two defined substrates. For this purpose SpWss1b (108-232) was added to an artificial Smt3-TPR fusion protein on the one hand (a generous gift by Andreas Schmid, Biotechnology, TUM) and on the other hand to a synthetic tetra-Ubiquitin chain (Boston Biochem). The results were analyzed by SDS-PAGE (Figure 12).
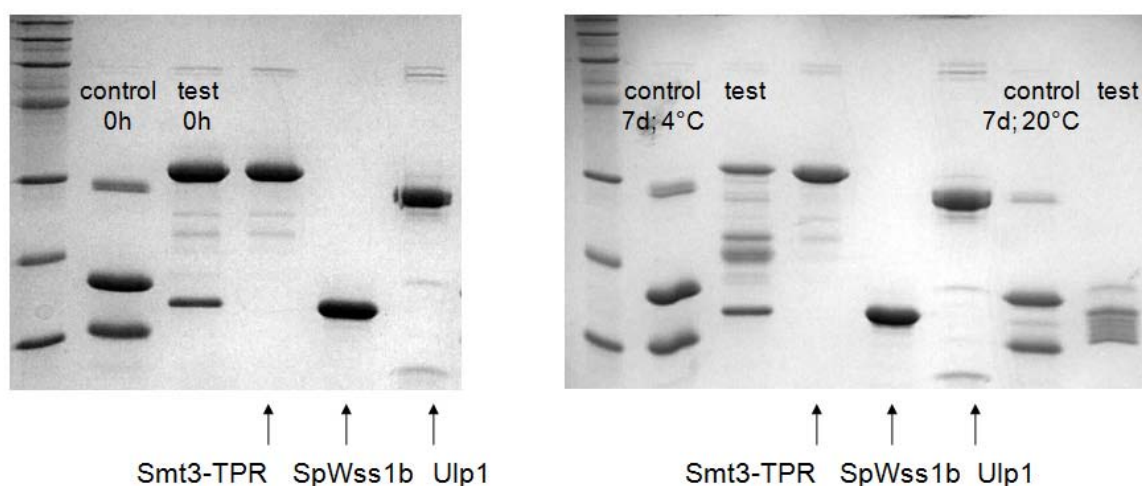
Figure 12:
Initial activity analysis of SpWss1b. Unlike Ulp1 (control), the 16 kDa SpWss1b catalytic core domain displays unspecific proteolytic activity on the model substrate Smt3-TPR. Same size marker as in Figure 10.

The Smt3-TPR fusion protein links the two individual components via a conventional peptide bond, which can be split by Ulp1, a protease that specifically cleaves Smt3 protein conjugates and which was used as a positive control in this assay (Li and Hochstrasser, 1999; Li and Hochstrasser, 2003). Figure 12 (left panel, control lane) demonstrates that the respective peptide bond in the Smt3-

TPR protein is being broken immediately after addition of Ulp1, resulting in two discrete bands representing Smt3 and TPR alone, respectively. By contrast, SpWss1b does not exhibit a comparable performance. Both at 4 °C and at 20 °C several bands smaller than the Smt3-TPR protein are visible after one week (Figure 12, right panel, test lanes). As already mentioned for the autocatalytic self processing, SpWss1b seems to cause an undefined cutting of the substrate. Interestingly, a discontinuous band pattern is produced, which implies some preference of SpWss1b for certain structural features of the substrate. The control lane (right panel) precludes thermodynamic instability of the Smt3-TPR substrate.

The tetra-Ubiquitin chain connects the Ubiquitin monomers by mixed linkages via Lys63 and Lys48, respectively. No cleavage of these bonds was detected for varying concentrations of SpWss1b. Therefore, SpWss1b is rather unlikely to process poly-Ubiquitin chains attached to target proteins.

In the following investigations, structural features of SpWss1b (108 - 232) were characterized by Nuclear Magnetic Resonance (NMR) and Totalreflexion X-Ray Fluorescence (TXRF) prior to crystallographic experiments. A 1H-NMR spectrum was recorded for initial folding analysis (Figure 13) in collaboration with the group of Prof. Sattler, Chair of Biomolecular NMR Spectroscopy (TUM). In the spectrum of SpWss1b (108 - 232), the hydrogen signal for peptide bonds shows typical peaks for α-helices and β-strands, suggesting a compact overall fold for the small molecule. Low structural flexibility can be deduced from defined hydrogen signals for methyl groups of amino acid side chains, which is a favourable condition for the crystallization tendency.
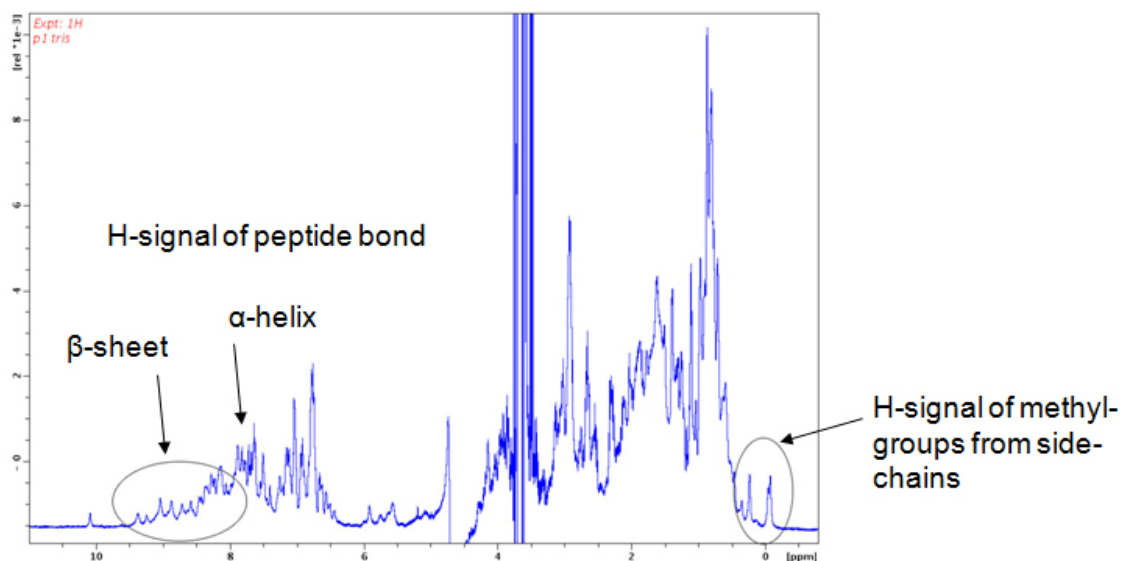
Figure 13:
1-H-NMR spectrum of SpWss1b.

A quantitative TXRF-analysis for metal ion determination was carried out together with the group of Prof. Schuster, Chair of Analytical Chemistry (TUM). The bivalent cations Ca^{2+}, Ni^{2+}, Zn^{2+} and Cu^{2+} were detected in the protein solution. Remarkably, only Ni^{2+} was measured in the expected 1:1 molar ratio compared to the protein, whereas the Zn^{2+}-concentration was too low by a factor of 3. Ca^{2+} displayed a 3-fold excess compared to the protein and Cu^{2+} was only found in traces. Thus, contrary to expectation, the amount of Zn^{2+}-ions is not sufficient for stoichiometric occupancy of the active site of SpWss1b. An active site occupation by Ni^{2+} is more reasonable, due to the very similar ionic radius (r $[Zn^{2+}]$ = 83 pm; r $[Ni^{2+}]$ = 78 pm) and the preceding Ni-NTA chromatography. However, active site coordination of Ca^{2+} with an ionic radius of 106 pm is implausible.

6.2.3 Crystal Structure of SpWss1b

Initial crystallization trials were carried out for both the wildtype SpWss1b short WLM-domain (108 - 232) and the E203Q mutant SpWss1b long WLM-domain (108 - 282) as described in the material and methods section. Sitting drop high throughput screens were performed by using 96-well format microplates and 5 standard crystal screening kits (Qiagen) on a Phoenix robot (Art Robbins Instruments). The protein concentration was varied from 10 mg/ml to 17 mg/ml and crystal droplets consisted of 1 volume of reservoir solution and 1 volume of protein suspension. Wildtype SpWss1b (108 - 232) crystallized after few days, whereas crystals of the E203Q mutant (108 - 282) grew within three months. Figure 14 shows 3 crystals with their typical size of about 150 × 70 × 30 µm^3. Colouring is caused by a polarization filter.
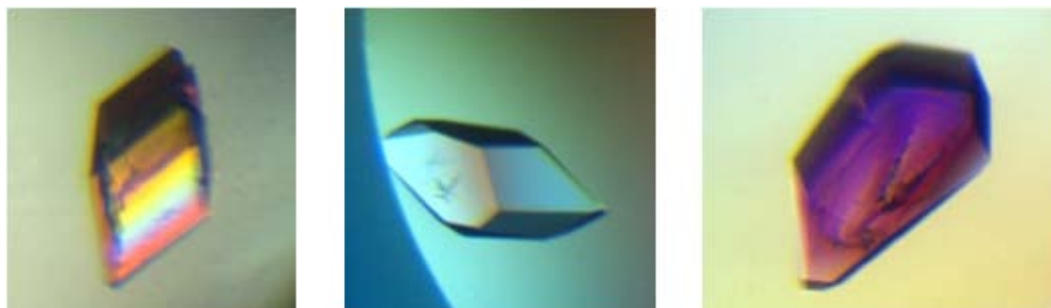
Figure 14:
Crystals of SpWss1b short WLM-domain (108 - 232).

The crystal structure was determined by single-wavelength anomalous disper-sion (SAD) at a resolution of 1.0 Å. To this end, an anomalous data set had been collected at the SLS synchrotron (Villigen, Switzerland). A fluorescence energy scan prior to anomalous data set collection identified the central metal ion not as Zn, but as Ni, which is in agreement with the results of the quantitative TXRF-analysis. Data processing for the wildtype SpWss1b short WLM-domain structure

yielded the orthorhombic space group $P2_12_12_1$ with the following unit cell axes: a = 40.3 Å, b = 41.3 Å, c = 68.5 Å. SHELXD located 1 strong heavy atom site and subsequent SHARP-SAD phasing as well as SOLOMON solvent flattening resulted in appropriate phases of about 1.8 Å (Bricogne et al., 2003; Sheldrick, 2010). The calculated electron density revealed well defined secondary structure elements including defined side chains, thus allowing automated protein chain tracing and model building with ARP/wARP (Langer et al., 2008). Positional refinement with REFMAC (Murshudov et al., 1997; Vagin et al., 2004) further improved phases, so that missing structural parts could be completed.

Subsequently, the model was refined against the native dataset collected at 1.0 Å resolution. Finally, TLS-refinement (Translation/Libration/Screw vibrational motion) (Murshudov et al., 1999; Vagin et al., 2004)yielded current crystallographic values of R_{crys} = 14.9 %, R_{free} = 17.9 %, r.m.s. bond length = 0.027 Å, and r.m.s. angles = 2.2°. The geometry of the whole molecule, including the two N-terminal amino acids (Gly and Ser), originating from the BamHI restriction site, is well defined in the electron density map, except for a loop of 9 amino acids (Ala158 - Lys166; numbers according to fulllength SpWss1b), which is structurally distorted. Table 6 gives an overview of the data collection and refinement statistics.

	SpWss1b native[a]	SpWss1b anomalous[a]
Crystal parameter		
Space group	$P2_1 2_1 2_1$	$P2_1 2_1 2_1$
Cell dimensions		
a, b, c (Å)	40.3; 41.3; 68.5	40.1; 41.4; 68.3
α, β, γ (°)	90.0; 90.0; 90.0	90.0; 90.0; 90.0
Data collection		
Beam line	SLS, X06DA	SLS, X06DA
Wavelength (Å)	1.0	1.4854
Resolution range (Å)[b]	10-1.0 (1.1-1.0)	15-1.8 (1.9-1.8)
No. observations	545126	75642
Unique reflections[c]	61720	15941
Completeness (%)[b]	98.7 (99.7)	95.2 (92.4)
R_{merge} (%)[b,d]	5.9 (39.8)	4.6 (23.6)
I / σ (I)[b]	21.0 (4.9)	18.7 (5.1)
Refinement		
Resolution (Å)	8.0-1.0	
R_{work} / R_{free}[e]	0.149 / 0.179	
No. reflections working set	58589	
No. reflections test set	3083	
No. nonhydrogen	983	
No. solvent water	224	
No. Ni	1	
No. O_2	1	
Average B-factor (Å^2)	13.1	
R.m.s. deviations[f]		
Bond lengths (Å)	0.027	
Bond angles (°)	2.239	
Ramachandran (%)[g]	98.2 / 1.8 / 0.0	

Table 6:

Data collection and refinement statistics regarding SpWss1b.
[a] Data sets from 2 different crystals; [b] values in parenthesis of resolution range, completeness, R_{merge} and I/σ (I) correspond to the last resolution shell; [c] Friedel pairs were treated as different reflections; [d] $R_{merge}(I) = \Sigma_{hkl}\Sigma_j |[I(hkl)_j - I(hkl)]|/[\Sigma_{hkl} I_{hkl}$, where I(hkl)$_j$ is the jth measurement of the intensity of reflection hkl and <I(hkl)> is the average intensity; [e] $R = \Sigma_{hkl} | |F_{obs}| - |F_{calc}| |/\Sigma_{hkl} |F_{obs}|$, where R_{free} is calculated without a sigma cutoff for a randomly chosen 5% of reflections, which were not used for structure refinement, and R_{work} is calculated for the remaining reflections (Brunger, 1992); [f] Deviations from ideal bond lengths/angles (Engh and Huber, 1991); [g] Number of residues in favoured region / allowed region / outlier region

The structure reveals that the WLM-core of SpWss1b forms a small, compact domain consisting of four tightly packed α-helices and a four-stranded antiparallel β-sheet (Figure 15).
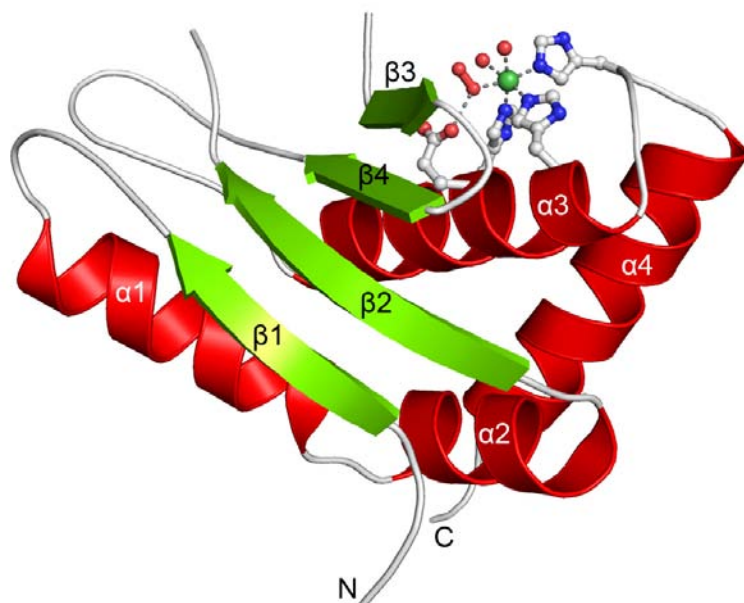
Figure 15:

Crystal structure of SpWss1b short WLM-domain (108 - 232) shown as cartoon. Helices are coloured in red, strands in green. Active site residues are shown as ball-and-stick models. The image was created with PyMol (DeLano, 2002).

The catalytic centre, comprising the metal binding HExxHx(5)H-motif, is solvent exposed. The β-sheet virtually ascends on a scaffold formed by the four helices. The apical β3-strand flanks the active site, thereby allowing direct interaction with a potential substrate. With this architecture the β-sheet may constitute a platform for the scissile substrate sequence, which, on its part, also may adopt β-conformation, thus being stabilized in a shared β-sheet directly above the catalytic centre.
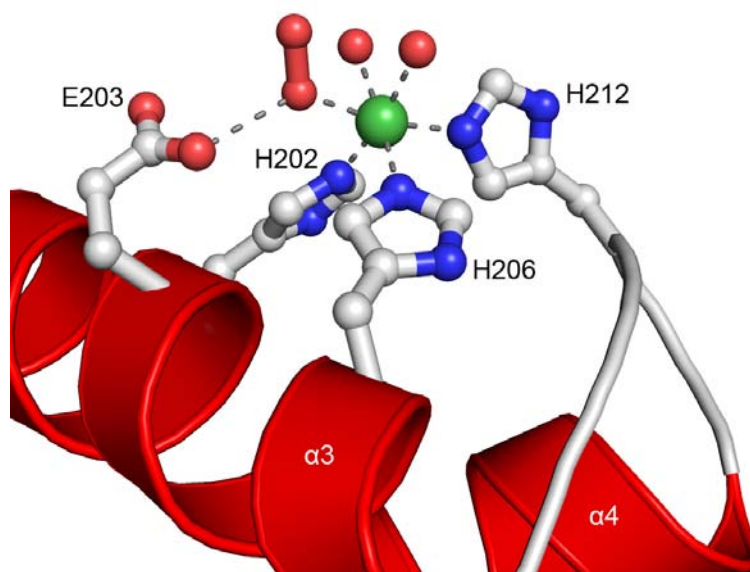
Figure 16:

Active site of SpWss1b short WLM-domain (108 - 232) shown as cartoon. Side chains are shown as ball-and-stick models and numbering corresponds to the full-length construct. The central Ni^{2+}-ion is shown in green and coordinating molecules in red. The image was created with PyMol (DeLano, 2002).

The predicted 3 histidines, as well as 2 water molecules and 1 oxygen molecule coordinate the active site Ni^{2+} ion by forming a distorted octahedron (Figure 16).

To verify a possible metal substitution in the active site during the protein purification procedure, an alternative protocol was established, avoiding the initially employed Ni-NTA resin. A purification strategy combining the advantages of both GST- and SUMO-tag together with subsequent size exclusion chromatography succeeded in obtaining sufficient amounts of homogenous SpWss1b short WLM-domain protein (108 - 232). The crystallization condition was significantly different from that for His-tag purified SpWss1b, pointing towards alterations of the protein traits, presumably due to metal ion exchange in the active site. However, a fluorescence energy scan with subsequent ano-malous data set collection for the respective crystal is necessary to clarify the identity of the active site metal ion. If a Zn-ion is found to occupy the catalytic

centre, it seems very likely that the Ni-ion occurs as an artifact of the Ni-IMAC purification procedure.

To further investigate the correlation of structure and function, the coordinates of the SpWss1b short WLM-domain structure were analyzed in view of structure based homology with the help of the DALI-server (http://ekhidna.biocenter. helsinki.fi/dali_server/), which performs a comparison between the query structure and all structures of the Protein Data Bank (PDB). Assuming an evolutionary continuity of structure and function, the description of structural similarity relationships between protein structures allows inference of functions of newly discovered proteins (Holm and Rosenstrom, 2010). According to the DALI search output, SpWss1b structurally resembles domains of metal dependent peptidases, such as the anthrax lethal toxin endopeptidase component (Z-score: 7.9, rmsd: 3.5; M34-family), the human endoplasmic reticulum aminopeptidase (Z-score: 7.1, rmsd: 3.0; M1-family) and the tricorn protease interacting factor F3 from *Thermoplasma acidophilum* (Z-score: 6.3, rmsd: 3.1; M1-family). Interestingly, most of the best hits refer to aminopeptidases, implying slight functional divergence from the isopeptidase activity proposed for ScWss1 (Mullen et al., 2010). However, structural homology to the anthrax lethal factor suggests an endopeptidase activity for SpWss1b. Hence, a clear functional allocation remains enigmatic at this stage.

Sequence identities between structural neighbours and the query lie only in an insignificant range from 4% to 24%. However, a striking structural similarity does not contradict with low sequence identity as exemplified by the structural superposition of SpWss1b and the respective region of human endoplasmic reticulum aminopeptidase (hERAP1) (Nguyen et al., 2011).
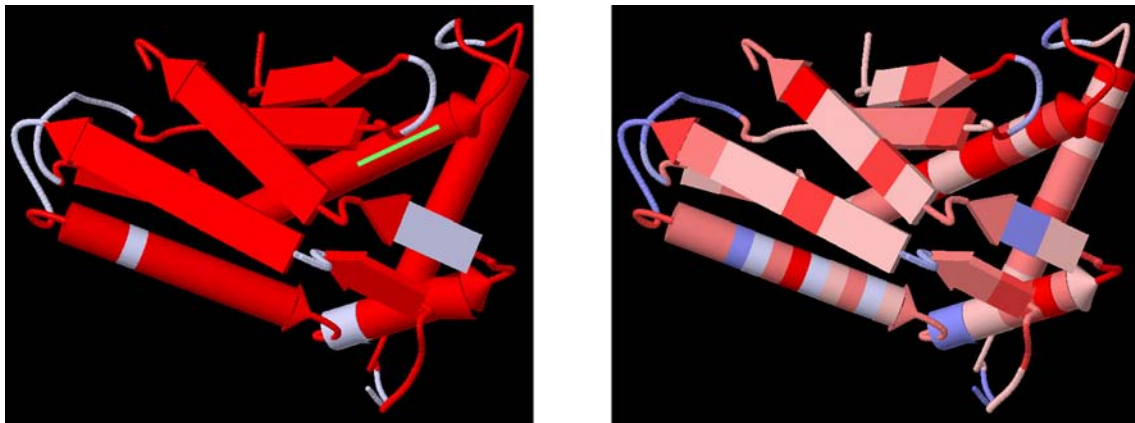
Figure 17:

Cartoon representation of SpWss1b short WLM-domain (108 - 232) showing structure (left) and sequence (right) conservation compared to hERAP1. Colour code for conservation: red: strong, pink: medium, pale blue: weak, blue: no. The active site is indicated by a green bar. The figure was generated on the DALI-server (Holm and Rosenstrom, 2010).

Figure 17 depicts a cartoon representation of the SpWss1b backbone coloured either by structure conservation (left panel) or by sequence conservation (right panel). Red positions are maximally conserved compared to hERAP1, whereas blue positions are not conserved (Holm and Rosenstrom, 2010). The predominant and intense red colouring together with the few pale blue areas in the left panel reflect the high structural homology of SpWss1b and hERAP1. Amazingly, the conserved HExxH-motifs superimpose at almost identical positions at the end of the active site helix (indicated by a green bar) (Iyer et al., 2004). As a member of the M1 family of zinc metallopeptidases, hERAP1 coordinates the catalytic metal ion via a HExxHx(18)E motif (Rawlings et al., 2010), which distinguishes it from SpWss1b with its HExxHx(5)H motif. By contrast to structural resemblance, sequence conservation between both domains is far less pronounced. The identical residues account for only 16% as illustrated by the positional colouring with pale red and blue in the right panel.

Thus, the results of the DALI search underpin the predicted role for SpWss1b in proteolytic degradation pathways though indicating nuanced divergence from ScWss1 function. In case SpWss1b is functionally categorized as SUMO-isopeptidase, it would feature a unique fold, so far unknown for this class of enzymes.

6.2.4 SpWss1 Phenotyping

Despite the homology between ScWss1 and SpWss1a as well as SpWss1b, the exact function of the latter two proteins remains elusive. For their initial functional characterization a reverse genetics approach was implemented by phenotypic analysis of the respective *S. pombe* single and double knockout mutants in view of the relation between SUMO-modification and DNA damage response. In a genome wide analysis of single gene deletion mutants of *S. pombe* both SpWss1a and SpWss1b were identified as nonessential genes under standard growth conditions (Kim et al., 2010). The average relative fitness of the deletion mutants was monitored by pooled growth experiments, which revealed no significant defects for the Δ*wss1a* deletion strain, since it was allocated to the fastest 5 % of haploproficient genes. By contrast, the Δ*wss1b* mutation was assigned to the 12 % of slowest growing deletion strains, thus indicating mild haploinsufficiency. However, impacts of stressors on the individual growth phenotype of the null mutants of both SpWss1 homologues have not been reported by now. Furthermore, the internal effects of a pooled growth culture on the growth rate of an individual strain are unclear. Therefore, both deletion strains (SpΔ*wss1a* and SpΔ*wss1b*) have been investigated individually under defined environmental stress conditions. Moreover, two double mutants have

been constructed (SpΔ*wss1a*Δ*wss1b* and SpΔ*pmt3*Δ*wss1b*) for the detection of putative genetic interactions. (Pmt3 is the term for the SUMO-homologue in *S. pombe*.)

Individual haploid deletion mutant strains were purchased from Bioneer Corporation. Within in these mutants, target ORFs are replaced by a deletion cassette module containing the KanMX4 selection marker gene, which confers resistance to Geneticin (G418). Double mutants were generated as described in the materials and methods section. In brief, Sp*wss1b*/h$^+$ was backcrossed with wildtype *S. pombe*/h$^-$ for mating type switching. Tetrads were dissected using a micromanipulator and spores were analyzed for Geneticin resistance. After that, the mating type of G418-resistant clones was determined by the iodine staining method. The resulting SpΔ*wss1b*/h$^-$ strain was crossed with both SpΔ*wss1a*/h$^+$ and SpΔ*pmt3*/h$^+$. Tetrads were inspected with regard to the genetic segregation pattern of the 2 G418-resistance markers, which is illustrated for the SpΔ*wss1a*Δ*wss1b* double mutant in Table 7.

parental ditype (no recombination)	tetra type (1 recombination)	nonparental ditype (2 recombinations)
Δ*wss1a*	Δ*wss1a*	Δ*wss1a*Δ*wss1b*
Δ*wss1a*	Δ*wss1b*	Δ*wss1a*Δ*wss1b*
Δ*wss1b*	Δ*wss1a*Δ*wss1b*	WT
Δ*wss1b*	WT	WT

Table 7:
Genotypic segregation pattern for the crossing of SpΔ*wss1a* and SpΔ*wss1b* strains. Since both strains contain the same selection marker, double mutants can only be identified from the nonparental ditype upon growth comparison on nonselective and selective medium. WT: wildtype.

For the nonparental ditype only 2 of the 4 spores contain the Geneticin-resistance markers due to 2 preceding genetic recombinations. Hence, double mutants can be unambiguously identified by comparison of the growth behavior of the 3 genetic types on G418 selective medium (Figure 18). A parental ditype was never observed for any of the performed crossings.
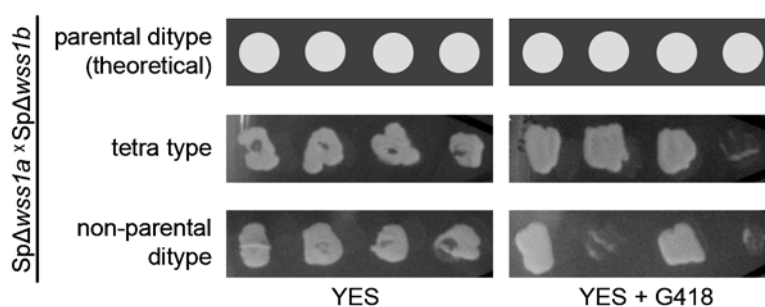
Figure 18:
Growth behavior of the 3 recombination types on nonselective (YES) and selective medium (YES + G418). Wildtype progeny are unable to grow on YES + G418.

Single and double mutants were investigated for both temperature sensitivity and susceptibility to DNA damage as described in the materials and methods section. Shortly, deletion strains were grown to mid log-phase, equal amounts of cells were harvested, washed with sterile saline, plated onto solid medium and finally treated with the respective environmental stimulus. None of the applied conditions provoked a significant phenotype in any of the examined deletion strains (Figure 19). Both SpΔ*wss1a/b* single mutants as well as the double mutant do not display sensitivity to heat shock or DNA damage caused by UV light or hydroxyurea. Remarkably, SpΔ*pmt3* exhibits a strong phenotype only for hydroxyurea, contradicting a previous study (Tanaka et al., 1999), which demonstrated SpΔ*pmt3* phenotypes also for 30°C and 36°C. Such a phenotype

was not reproducible with the strain used in this work. The susceptibility to
hydroxyurea of the SpΔpmt3Δwss1b double mutant obviously originates from
pmt3 deletion.
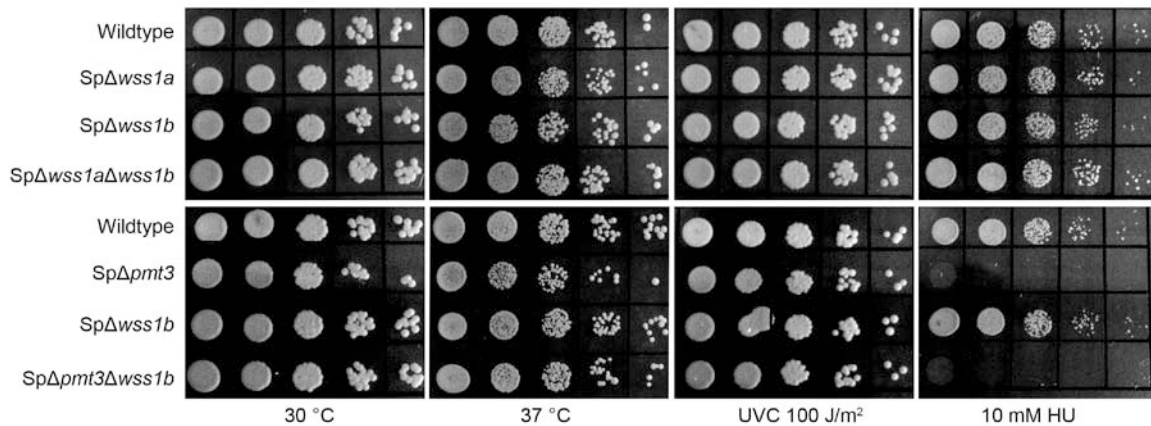
Figure 19:
Phenotypes of various *S. pombe* deletion strains. Disrupted genes are indicated on
the left. The respective growth condition is given at the bottom. Hydroxyurea was
directly added to the medium. UVC exposure was performed immediately after cell
spotting.

In collaboration with the group of Prof. Jentsch (Max Planck Institute of
Biochemistry, Munich) a complementation assay was performed using both
individual *S. pombe* Wss1 homologues for recovery of the conditional *S.
cerevisiae* Δwss1 phenotype (Figure 20). ScΔwss1 shows sensitivity to both
elevated temperature and hydroxyurea treatment (empty vector). Plasmid-borne
wildtype ScWss1 can partly restore the deletion mutant's growth defect, whereas
a H115A loss-of-function mutation causes lethality of ScΔwss1 under the
restrictive conditions. Even at 30°C ScWss1 H115A impairs the growth of
ScΔwss1.
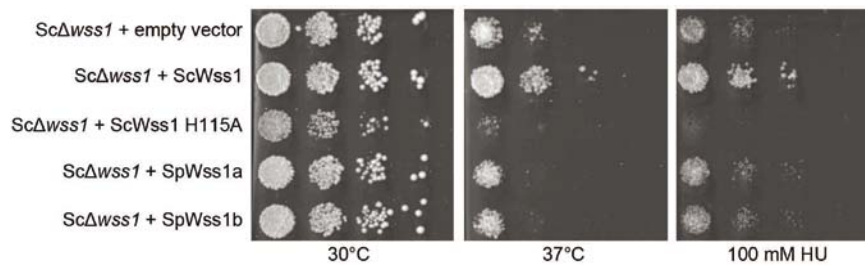
Figure 20:
Complementation phenotypes of a ScΔ*wss1* strain. The plasmid-borne complementation element is indicated on the left. The growth condition is given at the bottom.

Episomal SpWss1a and b, respectively, do not suppress the heat shock phenotype. For hydroxyurea exposure only marginal complementation is observed. These results demonstrate that both *S. pombe* Wss1 homologues cannot restore *S. cerevisiae* Wss1 function for the tested conditions.

6.3 Discussion

SUMOylation is a dynamic process controlling diverse cellular events including transcriptional regulation, nuclear transport, cell cycle progression, DNA-repair and signal transduction pathways (Kim and Baek, 2009). Over the past decade, many scientific investigations have concentrated on SUMO-modification, since it represents an important regulatory mechanism for protein function and localization. In contrast to the complex Ubiquitin pathway (Hershko et al., 2000), SUMOylation employs only a single conjugating enzyme, Ubc3 (Gong et al., 1997), and a small number of ligases (Johnson and Gupta, 2001; Kahyo et al., 2001; Pichler et al., 2002). Accordingly, only two SUMO-specific proteases in yeast (Li and Hochstrasser, 1999; Li and Hochstrasser, 2000) and six in human have been identified up to now (Gong et al., 2000; Yeh et al., 2000). SUMO-deconjugating enzymes are cysteine proteases possessing a conserved catalytic domain, which features the catalytic triad (histidine, aspartate, cysteine) and a conserved glutamine residue required for the formation of the oxyanion hole in the active site (Li and Hochstrasser, 1999). A bioinformatic study predicted novel Zincin-like metalloproteases with a potential role in deSUMOylation (Iyer et al., 2004). Based on the homology to the putatively globular domain of ScWss1p, this new class was designated as WLM-family (Wss1p-like metalloproteases). Recently, it was reported that ScWss1 physically binds SUMO (Smt3 in *S. cerevisiae*) and displays *in vitro* isopeptidase activity on poly-SUMO chains (Mullen et al., 2010). Furthermore, ScWss1 was implicated in Ubiquitin metabolism on the basis of its physical association with proteasomal subunits as well as its unconventional deubiquitination ability. Hence, ScWss1 represents the first case of a presumed Zincin-like metalloprotease involved in an Ubiquitin

signaling pathway. In this work, a ScWss1 homologue from *S. pombe* was structurally and functionally characterized (Figure 8 and Figure 11), since multiple attempts for heterologous expression and purification of ScWss1 failed.

The crystal structure of SpWss1b reveals a compact and globular overall fold of the catalytic domain (Figure 15), consistent with the bioinformatic prognosis of a segregated α/β structure similar to Zincin-like metalloproteases (Iyer et al., 2004). The atomic model also confirms both the 1H-NMR folding analysis as well as the secondary structure prediction by Jalview, suggesting them as reliable tools for the preliminary estimation of crystallization tendency. The overall structure shows a clear spatial distance between the active site and the C-terminus of the short WLM-domain, implying self cleavage of the corresponding C-terminal fragment in *trans*. The structure of both terminal domains of SpWss1b was not accessible in this work. The N-terminal 75 amino acids are predicted to form an Ubiquitin-like domain (Matsuyama et al., 2006; Wood et al., 2002) (http://www.uniprot.org/uniprot/ O94580), hence proposing participation of SpWss1b in proteasomal degradation pathways. A C-terminal SUMO-Interaction-Motif (SIM) in *S. cerevisiae* Wss1 (Uzunova et al., 2007) is not visible for SpWss1b (K. Hofmann, personal communication). Altogether, the role of both terminal domains of SpWss1b remains to be investigated, though recognition of substrates or other binding partners is reasonable.

The active site comprises the conserved HExxHx(5)H-motif, coordinating the central metal ion (Figure 16), thus supplying strong structural evidence for the categorization of Wss1 as a metalloprotease. A TXRF-analysis prior to crystal structure determination detected stoichiometric amounts of Ni^{2+}-ions in a homogenous preparation of SpWss1b. Moreover, an anomalous data set of the

respective crystal was collected at the Ni-absorption edge, followed by Ni-site identification during the course of data processing. These findings prove the presence of a Ni-ion in the predicted Zn-binding motif. However, a purification strategy avoiding a Ni^{2+}-IMAC column yielded crystals under significantly different conditions, pointing towards altered protein traits which may have arisen from a putative metal ion exchange in the active site. Such a scenario is conceivable due to the high abundance of Ni^{2+}-ions on the respective NTA-resin and the obvious surface exposure of the active site. The Ni^{2+}-ion is octahedrally coordinated by the 3 histidines of the HExxHx(5)H-motif, two water molecules, saturating free coordination sites, and 1 unidentified 2-atomic molecule (Figure 16), which most likely is a superoxide anion. Ligand field effects let expect either tetrahedral or trigonal bipyramidal geometry for the Zn-integrating fulllength protein (Christianson, 1991; McCall et al., 2000).

Functional investigations determine a role for SpWss1b in proteolytic degradation pathways, even though a precise classification still remains to be established. A structure based homology analysis with the DALI-server discloses similarity to both amino- and endopeptidases (M1-/M34-family) whereas initial *in vitro* functional characterization experiments indicate endoproteolytic activity only. Self truncation of the C-terminal region of the SpWss1b long WLM-domain (108 - 282) did not reveal a defined target cleavage site but still yielded a stable 16 kDa catalytic core domain. Together with the reduced autoproteolysis of SpWss1b E203Q, a mere thermodynamic protein degradation as well as external protease action can be excluded as a cause for the truncation of SpWss1b. Thus, the monitored *in vitro* self cleavage of SpWss1b might be a relic of an *in vivo* self maturation function (Kay Hofmann, personal communication). A Smt3-

TPR model substrate was randomly cleaved by SpWss1b, resulting in a discontinuous band pattern, which might imply some preference for certain sequence or structure features of the substrate. Apparently, the SpWss1b short WLM-domain does not display a distinctive substrate specificity for the Smt3-TPR fusion protein compared to Ulp1. In Ulp1 the N-terminal domain is important for activity against a substantial fraction of SUMOylated targets (Li and Hochstrasser, 2003). Accordingly, involvement of either the N-terminal or the C-terminal domain of SpWss1b in substrate identification and/or substrate binding is plausible. Moreover, owing to only 70% sequence homology between Smt3 (SUMO from *S. cerevisiae*) and Pmt3 (SUMO from *S. pombe*), a Pmt3-TPR fusion protein might be more likely to constitute a substrate for SpWss1b. However, a poly-Ubiquitin chain as potential target (Kay Hofmann, personal communication) could not be verified experimentally. Since the predicted N-terminal Ubiquitin-like domain harbours a well conserved Ile44 patch, inter-actions with proteins containing Ubiquitin associated domains (UBAs) or Ubiquitin interacting motifs (UIMs) are conceivable (Kay Hofmann, personal communication). A comparison of architecture forecasts supports the idea of dis-tinct functions for SpWss1b and ScWss1. On the one hand, ScWss1 possesses a C-terminal SUMO interaction motif (SIM), which is absent in SpWss1b. On the other hand, ScWss1 lacks the N-terminal Ubiquitin-like domain found in SpWss1b. These observations reflect the general deviations in the modular design of WLM proteases (Kay Hofmann, personal communication). Thus, the exact function of a WLM-domain containing enzyme is most likely determined by its flanking regions. Nevertheless, evolutionary conservation of these flanking regions among fungi indicates roles in the Ubiqutin Proteasome System (UPS).

Besides the initial *in vitro* exploration of SpWss1b protease function, corresponding *S. pombe* deletion strains were examined for response to environmental stress conditions, namely heat shock and DNA lesion. Previous studies report sensitivity to UV irradiation of a ScΔ*wss1* disruption mutant (Birrell et al., 2001; O'Neill et al., 2004), whereas the loss of Wss1 alone does not result in an obvious growth defect of *S. cerevisiae* under standard conditions. Furthermore, integration of Wss1 in DNA damage response pathways was suggested (O'Neill et al., 2004). However, neither individual deletion of each *S. pombe* Wss1 homologue, nor the according double mutant showed evident growth phenotypes when tested against elevated temperature, UV irradiation and HU treatment. Inconsistent with a published SpΔ*pmt3* phenotype (Tanaka et al., 1999), the Pmt3-deletion strain used in this work was only susceptible to hydroxyurea, pointing towards strain dependency of the respective phenotype.

In addition to *S. pombe* knockout analysis, SpWss1a and b were investigated for complementation of the conditional ScΔ*wss1* phenotype. Yet, both *S. pombe* homologues were not able to suppress the conditional growth inhibition of ScΔ*wss1*, presumably reflecting the evolutionary distance between *S. cerevisiae* and *S. pombe* (Sipiczki, 2000).

In conclusion, no direct relation of the 2 *S. pombe* Wss1 homologues to DNA damage response pathways was detected in initial experiments of this work. Apparently, *S. pombe* is able to compensate for a loss of both genes even under stress conditions. Thus, a genome wide double mutant screen should be carried out, to shed light on the physiological roles of SpWss1a and b, respectively. Furthermore, additional *in vitro* investigations should clarify their exact enzymatical properties.

7 The FNR:Tic62 Complex

7.1 Introduction - The Role of FNR and Tic62 inside the Chloroplast

Plants, algae and many species of bacteria exploit the energy from sunlight to convert carbon dioxide into organic compounds in a biochemical process known as photosynthesis. In the light-dependent reactions photons are absorbed by the photosynthetic reaction centres, which are localized inside specialized organelles, the chloroplasts. The energy is used to hydrolyze water, thereby releasing electrons and protons. Linear electron transport (LET) reactions forward the electrons along through a series of large multiprotein complexes embedded in the thylakoid membrane to Ferredoxin (Fd). The final step of LET is catalyzed by the ubiquitous key photosynthetic enzyme Ferredoxin-NADP(H) Oxidoreductase (FNR), which takes over two electrons from reduced Fd and transfers them via its noncovalent cofactor FAD (flavin adenine dinucleotide) to $NADP^+$. FAD functions as an 1 to 2 electron switch, since the 2 electrons are supplied by 2 independent Fd molecules (Mulo, 2011). In this reaction FNR generates the reduction equivalents (NADPH). The concomitantly produced proton gradient between the thylakoid lumen and the chloroplast stroma is used to synthesize ATP as energy carrier. Reducing power (NADPH) and chemical energy (ATP) are mostly employed for carbon fixation in the Calvin-Benson cycle (Benz et al., 2010).

FNR proteins predominantly occur in 2 different tissues, allowing classification into 2 groups: leaf-type (photosynthetic) and root-type (nonphotosynthetic) FNRs. Both groups contain many isoforms (Green et al., 1991; Gummadova et al., 2007; Hanke et al., 2005; Okutani et al., 2005). In contrast to leaf-type FNRs,

which oxidize Fd, the nonphotosynthetic root-type FNRs preferably catalyze the reduction of Fd (Carrillo and Ceccarelli, 2003).

Principally, FNR is a soluble protein, however it was also found to be associated with the thylakoid membrane (Shin et al., 1963). Over the last three decades, several potential FNR binding partners have been discussed, which might be involved in membrane attachment of FNR, including subunits of Photosystem I and the $Cytb_6f$ complex (Matthijs et al., 1986; Zhang et al., 2001). Nevertheless, no conclusive biochemical evidence for a direct interaction with FNR was provided for any of them. It was demonstrated recently that FNR interacts directly and specifically with a conserved amino acid motif found in two different proteins, leading to membrane association of FNR into high molecular weight complexes. One of these proteins, Tic62, was originally identified as a member of the Tic complex (Translocon at the inner envelope of chloroplasts) involved in redox regulation of protein import into chloroplasts (Kuchler et al., 2002; Stengel et al., 2008). The N-terminal NADPH-binding domain of Tic62 switches its conformation according to the chloroplastic NADPH/ $NADP^+$ ratio. The latter also determines the localization of Tic62 either at the inner membrane or in the stroma as well as the binding of FNR by the C-terminal domain. Thus, via the interaction with FNR, Tic62 might act as a redox sensor for chloroplast protein import by transmitting information about the redox state, generated mostly by the photosynthetic apparatus, to the translocon at the inner envelope. (Kovács-Bogdán et al., 2010; Stengel et al., 2008)(Figure 21).
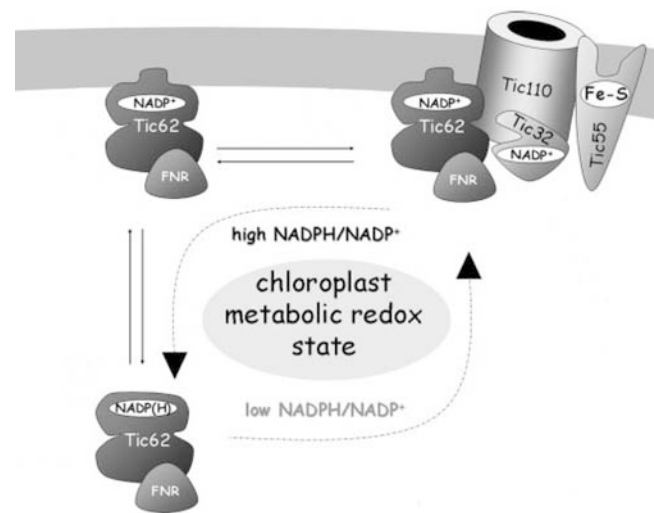
Figure 21:

Tic62 shuttling at the chloroplast inner envelope membrane (Stengel et al., 2008). Depending on the redox state (NADPH/NADP$^+$ ratio) Tic62 either prefers binding to the Tic complex or release into the stroma. Reducing conditions provoke stronger FNR association to Tic62. Alternative membrane binding of Tic62 is also indicated.

Tic62 was also found to represent a major FNR interaction partner at the thylakoids, and binding to Tic62 clearly increases the stability of FNR (Benz et al., 2009). The specific interaction with FNR is mediated by a conserved sequence motif rich in proline and serine residues, located in the C-terminus of Tic62 (Kuchler et al., 2002; Stengel et al., 2008). Interestingly, this motif is restricted to Tic62 proteins from vascular plants (Balsera et al., 2007), and it occurs in different numbers dependent on the respective plants species. Additionally, a second protein containing the Ser/Pro rich FNR binding motif has been recently identified in *Arabidopsis thaliana* and named Trol (thylakoid rhodanese-like protein). It represents an integral membrane protein located in the thylakoids and contains a single FNR-interacting domain at the C-terminus, which was shown to act as an FNR anchor similar to Tic62 (Juric et al., 2009).

Since the publication of the first high resolution FNR structure (Karplus et al., 1991), further atomic models have been described for many species (Karplus and Faber, 2004). Generally, FNR proteins are composed of 2 distinct domains connected by a long loop (Dorowski et al., 2001). The N-terminal domain binds the FAD-cofactor and consists of a 6-stranded, antiparallel β-barrel covered by an α-helix. The substrate $NADP^+$ is accommodated in the C-terminal domain, which features a central 5-stranded parallel β-sheet surrounded by 6 α-helices (Figure 22, left panel). Crystal structures of FNR:ligand complexes with its substrates NADP(H) and Fd demonstrated that both molecules bind in close vicinity to the active site of FNR (Deng et al., 1999; Kurisu et al., 2001)(Figure 22).
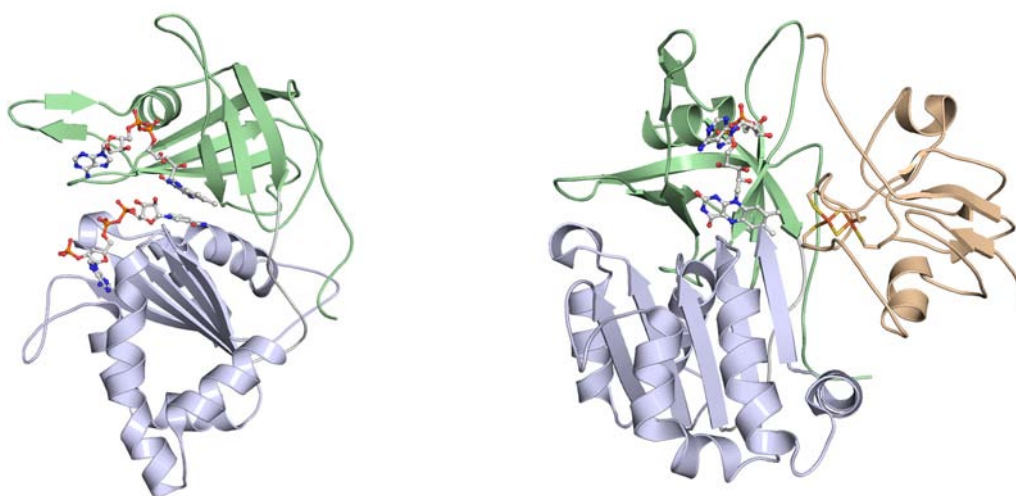
Figure 22:
Crystal structures of FNR in complex with NADP(H) (left) and Fd (right). The FAD-binding domain is coloured in green and the NADP(H)-binding domain in blue. Fd is coloured in orange with the iron sulfur cluster depicted as sticks (right).

NADP(H) binding causes side chain movement of the C-terminal tyrosine residue, which serves as a substrate sensor and the relative position of $NADP^+$ changes slightly in the FNR-complex. Fd predominantly binds via electrostatic

interactions, which play a dominant role in determining the orientation of the two proteins and in stabilizing the complex. Binding of Fd likewise induces slight structural changes in FNR, mostly involving a loop in the FAD domain, allowing the formation of the salt bridges between FNR and Fd.

7.2 Results

7.2.1 Database Analysis of the FNR-binding Domain

In previous studies it was demonstrated that the C-terminal domain of the 2 proteins Tic62 and Trol harbours a conserved sequence motif which is able to bind specifically to FNR, thus mediating its attachment to the thylakoid membrane (Benz et al., 2009; Juric et al., 2009; Kuchler et al., 2002; Stengel et al., 2008). For the selection of a suitable peptide fragment, that might serve as an oligomerization platform for FNR, the C-terminal region of Tic62 and Trol was first characterized by help of a database analysis. For this purpose, a stretch of 58 amino acids from the pea Tic62 C-terminus (amino acids 354 - 411) containing the Ser/Pro-rich conserved sequence motif (henceforth called the FNR-Membrane-Recruiting-Motif (FNR-MRM)) was used as a template for a search in all nonredundant databases via tblastn (Altschul et al., 1990). The conserved motif was found exclusively in vascular plants, either belonging to Tic62 proteins, corroborating results from an earlier study (Balsera et al., 2007), or to Trol homologs (Figure 23). In all Tic62 proteins identified to date at least 2 FNR-interacting repeats are present, the highest number of repeats (7) being present in *Lycopersicon esculentum*. Tic62 from *Pisum sativum*, which was used in this study, harbours 3 FNR-binding motifs. In contrast, almost all Trol proteins comprise only 1 FNR-MRM, except the monocotyledons *Oryza sativa*, *Zea mays*, and *Triticum aestivum* which contain 2 FNR binding repeats. Thus, the FNR-MRM is restricted to vascular plants, rendering this sequence a specific feature for this class of photosynthetic organisms.

Figure 23:

Alignment of the conserved motif in Tic62 and Trol from vascular plants with ClustalW2 (Larkin et al., 2007). Abbreviations stand for At: *Arabidosis thaliana*, Le: *Lycopersicon esculentum*, Vv: *Vitis vinifera*, Sm: *Selaginella moellendorffii*, Mt: *Medicago trunculata*, Tp: *Trifolium pratense*, Ps: *Pisum sativum*, Gm: *Glycine max*, Pt: *Populus trichocarpa*, Rc: *Ricinus communis*, Os: *Oryza sativa*, Zm: *Zea mays*, Ta: *Triticum aestivum*, Lj: *Lotus japonicus.* (Alte et al., 2010)

Alignment of all conserved FNR-MRMs applying the ClustalW2 program (Larkin et al., 2007) (http://www.ebi.ac.uk/Tools/clustalw2/index.html) revealed the presence of a "core motif" of 19 amino acids located in the distal C-terminus as shown in Figure 24.

Figure 24:

Alignment of the C-termini of Tic62/Trol-proteins from different vascular plants containing the FNR-MRM. The red frame indicates the strictly conserved core-motif. Abbreviations, Ps: *Pisum sativum*, At: *Arabidopsis thaliana*, Os: *Oryza sativa*, Pt: *Populus trichocarpa*, OsJ: *Oryza sativa subsp. japonica*. The OsJ_04356 sequence is related to a putative uncharacterized protein. (Alte et al., 2010)

Intriguingly, an alternating pattern of hydrophobic/hydrophilic residues can be observed in this strictly conserved region. Conservation is less pronounced in the first 40 amino acids (Figure 23), though an accumulation of Ser and Pro residues is still obvious. Most of the amino acid residues in the FNR-MRM, such as Pro387, Leu388, Ser389, Pro390, Tyr391, Tyr394, Asp/Glu396, Leu397, Lys398, Pro399, Pro400, Ser/Thr401, Ser402, Pro403 and Pro405 are invariable and hence might be essential for FNR-binding (numbers according to PsTic62). Consequently, a synthetic peptide representing the first FNR binding repeat from *Pisum sativum* Tic62 (PsTic62), including the strictly conserved "core motif" (**KTEQPLSPYTAYDDLKPPSSPSPTKPS**) was used for further analysis.

7.2.2 Preparation of the FNR:Tic62-Complexes

PsLFNR and the C-terminal domain of PsTic62, which comprises all 3 FNR-binding motifs (Val346 - Ser534, from now on abbreviated as R3) were prepared in collaboration with the group of Prof. Soll (Chair of Plant Biochemistry and Physiology, LMU). Both proteins were solubly expressed in *E.coli* and purified via Ni-NTA IM-affinity chromatography. To remove contaminants, PsLFNR and R3 were further purified by size exclusion chromatography. Both the FNR:R3-complex and the FNR:peptide-complex were formed by overnight incubation of the components involved at 4 °C and isolated by size exclusion chromatography resulting in homogeneous protein preparation. Figure 25 displays the chromatograms of the size exclusion runs and Table 8 presents the corresponding elution volumes and calculated molecular weights according to the calibration of the size exclusion column.

Sample name	Theoretical MW [kDa]	Elution volume [ml]	Experimental MW [kDa]
PsFNR	35.9	15.3	39.2
R3	21.3	12.8	122.4
PsFNR:R3	129.0 (3:1)	10.7	319.0
PsFNR:peptide	91.7 (2:1)	13.5	87.1

Table 8:

Overview of the theoretical and experimental molecular weights of the two complexes and the respective single components. Theoretical values for PsFNR and R3 were calculated for the expressed constructs *in silico* with the ProtParam tool of the ExPASy Bioinformatics Resource Portal (http://web.expasy.org/protparam/). For the complexes, theoretical values of the monomers were added up according to the oligomer-stoichiometry, which is given in brackets. Experimental values were calculated from the elution volume of the UV-peaks according to the calibration of the size exclusion column.
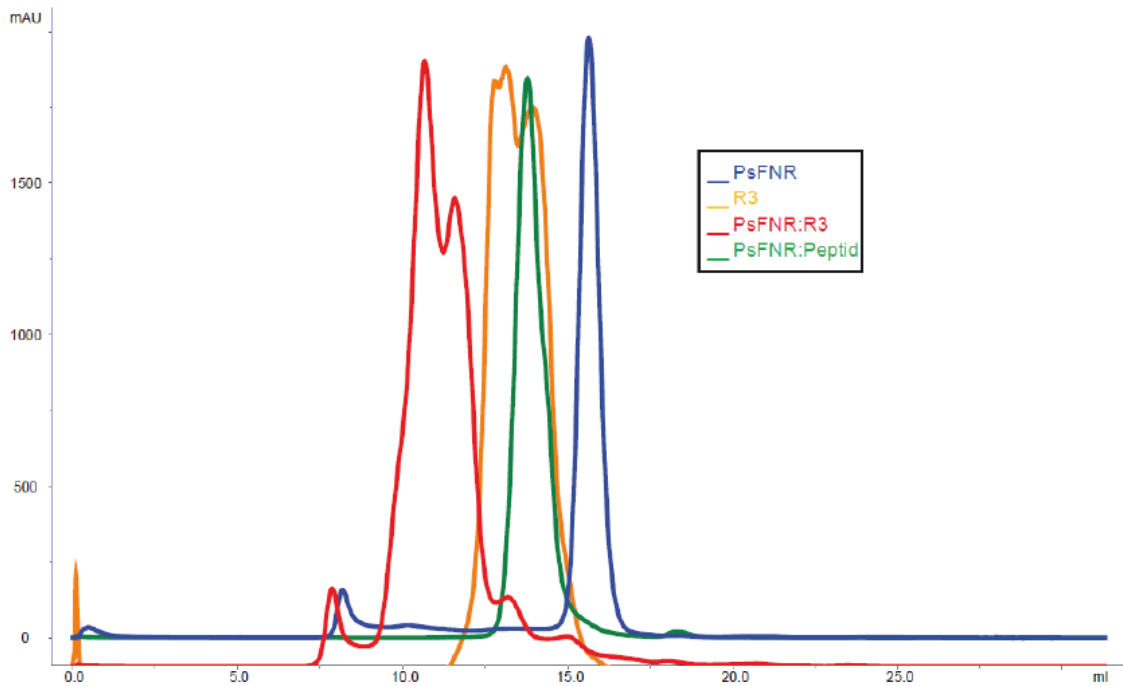
Figure 25:

Purification of PsFNR, R3 as well as the PsFNR:R3 and PsFNR:peptide complexes by size exclusion chromatography. The blue and yellow graphs represent PsFNR and R3 alone, respectively. The red graph marks PsFNR:R3 complex, whereas the green line visualizes the PsFNR:peptide complex. According to the calibration of the size exclusion column the sizes of the proteins and the complexes are calculated as follows: MW(PsFNR) = 39.2 kDa; MW(R3) = 122.4 kDa; MW(PsFNR:R3) = 319 kDa; MW(PsFNR:peptide) = 87,1 kDa. (Alte et al., 2010)

For both monomeric PsFNR and the PsFNR:peptide-complex theoretical molecular weights are consistent with the experimental values. By contrast, the experimental molecular weights for monomeric R3 and the PsFNR:R3-complex differ significantly from the *in silico* values. According to the size exclusion data, the apparent molecular weight for R3 is about 6 times higher and for PsFNR:R3 it is 2.5 times higher than the respective theoretical value. This observation is owed to the fact that size exclusion experiments actually measure the sizes, this means the physical dimensions of protein molecules, which only accord with the actual molecular weights in the case of mainly globular proteins (Rhodes et al.,

2009). Consequently, R3 probably adopts a rather unstructured, elongated conformation, which is plausible with regard to the high proportion of prolines (15 %) in this domain. This assumed R3-conformation may also affect the shape and accordingly the size of the quaternary PsFNR:R3-complex, thus leading to a 2.5 times increase of the experimental molecular weight value compared to the theoretical number. Previous analytical ultracentrifugation analyses disclose a molecular weight of 19.7 kDa for monomeric R3 and 127.8 kDa for the PsFNR:R3-complex, respectively (Benz et al., 2009), which conform well to the theoretical values. Therefore, the size exclusion experiment does not even permit a rough estimation of molecular weights for 2 of the 4 proteins analyzed in this study.

7.2.3 Crystal Structure of the FNR:Tic62-Complex

Initial crystallization trials were carried out for both the PsFNR:R3- and the PsFNR:peptide-complex as described in the material and methods section. In brief, sitting drop high throughput screens were performed by using 96-well format microplates and 5 standard crystal screening kits (Qiagen) on a Phoenix robot (Art Robbins Instruments). The protein concentration was varied from 10 mg/ml to 37 mg/ml and crystal-droplets consisted of 1 volume of reservoir solution and either 1 volume or 2 volumes of protein suspension. PsFNR:R3 did not crystallize under any of the conditions tested, whereas crystals of the PsFNR:peptide-complex grew within three months, with PEG3350 as precipitant. Figure 26 shows a crystal with its typical size of about 200 × 100 × 50 µm^3. The FAD-cofactor of FNR causes the yellow colour.
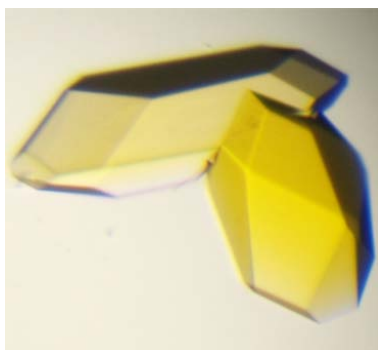
Figure 26:
PsFNR:Tic62peptide-crystal with a typical size of about 200 × 100 × 50 μm^3. The yellow colour is caused by the FAD-cofactor of FNR.

The PsFNR:peptide-complex crystallized in the triclinic space group P1 with the following unit cell parameters: a = 47.5 Å, b = 48.8 Å, c = 71.3 Å; α = 106.6 °, β = 97.0 °, γ = 91.8 °. The structure was determined by molecular replacement (McCoy et al., 2007) using the program PHASER and PsFNR (PDB ID: 1QG0) (Deng et al., 1999) as a search model. The data set was refined to 1.7 Å resolution with the crystallographic CCP4 software package REFMAC (Vagin et al., 2004) using conventional rigid body, positional, and temperature factor methods yielding current crystallographic values of R_{crys} = 13.8 %, R_{free} = 18.9 %, r.m.s. bond length = 0.024 Å, and r.m.s. angles = 1.8°. The 12 N-terminal amino acids of both FNR subunits (termed FNR A and FNR B, respectively) as well as a loop of 7 amino acids (Thr167 - Val173; numbers according to fulllength PsFNR) in FNR B were structurally distorted. The geometry of the whole Tic62-peptide is well defined in the electron density map, except the C-terminal serine. Table 9 gives an overview of the data collection and refinement statistics.

	FNR:Tic62-Peptide
Crystal parameter	
Space group	P1
Cell dimensions	
a, b, c (Å)	47.5; 48.8; 71.3
α, β, γ (°)	106.6; 97.0; 91.8
Molecules per AU[a]	2 FNR; Tic62-Peptide
Data collection	
Beam line	Cu K_α
Wavelength (Å)	1.5418
Resolution range (Å)[b]	65-1.7 (1.8-1.7)
Unique reflections[c]	66902
Completeness (%)[b]	99.9 (99.5)
Redundancy	10.9 (3.9)
R_{merge} (%)[b,d]	3.5 (23.6)
I / σ (I)[b]	23.6 (3.3)
Refinement	
Resolution (Å)	15-1.7
R_{work} / R_{free}[e]	0.138 / 0.189
No. atoms	
Protein	4861
FAD Ligands	106
Water	513
B-factors	16.6
R.m.s. deviations[f]	
Bond lengths (Å)	0.024
Bond angles (°)	1.826
Ramachandran (%)[g]	99.5 / 0.5 / 0.0
PDB accession code	3MHP

Table 9:

Data collection and refinement statistics regarding the FNR:peptide complex.
[a] Asymmetric unit; [b] values in parenthesis of resolution range, completeness, R_{merge} and I/σ (I) correspond to the last resolution shell; [c] Friedel pairs were treated as identical reflections; [d] $R_{merge}(I) = \Sigma_{hkl}\Sigma_j |[I(hkl)_j - I(hkl)] |/[\Sigma_{hkl} I_{hkl}$, where $I(hkl)_j$ is the jth measurement of the intensity of reflection hkl and <I(hkl)> is the average intensity; [e] $R = \Sigma_{hkl} | |F_{obs}| - |F_{calc}| |/\Sigma_{hkl} |F_{obs}|$, where R_{free} is calculated without a sigma cutoff for a randomly chosen 5% of reflections, which were not used for structure refinement, and R_{work} is calculated for the remaining reflections (Brunger, 1992); [f] Deviations from ideal bond lengths/angles (Engh and Huber, 1991); [g] Number of residues in favoured region / allowed region / outlier region

Overall Structure of the Complex

The structure discloses that the FNR:peptide-complex consists of two FNR molecules, which are bound to one peptide (Figure 27). Thereby, the peptide is sandwiched by two FNR monomers, with the two subunits arranged back-to-back in a way that the two FAD-molecules face opposite sides of the complex and are solvent exposed.
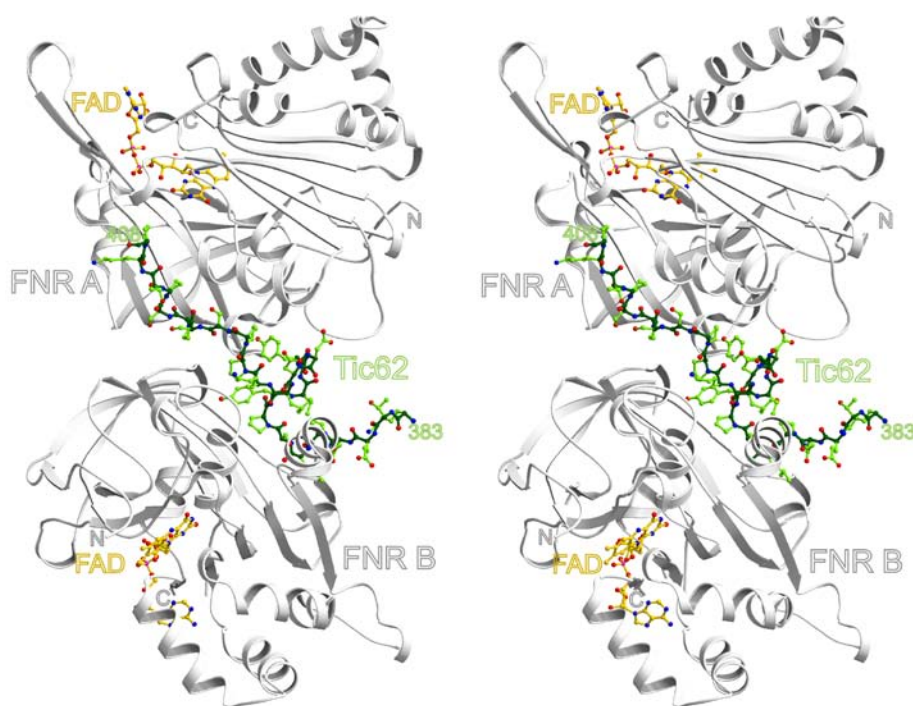
Figure 27:

Stereo view of the two FNR-subunits, shown as grey ribbon plots and denoted as FNR A and FNR B, respectively. The Tic62-peptide, colored in green, and both FAD-cofactors, colored in yellow, are shown as ball-and-stick models. N- and C-termini of the peptide are numbered according to the fulllength Tic62 protein. The image was created using Molscript (Kraulis, 1991) and Bobscript (Esnouf, 1997). (Alte et al., 2010)

The substrate binding sites are located on a level with the C-terminal part of the peptide. Since both FNR monomers are turned by 180°, the central peptide constitutes an imaginary rotational C_2-symmetry axis. Thus, the redox centers of both FADs are accessible for interaction with Fd (Kurisu et al., 2001).

Even though protein-protein-interactions often go hand in hand with considerable structural rearrangements of the molecules involved, such a rearrangement is not observed in the presented case. Comparing the structure of the FNR monomers in the complex and in the free state, the molecules appear like rigid bodies, not showing significant changes in the trace of the backbone, as depicted by backbone superposition of the two FNR-monomers in the complex with the backbone of the free FNR (PDB ID: 1QG0) (Figure 28).
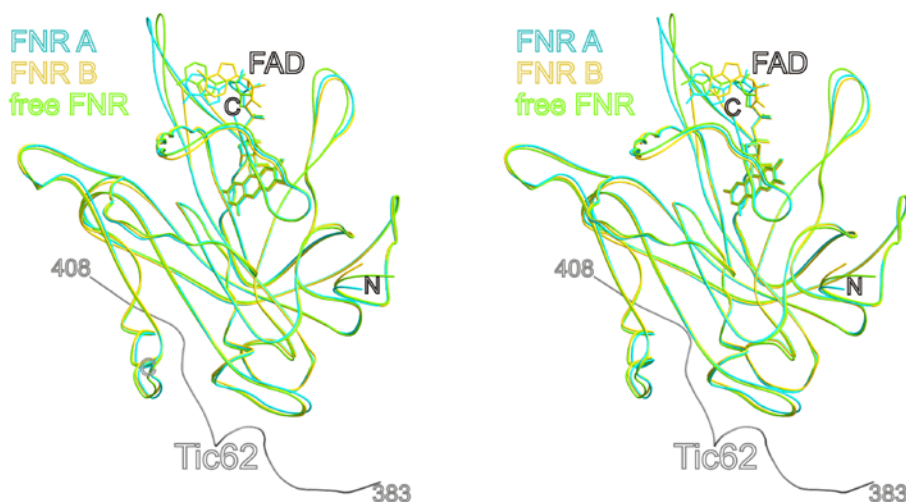
Figure 28:
Superposition of the backbones of free FNR, FNR A and FNR B subunits of the complex as stereo view. Free FNR is colored in green, FNR A in blue and FNR B in yellow. The root mean square (r.m.s.) deviations for the Cα-atoms of the FNR-molecules are < 0.3Å. The trace of the Tic62-peptide is shown as a grey coil. Note, the loop to the left of the AMP-moiety of the FAD-cofactor shows mobility due to a high temperature factor. (Alte et al., 2010)

This also applies to the flavin mononucleotide moiety of the coenzyme, which is rigidly fixed in the active site of all three structures. Only parts of the AMP segment in FAD show variant structural orientations, as they are surface exposed and therefore more flexible compared to the isoalloxazin ring system.

The FNR-domain interacting with the peptide is composed of a twisted 3-stranded antiparallel β-sheet (β1 - β3), 2 associated loops and 2 flanking α-helices (α1 & α2) (Figure 29). The domain forms a shallow "trough shaped" surface groove, which accommodates the peptide without causing structural rearrangements upon ligand binding.
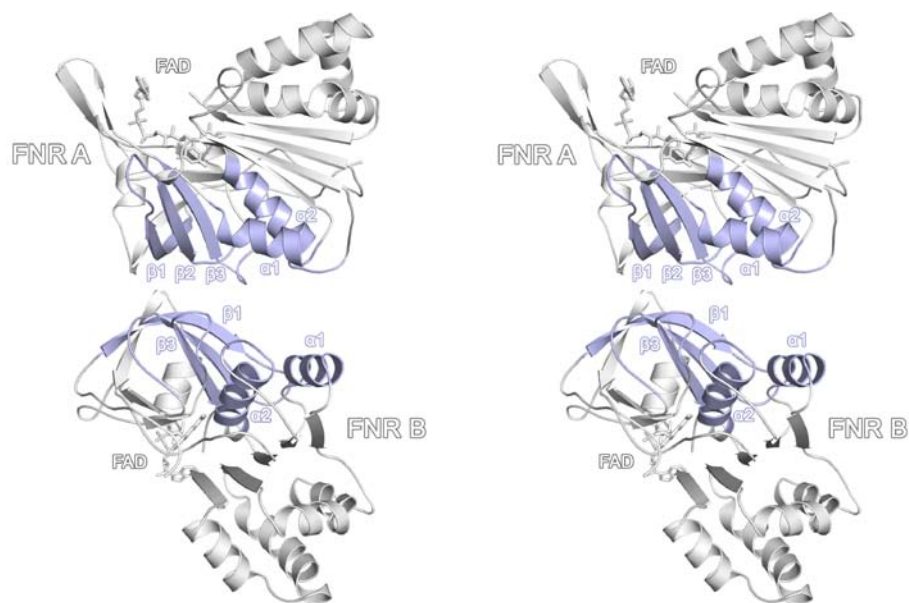
Figure 29:
Stereo view of the two FNR-monomers in the complex depicted as a ribbon plot, showing the FNR-domain that interacts with the Tic62-peptide. The latter is not shown. The FNR-domain consists of a three-stranded antiparallel β-sheet (β1 - β3), two associated loops and two flanking α-helices (α1 & α2). (Alte et al., 2010)

Most interactions between the FNR-domain and the peptide originate from the 2 helices α1 and α2, whereas only few residues of the β-sheet and the associated loops are involved in complex formation. Helix α2 protrudes into the interior of FNR, thus only the bottom winding and partially the adjacent loop interact with the peptide.

The peptide itself does not adopt defined regular secondary structures such as α-helices or β-strands (Figure 27). The trace of its backbone consists of a random series of turns and loops without any apparent symmetric features. Hence, it is rather surprising that the symmetry of the whole complex is generated by a putative asymmetric core module.

Analysis of the FNR-MRM Structure

The conserved FNR-MRM contains about 25% prolines, which suggests a protein-protein interaction mediated by a polyproline motif. It is known that poly-proline ligands feature the conformation of a polyproline type II (PPII) helix when bound to the target protein (Li, 2005; Zarrinpar et al., 2003). However, this has not been identified in FNR-interacting proteins to date. Interestingly, PPII-helices contain an inherent 2-fold rotational pseudo-symmetry, thus, the respective binding domain of putative interaction partners can catch the PPII ligand in 2 possible orientations (Lim et al., 1994). In the FNR:peptide crystal structure, a PPII-conformation is indeed found in distinct peptide sections (Figure 30).
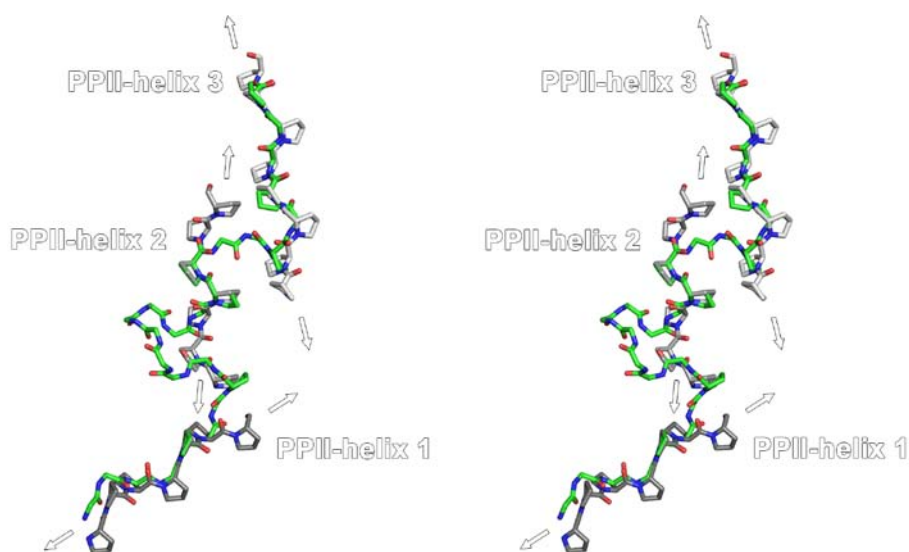
Figure 30:
Structural overlay of the Tic62-peptide with three polyproline type II (PPII) helices (stereo view). Only Pro side chains are shown. The backbone dihedral angles of the PPII-helices are φ = -75° and ψ = 145°. The dihedral angles of the first five amino acids of the Tic62-peptide (segment 1: Lys1 - Pro5) are in the respective range and the backbone widely matches the backbone of PPII-helix 1. The three proline residues 8, 17 and 18 together with Tyr9 and Lys16 of the FNR-MRM form a second axis of a PPII-helix (PPII-helix 2; segment 2: Pro8 - Pro18). The third segment (Pro21 - Pro62) in the FNR-MRM is indicated by PPII-helix 3 (Lim et al., 1994). (Alte et al., 2010)

A structural overlay of a PPII-helix with the peptide uncovered 3 segments that adopt a PPII helical conformation (segment 1: Lys1 - Pro5; segment 2: Pro8 - Pro18; segment3: Pro21 - Pro26). The axes of all 3 segments point to different directions, and the segments, on their part, are separated from each other by 2 linkers. Linker 1 comprises Leu6 and Ser7, linker 2 consists of Ser19 and Ser20. Interestingly, segment 2 (Pro8 - Pro18) is intercepted by a loop, which consists of the residues Thr10 to Leu15. These loop residues contribute to multiple interactions with both FNR subunits. Such a conformation has not yet been reported for polyproline ligands. Notably, the peptide exhibits 2 features typical for PPII-ligands that are in complex with a SH3-domain (src homology 3). First, the peptide contains a PxxP-motif, which is known to be essential for interactions

with SH3 domains (Zarrinpar et al., 2003). Second, the proline delta carbon (Cδ)

is recognized: the unique position of that atom, which is covalently fused to the

backbone nitrogen, renders PPII-interactions specific. Analysis of the interface of

the complex revealed 5 such contacts, 1 of which is superior: Lys16 and Pro17

of the peptide form a ridge that efficiently fits into a peptide binding surface

groove of FNR B, which is defined by the aromatic residues Phe99 and Trp176

(Figure 31).
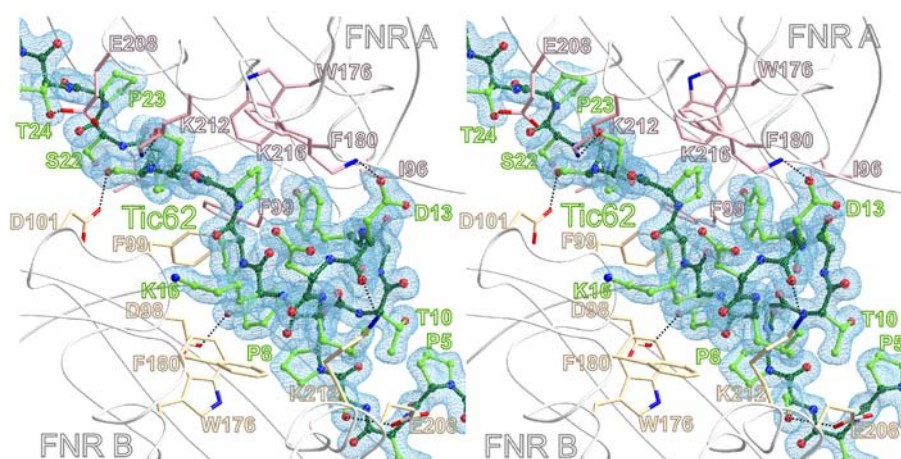
Figure 31:
Stereo view of the 2Fo-Fc electron density map (countered at 1σ) for the Tic62-
peptide in the complex interface, in which the Tic62-peptide has been omitted for
phasing. FNRs are represented in coils and amino acid residues of both FNR
subunits complexing the Tic62-peptide are depicted as sticks. Hydrogen bonds and
a salt bridge are indicated by black dashed lines. Here, the peptide amino acids are
numbered from 1 to 27. (Alte et al., 2010)

All four amino acids involved in this interaction are highly conserved in the

respective proteins among vascular plants. This domain exhibits a novel Proline-

Recognition-Domain-fold (PRD), as domain superpositioning of the respective

FNR-domain does not reveal structural similarity to any of the so far examined

PRDs (e.g. SH3, Profilin) (Li, 2005).

Intermolecular Forces at the Complex Interface

A more detailed analysis of the amino acids participating in complex formation reveals that numerous interactions of both hydrophobic and polar nature contribute to the formation of a stable complex between the FNR-molecules and the peptide: the amino acid composition of the peptide (KTEQPLSPYTAYDDL KPPSSPSPTKPS) holds the potential of creating a hydrophobic core region in the interface, which is complemented by distinct polar interactions. Mainly the large proportion of prolines (Pro5, Pro8, Pro17, Pro18, Pro21, Pro23, Pro26), but also the aliphatic moieties of Leu6, Tyr9, Tyr12, Leu15 and Lys16 in the peptide provide the basis for van der Waals interactions with nonpolar regions of both FNR subunits. In FNR, Ile96, Phe99, Trp176, Phe180 and Tyr206 predominantly contribute to a hydrophobic core (Figure 31). Apart from that, the amino acids Glu208, Lys212 and the backbone oxygen of Phe180 of both FNR A and B subunits are important for the hydrogen binding network in the interface. Additionally, Lys182 and Glu184 of FNR A and Asp98 and Asp101 of FNR B form hydrogen bonds with the peptide. Furthermore, a salt bridge exists between Lys216 of FNR A and Asp13 of the peptide. In addition to the abovementioned special ligand attributes, the specific interactions in the 2 contact regions between the peptide and the 2 FNR subunits contribute to the symmetry of the complex. Particularly, a noticeable number of identical amino acids of both FNR monomers are involved in binding to the peptide, which is crucial for generating the symmetric complex. These residues include Thr43, His53, Phe99, Trp176, Phe180, Tyr206, Glu208 and Lys212, seeming to pull the two FNR monomers into a symmetric conformation. (Figure 31, Table 10).

	K	T	E	Q	P	L	S	P	Y	T	A	Y	D
vdW (FNR A)											I96	E181	E181
h-bond (FNR A)			E184								K182	G100 G97	F180 K216
Peptide	**K**	**T**	**E**	**Q**	**P**	**L**	**S**	**P**	**Y**	**T**	**A**	**Y**	**D**
h-bond (FNR B)				D45		Y206 E208	E208 E209	D98					K212
vdW (FNR B)						T43 K207		I42 H53 Y206		E208			

	D	L	K	P	P	S	S	P	S	P	T	K	P
vdW (FNR A)				F180 W176	W176			F99 L38		Y206 H53			T43
h-bond (FNR A)				K212	K212						E208		
Peptide	**D**	**L**	**K**	**P**	**P**	**S**	**S**	**P**	**S**	**P**	**T**	**K**	**P**
h-bond (FNR B)			F180					D101					
vdW (FNR B)	E208 K212	W176	F99 W176					F99					

Table 10:

Overview of the interactions between the FNR subunits and the Tic62-peptide. Interacting amino acids of the respective FNR subunits are given with the corresponding numbers of the PsFNR-construct used in this study (Met1 omitted). Hydrophobic interactions (van der Waals) are depicted in blue, hydrogen bonds in pink. Note, the sole salt bridge is coloured in green. Due to structural distortion, Ser27 of the Tic62-peptide is omitted. (Alte et al., 2010)

Surface Properties of the Complex

Next, the contact area of both FNR molecules involved in dimerization was analyzed. Interestingly, the presence of the peptide leads to an enormous increase of the contact region. Without the peptide, the theoretical contact surface between the two FNR subunits is restricted to 380 $Å^2$, as calculated *in silico* on the EBI-PISA website (Krissinel and Henrick, 2007). This area is only formed by a small patch comprising the amino acids 35 to 40, 57, 99 to 104, 135 to 137 of both FNR subunits and a salt bridge between Glu215 (FNR A) and Lys182 (FNR B) (Figure 32). Nevertheless, a large cavity remains between the two FNRs due to steric interference.
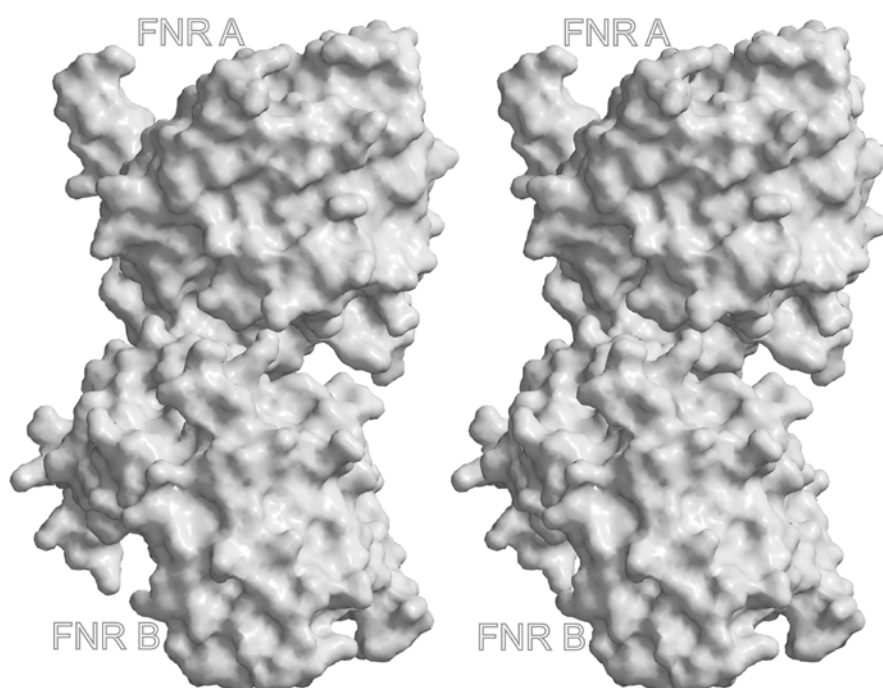
Figure 32:

Stereo view of both FNR subunits in the complex without the Tic62-peptide. This surface representation was created using GRASP software (Nicholls et al., 1991). (Alte et al., 2010)

In the complex structure, this cavity is filled by the peptide, which enlarges the contact surface area to 2070 Å^2 in total (Figure 33). Thus, the surface between FNR and the peptide is about 900 Å^2 and about 790 Å^2 for FNR A and B, respectively, which induces the assembly and stabilizes the ternary complex.
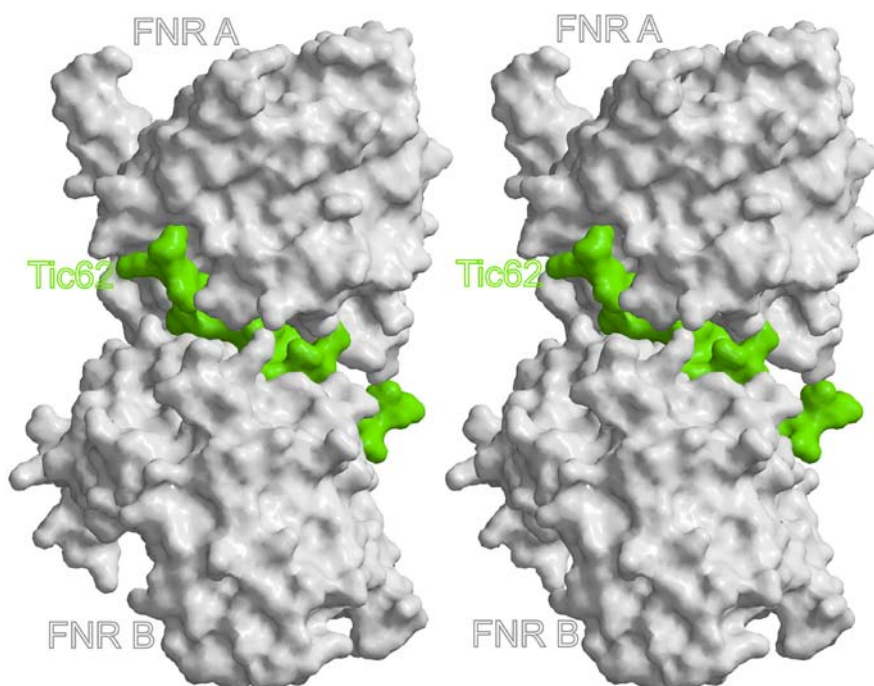
Figure 33:
Stereo view of both FNR subunits in the complex with the Tic62-peptide, which is colored in green. The FNR-MRM fills a large cavity between the two FNR-molecules, thereby significantly expanding the contact surface. This surface representation was created using GRASP software (Nicholls et al., 1991). (Alte et al., 2010)

Calculated values of the solvation free energy gain (Krissinel and Henrick, 2007) for the respective FNR molecules upon complex formation indicate that FNR B (-7.5 kcal/mol) shows a slightly stronger binding to the peptide than FNR A (-6.9 kcal/mol). Thus, a consecutive binding mode could be hypothesized by specific interactions in the respective interfaces. A structural rearrangement of the side chains in FNR A, induced by the previous binding of FNR B to the

peptide, can be excluded as a cause of a putative sequential binding (Figure 34). Thus, although the peptide is asymmetric with respect to its primary sequence, it still acts as a symmetric dimerization module for the two FNR subunits.
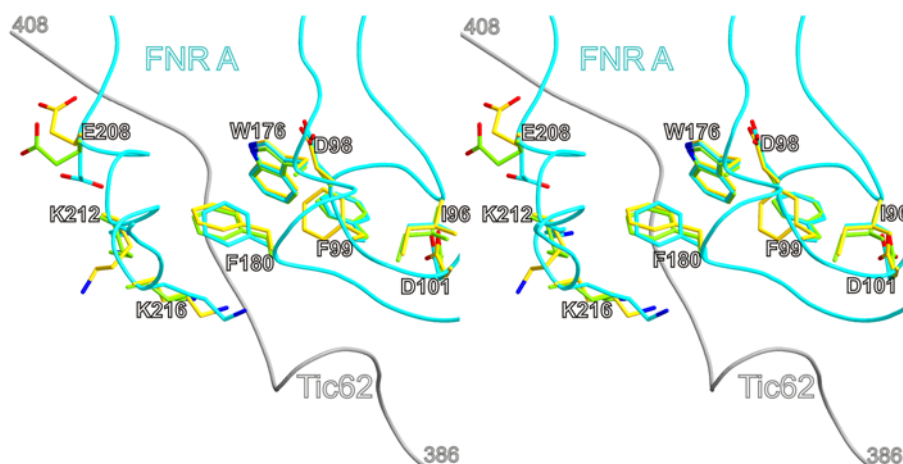
Figure 34:

Structural superposition of amino acids involved in binding of the Tic62-peptide shown in stereo. Color-coding corresponds to Figure 28 and orientations of the molecules are identical to Figure 27. (Alte et al., 2010)

Binding Properties of the Complex

In addition to solving the crystal structure of the FNR:peptide complex, the affinity of the binding partners for each other was determined in collaboration with the group of Prof. Soll. For this purpose, one of the most sensitive methods is Surface Plasmon Resonance (Hoa et al., 2007). To analyze binding of the FNR-MRM to FNR, both the synthetic peptide as well as the whole C-terminus of PsTic62, comprising all three binding motifs (R3), were used for the interaction studies (Kuchler et al., 2002). The FNR-MRM-peptide or R3 were coupled to a CM5 chip using the standard amine coupling procedure (Johnsson et al., 1991). After activation of the chip, as well as binding of the respective ligands and

blocking of unspecific binding sites, FNR was injected at pH 8 and a constant flow rate of 30 µl/min.
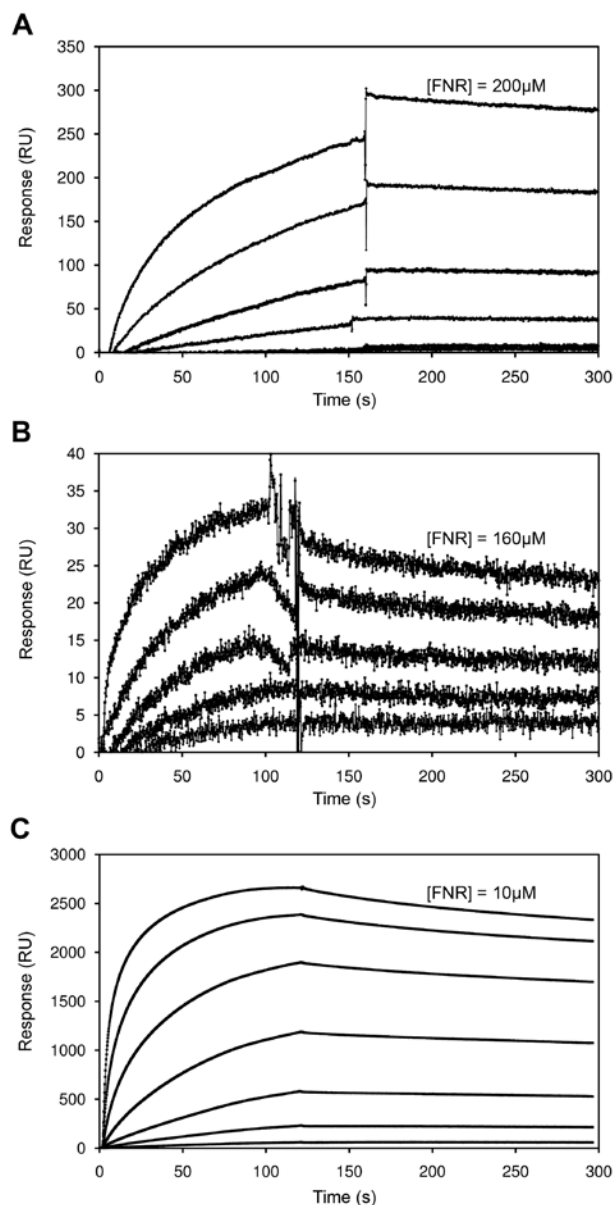
Figure 35:

SPR sensorgrams showing the binding of FNR to either the peptide or the whole C-terminus (R3) of PsFNR. Association and dissociation of FNR to the immobilized ligands were measured at varying FNR-concentrations and pH-values. For the sake of clarity only the highest FNR-concentration is indicated. Association of FNR to the respective ligand is visible by rising RU values, whereas dissociation leads to a decrease. **A** FNR:peptide binding at pH8 ([FNR]: 6.25, 12.5, 25, 50, 100 and 200 µM, respectively). **B** FNR:R3 binding at pH8 ([FNR]: 10, 20, 40, 80, 160 µM, respectively). **C** FNR:R3 binding at pH6 ([FNR]: 0.16, 0.32, 0.64, 1.25, 2.5, 5, 10 µM, respectively). For details of k_a, k_d and K_D see Table 2. (Alte et al., 2010)

An equilibrium dissociation constant of 2.75 ± 0.33 µM was calculated for the peptide and FNR at pH8 (Figure 35A, Table 11) which represents a high affinity, although it has to be noted that the observed association rate was quite slow. The dissociation constant of R3 and FNR at pH8 was similar to that of the peptide, but association and dissociation rates were about 5 times faster (Figure 35B, Table 11). This observation indicates that the number of FNR-binding repeats in Tic62 proteins influences the speed of association/dissociation, but does not change the general affinity for FNR. This can also be deduced from the association curves, which show no cooperative binding effect for R3 when compared to the peptide.

Sample name	K_D ± SD [µM]	k_a ± SD [1/Ms]	k_d ± SD [1/s]
Tic62 peptide (pH 8)	2.75 ± 0.33	$1.12 * 10^2 ± 0.31 * 10^2$	$3.11 * 10^{-4} ± 1.16 * 10^{-4}$
R3 (pH 8)	3.4 ± 1.33	$6.18 * 10^2 ± 3.55 * 10^2$	$1.31 * 10^{-3} ± 3.75 * 10^{-4}$
R3 (pH 6)	0.041 ± 0.48	$1.82 * 10^4 ± 0.62 * 10^4$	$4.6 * 10^{-4} ± 5.16 * 10^{-5}$

Table 11:
Overview of the association and dissociation constants measured by SPR. Standard deviations were calculated from at least three independent experiments. (Alte et al., 2010)

Furthermore the potential physiological effects on the binding were analyzed by changing the pH of the binding reaction. Intriguingly, the affinity of FNR to R3 significantly increased upon lowering the pH to 6. Especially the association occurred about 30 times faster at pH 6 compared to pH 8, which led to a dissociation constant differing by a factor of approximately 80 (0.041 ± 0.027 µM) (Figure 35C). Thus, the SPR results demonstrate that FNR has a high affinity to

the binding motif found in Tic62 and Trol, which is strongly increased at acidic conditions.

In the following, the activity of the complex bound FNR was investigated as compared to the activity of the free enzyme in collaboration with the group of Prof. Soll. To this end, FNR activity was measured employing a Cyt c reduction assay (Benz et al., 2009) with varying amounts of FNR (0.5 µg - 2 µg total protein) at pH 8 and pH 6, respectively (Figure 36). As a control, R3 alone was used, which exhibited no activity.
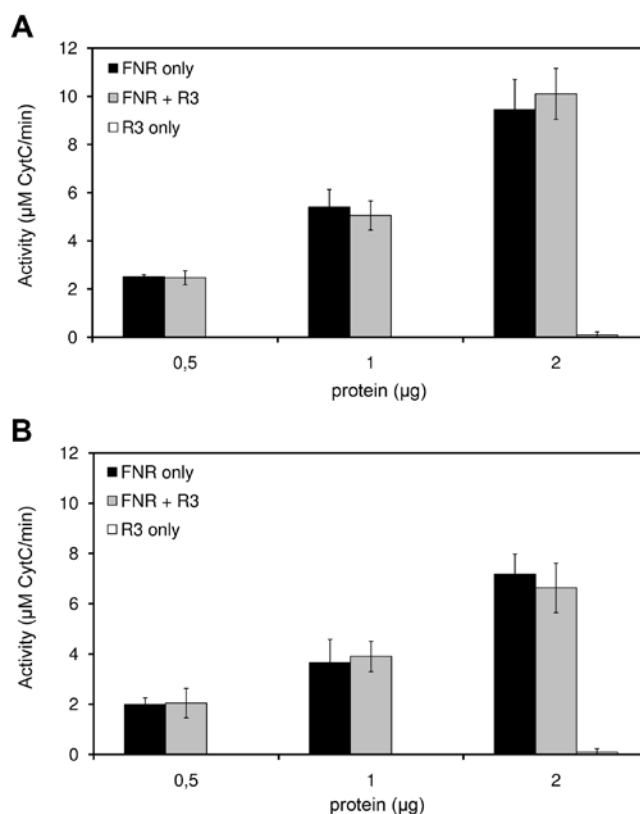
Figure 36:

Activity of FNR and FNR:R3 complexes measured by Cyt c reduction. Activity at pH 8 (**A**) and pH 6 (**B**). Black bars represent FNR alone; grey bars the complex of FNR:R3 and white bars R3 alone as a control, respectively. Data have been collected from at least three independent measurements and error bars are indicated. (Alte et al., 2010)

For both conditions, free FNR displayed a similar performance compared to complex bound FNR, allowing the conclusion that FNR:R3 has the same activity as FNR alone. Lowering the pH in the assay resulted only in a slightly reduced general activity, and no differences in FNR activity of the free and the complexed protein have been observed under this condition as well. These data indicate that the Tic62-peptide functions as a FNR-recruiting motif that leads to dimerization of the FNR while leaving its activity unchanged which conforms to the crystallographic results of the ternary complex.

7.3 Discussion

Identifying FNR-binding proteins at the thylakoid membrane is in central focus of active research, since it remains an open and controversially discussed question how the soluble FNR becomes attached to the thylakoid. Recently, a Ser/Pro-rich domain has been identified in the 2 proteins Tic62 and Trol that was shown to specifically interact with FNR and to be required for its membrane attachment (Benz et al., 2009). In this work, the FNR binding motif was structurally and functionally characterized in molecular detail. Previous data revealed that the FNR-binding domain of Tic62 exclusively exists in vascular plants (Balsera et al., 2007). The results of this work disclose that the integral membrane protein Trol possesses a highly similar FNR-binding motif at its C-terminus (Figure 23 and Figure 24) that is likewise only found in these organisms. Thus, membrane tethering of FNR by this motif seems to be a recent evolutionary invention that occurred only after separation of vascular from nonvascular plants. Hence, while FNR is commonly distributed among all three domains of life, the membrane recruiting components Tic62 and Trol are restricted to plants possessing a vascular system.

The FNR binding motif(s) found in Tic62 and Trol are characterized by a highly homologous core domain of 19 amino acids (Figure 24). Variability increases upstream of the core region, though accumulation of Ser and Pro residues is still evident. Whereas most Trol proteins comprise a single FNR-binding domain, its number varies to a higher extent in Tic62 proteins: 3 repeats can be found in Tic62 from *Pisum sativum*, whereas the *Arabidopsis thaliana* orthologue comprises 4 and in Tic62 from *Lycopersicon esculentum* even 7 FNR-binding domains can be found (Balsera et al., 2007). Interestingly, the binding affinity to

FNR did not change significantly when constructs comprising 1 or 3 FNR-interacting motifs were analyzed (Figure 35 and Table 11). This indicates that binding to each domain occurs independently of the other motifs and excludes cooperative binding effects.

To date, a variety of FNR structures are available, either showing FNR alone or in complex with its substrate NADP(H) and/or Fd. The present work resulted in the first structure of FNR together with a nonsubstrate binding partner, *i.e.* the conserved motif found in Tic62 and Trol. In an earlier study, a hydrophobic cavity opposite to the active site was described for FNR (Bruns and Karplus, 1995). Since exposure of such a feature is highly unusual in a native protein, it was speculated that this hydrophobic region could function in membrane attachment. Several lines of evidence now suggest that FNR is tethered to the membrane by binding to Tic62 (and Trol) rather than by direct membrane attachment in a pH-dependent manner (Grzyb et al., 2008), for example thylakoid binding of FNR is significantly disturbed in the absence of Tic62 (or Trol) (Benz et al., 2009; Juric et al., 2009).

Interestingly, the FNR-MRM was found to bind opposite to the active site of both FNR molecules forming a back-to-back dimer. As found for the complex structures of FNR bound to NADP(H) and Fd, dimerization of FNR upon interaction with the peptide does not induce structural rearrangements (Figure 28 and Figure 34). Even the side chains at the interface exhibit only slight conformational rearrangements and thus the FNR molecules can be regarded as rigid bodies. Hence, the Tic62-peptide seems to mediate self assembly of the FNR dimer only by surface expansion without influence on the active sites.

A striking feature of the FNR-binding motif is the formation of a PPII-like helix (Figure 30) upon complex formation. This type of secondary structure element has often been implicated in protein-protein-interactions in various cytosolic signal transduction pathways and was extensively characterized in SH3 domain proteins (Li, 2005) which are present in all eukaryotes (Rubin et al., 2000). The FNR-MRM in Tic62 and Trol is the first example of a domain forming the PPII conformation in chloroplasts. Tic62 was proposed to play a role in signaling events (Benz et al., 2009; Kuchler et al., 2002; Stengel et al., 2008) by sensing the chloroplast redox state and regulating protein import accordingly. FNR was discussed to participate in this process, although the molecular details of redox related import regulation remain elusive (Benz et al., 2009; Stengel et al., 2009).

The structural results could be corroborated by enzymatic measurements, which showed that binding of the peptide has no effect on the activity of FNR (Figure 36). This clearly differentiates Tic62 binding to FNR from other PPII domains, which have been described to drastically influence the conformation and/or activity of their interaction partners (Groemping and Rittinger, 2005; Takeya and Sumimoto, 2003). However, as the experiments have been performed *in vitro*, it remains to be established if membrane attachment mediated by Tic62/Trol influences the activity of FNR *in vivo*, as was proposed by another study (Grzyb et al., 2008).

The most interesting property of the FNR-Tic62/Trol interaction is the clear difference of the affinity at acidic (pH 6; $K_D \approx 0.04\mu M$) compared to alkaline (pH 8; $K_D \approx 3\mu M$) conditions (Figure 35). Both values indicate a high affinity of FNR and Tic62/Trol, since the binding at pH 8 is similar to *e.g.* the binding strength of a cochaperone to Hsp90 (Brinker et al., 2002). It also reflects the dissociation

equilibria of other PPII proteins with their substrates, which usually range between 1 to 10 µM (Li, 2005). However, the increased binding strength at pH 6 is even in the range of the affinity of monoclonal antibodies for their antigens (Egler et al., 2009) and has not been described for interactions performed by PPII proteins before. Thus, the interaction of FNR with Tic62/Trol seems to have a function distinct from mere signaling. Intriguingly, the pH variations reflect differences of the chloroplast stroma between light and dark cycles (*e.g.* day vs. night) (Figure 37).
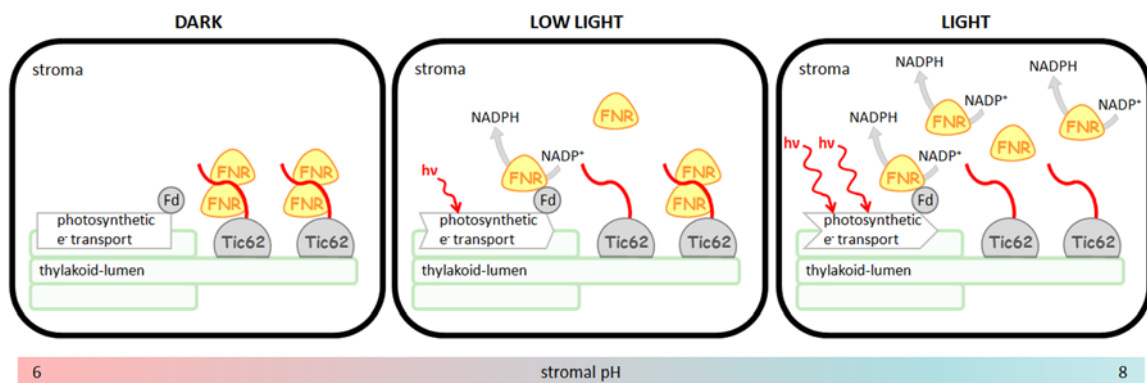
Figure 37:
Schematic model of pH-dependent FNR-storage at the thylakoid membrane by Tic62. During dark periods, when photosynthesis is shut-down, FNR strongly interacts with the Tic62 C-terminus due to an acidic stromal pH. Hence, FNR is attached to the thylakoid membrane (left panel), where it is stored and stabilized until reactivation of photosynthesis. Low light quantities (indicated by a small, red arrow) induce a modest photosynthetic activity, resulting in a higher stromal pH, which causes a partial release of FNR molecules into the stroma (middle panel). Thus, an adequate amount of reduction equivalents (NADPH) is produced. High light conditions (indicated by large, red arrows) evoke high photosynthetic activity, leading to an alkaline stroma, since protons are transported into the thylakoid lumen. Under these conditions, FNR is predominantly found in a Tic62-free form, therefore it is able to mediate the transfer of electrons from ferredoxin (Fd) to $NADP^+$ (right panel). For the sake of clarity, the role of Tic62 in the chloroplast redox shuttling system is not depicted. (Alte et al., 2010)

During light phases, when photosynthetic activity is high, protons are transported into the thylakoid lumen, leading to an alkaline stromal pH. By contrast, when photosynthesis ceases during dark phases the stromal pH decreases again. Under these conditions, Tic62 is predominantly associated with the thylakoid membrane where it recruits FNR into stable high-molecular-weight complexes (Benz et al., 2009). Light catalyses photosynthetic electron flux, however light quantity can vary dramatically during the course of the day, therefore requiring constant adjustment of the light harvesting processes and the enzymatic reactions leading to the formation of NADPH as the end product of photochemistry. Changes in light quantities alter stromal pH and thus the amount of FNR bound to the thylakoids (this work and Benz et al., 2009). Furthermore, the membrane attachment of FNR is influenced by the stromal redox state (*i.e.* the NADPH/NADP$^+$ ratio), which mimics variations in environmental conditions (Stengel et al., 2008). Therefore, reversible attachment of FNR to the thylakoid membrane via Tic62/Trol provides an elegant way to store surplus molecules, not required during *e.g.* low-light/dark periods or particular environmental conditions.

8 The Small Heat Shock Protein Hsp17.7

8.1 Introduction - The Role of Chaperones in the Heat Shock Response

Heat stress causes unfolding and unspecific aggregation of proteins, which results in a general perturbation of the regulated interplay between protein biosynthesis and programmed degradation. Beyond the disintegration of individual proteins, heat stress corrupts the cellular infra structure as a whole. For instance, eukaryotes suffer from damages of the cytoskeleton, breakdown of organelles and intracellular transport systems, nuclear events such as RNA-splicing and even altered membrane composition (Kruuv et al., 1983; Szalay et al., 2007; Toivola et al., 2010; Vigh et al., 2007; Vogel et al., 1995; Welch and Suhan, 1985; Welch and Suhan, 1986; Yost and Lindquist, 1986). Finally, this accumulation of defects severely hampers cell growth and in the worst case results in cell death.

Organisms have evolved sophisticated defence systems. Thus, when they encounter heat stress, proteins from many different functional classes are recruited for the shock response. Besides the molecular chaperones, which constitute a universal protective equipment across all species (Ellis et al., 1989), the overheated cell engages components of several other pathways, such as proteolysis, DNA damage repair, energy metabolism, cell regulation as well as transport and detoxification (Al Refaii and Alix, 2009; Bügl et al., 2000; Jantschitsch and Trautinger, 2003; Malmendal et al., 2006). Unlike the conserved induction of chaperones upon heat shock, the pattern of upregulated genes of all other functional classes varies substantially between different

species, reflecting a species specific set of damage control proteins (Richter et al., 2010).

The molecular chaperones comprise 5 major and broadly conserved families of heat shock proteins: Hsp100s, Hsp90s, Hsp70s, Hsp60s (chaperonins) and small heat shock proteins (sHsps) (Richter et al., 2010). Before a polypeptide chain finally adopts its native 3D conformation, it continuously struggles with unfolding and aggregation even at physiological temperatures (Gragerov et al., 1991; Kerner et al., 2005; Mayer, 2010). Therefore, a permanent presence of chaperones supports protein folding. Hsps accept various kinds of unfolded proteins as substrates by detecting their exposed hydrophobic regions. In addition to mere shielding of nonnative patches, ATP-dependent Hsp-systems actively participate in refolding of clients. These "foldases" include all the above-mentioned families of Hsps, except for the sHsps, and they share a mechanistical principle, in which the binding and hydrolysis of ATP controls the transition between different affinity states of the respective chaperone for its substrate (Richter et al., 2010)(Figure 38, left panel). The sHsps, however, stand out for their sheer "holdase" activity, since they seem to be optimized for efficient binding of nonnative proteins, thus representing an effective first line of defence against heat stress (Richter et al., 2010).

While sHsps represent the most prevalent sort of molecular chaperones, they show high heterogeneity both in sequence and size (Kriehuber et al., 2010; Richter et al., 2010). Nevertheless, the structure of all known sHsp-monomers is characterized by the central α-crystallin domain flanked by variable terminal extensions. In general, sHsps assemble into oligomers, which display wide variations in the number of subunits and their packing symmetry. Moreover, they

also show significantly divergent degrees of order and dispersity (Haley et al., 2000; McHaourab et al., 2009). Previous structural studies revealed that α-crystallin domain dimers are the building blocks for higher oligomers (Kim et al., 1998; Stamler et al., 2005; van Montfort et al., 2001). Within the cellular heat shock response, sHsps associate with unfolded proteins, thereby preventing their aggregation. Since they lack refolding activity, they presumably serve as a storage depot for substrate proteins. Subsequent refolding may occur in cooperation with ATP-dependent chaperone systems such as Hsp100 or Hsp70 (Lee et al., 1997; Mogk et al., 2003). The exact mode of action for sHsps is still enigmatic. Figure 38 (right panel) illustrates possible mechanisms.
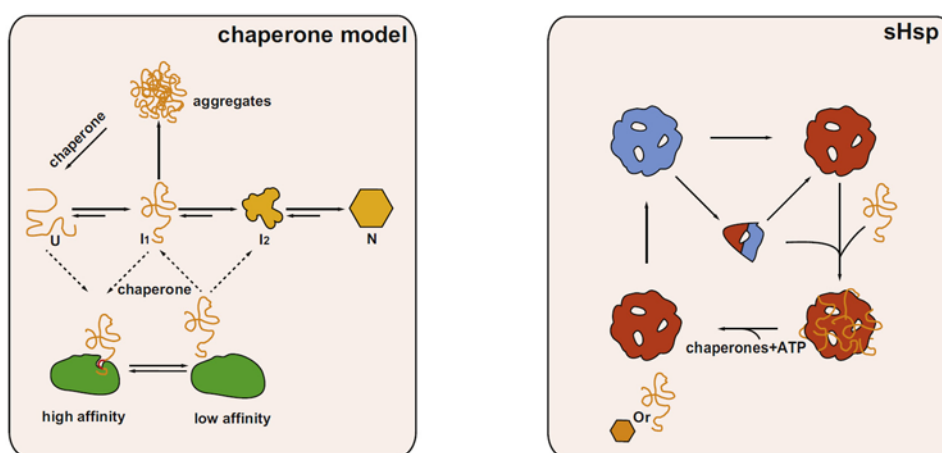
Figure 38:

General chaperone model (left) and suggested sHsp mechanism (right) (Richter et al., 2010). Left: Starting from the unfolded polypeptide chain (U), proteins fold via increasingly structured intermediates (I_1, I_2) to their native form (N). Heat shock presumably provokes the inverse process. Chaperones associate with (partially) unstructured clients. ATP binding and hydrolysis usually induces transition from the high-affinity binding state to the low-affinity release state. Right: Upon heat stress inactive oligomeric sHsp complexes (blue) may either be activated as a whole (red) or break into smaller subunits before binding the substrate and reassembling into larger complexes. Following substrate interaction, protein refolding is accomplished by cooperation together with ATP-dependent chaperone systems.

Previous Characterization of DrHsp17.7 and DrHsp20.2

This section summarizes the main results, which coworkers (Dr. Alexander Bepperling, Thomas Kriehuber, Dr. Martin Haslbeck) of the group of Prof. Buchner (Chair of Biotechnology, TUM) obtained in a comprehensive study on the sHsp-system of the polyextremophilic bacterium *Deinococcus radiodurans* (Slade and Radman, 2011). The determination of the crystal structure of DrHsp 17.7, which is described in the following chapter, serves as a contribution to the abovementioned work.

Both sHsps from *D. radiodurans* function as "holdase" chaperones, since they prevent both thermal and chemical induced aggregation of model substrates such as citrate synthase, luciferase and lysozyme *in vitro*. However, Hsp20.2 exhibits higher chaperone potency than Hsp17.7.

Analysis of the kinetics of thermal inactivation of citrate synthase indicates transient substrate complexes for Hsp17.7, whereas Hsp20.2 interacts more stable with client proteins.

Mechanistical studies on the properties of substrate complex formation showed that Hsp20.2 acts as a 16-18mer *in vitro*. However, no substrate complexes were detected for Hsp17.7. This mechanistical divergence in substrate interaction also manifests in the release of substrate proteins, as demonstrated by substantial differences between the 2 sHsps in their potential to interplay with ATP-dependent chaperone systems from *E. coli*. While Hsp20.2 readily cooperates with "foldases" in the recovery of client proteins, the presence of Hsp17.7 effects only insignificant substrate reactivation.

Structural investigations by size exclusion chromatography (SEC) and analytical ultracentrifugation (aUC) revealed that Hsp17.7 exists as a homodimer, whereas Hsp20.2 appeared in 2 major oligomeric species: a 32-36mer and a 16-18mer. Native PAGE analyses confirmed the *in vitro* oligomerization properties for both sHsps also *in vivo*. However, for Hsp17.7 low amounts of potentially tetrameric to octameric assemblies were also detected by native PAGE.

8.2 Results - Crystal Structure of Hsp 17.7

Initial crystallization trials were performed for fulllength DrHsp17.7 as described in the material and methods section. Sitting drop high throughput screens were performed by using 96-well format microplates and 5 standard crystal screening kits (Qiagen) on a Phoenix robot (Art Robbins Instruments). Crystal droplets consisted of 1 volume of reservoir solution and 1 volume of protein suspension (12 mg/mL). Crystals grew within 5 months to a final size of about 110 × 80 × 70 μm^3 with PEG3350 as precipitant.

DrHsp17.7 crystallized in the trigonal space group $P3_121$ with the following unit cell parameters: a = b = 51.3 Å, c = 80.4 Å. The structure was determined by molecular replacement (McCoy et al., 2007) using the program PHASER and the coordinates of XAC1151 (PDB ID: 3GLA) (Hilario et al., 2006) as starting model. The model was refined to 2.4 Å resolution using TLS parameters and REFMAC (Vagin et al., 2004) yielding current crystallographic values of R_{crys} = 19.7 %, R_{free} = 25.3 %, r.m.s. bond length = 0.017 Å, and r.m.s. angles = 1.54°. The 45 N-terminal amino acids as well as the last 19 C-terminal amino acids were structurally distorted. Table 12 gives an overview of the data collection and refinement statistics.

	DrHsp17.7
Crystal parameter	
Space group	$P3_121$
Cell dimensions	
a, *b*, *c* (Å)	51.3; 51.3; 80.4
α, β, γ (°)	90; 90; 120
Molecules per AU[a]	1 Hsp17.7 monomer
Data collection	
Beam line	Cu K_α
Wavelength (Å)	1.5418
Resolution range (Å)[b]	40-2.4 (2.5-2.4)
No. observations	87023
No. unique reflections[c]	5119
Completeness (%)[b]	99.9 (100.0)
R_{merge} (%)[b,d]	5.3 (36.9)
I / σ (I)[b]	18.4 (5.3)
Refinement	
Resolution (Å)	15-2.4
R_{work} / R_{free}[e]	0.197 / 0.253
No. reflections working set	4539
No. reflections test set	209
No. nonhydrogen	757
No. of solvent water	79
Average *B*-factor (Å^2)	25.8
R.m.s. deviations[f]	
Bond lengths (Å)	0.017
Bond angles (°)	1.54
Ramachandran (%)[g]	96.0 / 4.0 / 0.0

Table 12:

Data collection and refinement statistics regarding DrHsp17.7.
[a] Asymmetric unit; [b] values in parenthesis of resolution range, completeness, R_{merge} and I/σ (I) correspond to the last resolution shell; [c] Friedel pairs were treated as identical reflections; [d] $R_{merge}(I) = \Sigma_{hkl}\Sigma_j |[I(hkl)_j - I(hkl)]|/[\Sigma_{hkl} I_{hkl}$, where I(hkl)$_j$ is the jth measurement of the intensity of reflection hkl and <I(hkl)> is the average intensity; [e] $R = \Sigma_{hkl} | |F_{obs}| - |F_{calc}| |/\Sigma_{hkl} |F_{obs}|$, where R_{free} is calculated without a sigma cutoff for a randomly chosen 5% of reflections, which were not used for structure refinement, and R_{work} is calculated for the remaining reflections (Brunger, 1992); [f] Deviations from ideal bond lengths/angles (Engh and Huber, 1991); [g] Number of residues in favoured region / allowed region / outlier region

The atomic structure shows that Hsp17.7 crystallized as a homodimer, in accordance with the size determined by analytical ultracentrifugation. The monomers adopt the characteristic α-crystallin core fold, consisting of two antiparallel β-sheets, which are packed as parallel layers (Figure 39).
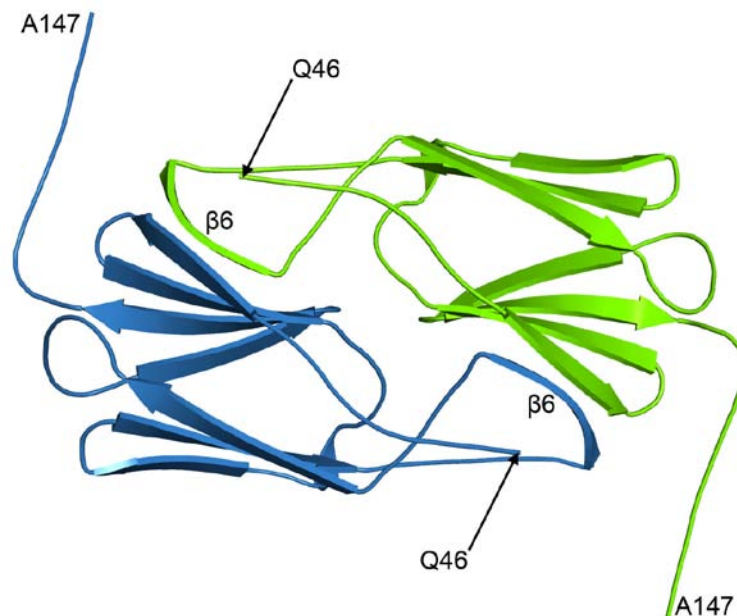
Figure 39:

Crystal structure of the DrHsp17.7 homodimer shown as cartoon. The 2 monomers are depicted in blue and green, respectively. The termini are numbered by the corresponding amino acids Q46 and A147 according to the fulllength construct. The swapped β6-strands are also indicated. The figure was created with PyMol (DeLano, 2002).

As observed for some other sHsps, the peripheral β6-strand in the extended loop of DrHsp17.7 stabilizes the dimer by interacting with the partner monomer (Bagnéris et al., 2009; McHaourab et al., 2009). A backbone superposition of sHsps from different organisms revealed significant structural divergence for the extended loop region (Figure 40). Interestingly, the backbone of the extended loop of DrHsp17.7 structurally matches best with HspA (XAC1151) from the plant pathogenic bacterium *Xanthomonas axonopodis* (Hilario et al., 2011; Lin et al.,

2010). However, XaHspA assembles into a 36mer *in vitro* and crystallizes as a
hexamer. By comparing the backbones of the four chaperones XaHspA,
MjHsp16.5, TaHsp16.9 and DrHsp17.7, the latter stands out for the narrowest
geometry of the extended loop. This alternate loop conformation might suggest a
different dimer packing, which in turn may influence oligomer formation, hence
giving structural indications for the findings that DrHsp17.7 does not build up
higher oligomers unlike XaHspA, MjHsp16.5 and TaHsp16.9.
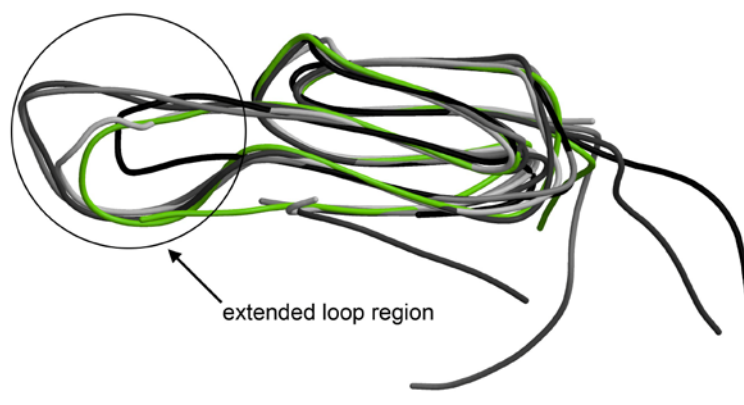
Figure 40:
Backbone superposition of one monomer of DrHsp17.7 (green), XaHspA (white),
TaHSP16.9 (grey), MjHSP16.5 (dark grey) and human αB-crystallin (black). The
comparison of the superimposed backbones exhibits significant structural variations
for the extended loop region. The figure was created with MolScript (Kraulis, 1991).

Even though the crystal structure suggests that the biological relevant form of
Hsp17.7 is a homodimer, the conserved C-terminal IXI/V motif, which usually
contributes to the formation of oligomers, forms a defined crystal contact to the
neighbouring dimer by adopting β-strand conformation (Figure 41, indicated by
arrows). Such an interface is also present both in the spherical 24mer of
MjHsp16.5 and the dodecameric double disc of TaHsp16.9 (Kim et al., 1998; van
Montfort et al., 2001). In the DrHsp17.7 crystal the dimers are arranged in a
helical, lined up manner (Figure 41) and not in globular, high oligomeric

assemblies, indicating that this contact only forms due to the high local protein concentration. Since DrHsp17.7 is a dimer up to a concentration of 1mM, it seems unlikely that oligomers form at physiological conditions. Nevertheless, the principal possibility to form interaction contacts via the IXI/V motif in addition to the compact β6-loop interface might explain the low amounts of potentially tetrameric to octameric assemblies detected by native PAGE.
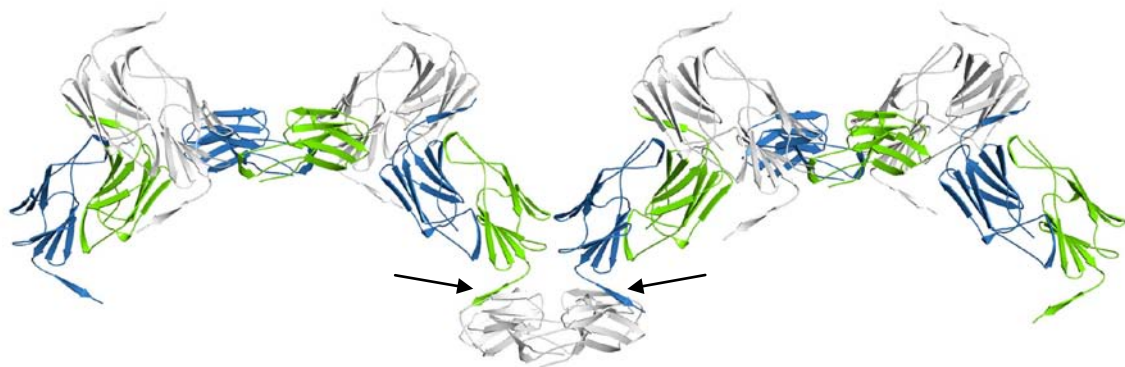
Figure 41:

Crystal packing of DrHsp17.7. The dimer building blocks are packed in a helical, lined up order owing to the trigonal space group. Note, the C-terminal extension of a monomer (blue and green, respectively; indicated by black arrows) containing the conserved IXI/V-motif adopts β-strand conformation (β10 strand) by binding in a hydrophobic groove formed by the β4 and β8 strands of an adjacent dimer (white). This intermolecular dimer-dimer connection (only marked twice here) represents a core structural motif responsible for oligomerization of MjHsp16.5, TaHsp16.9 and StHsp14.0. The figure was created with PyMol (DeLano, 2002).

8.3 Discussion

Apart from the crystallographic study on DrHsp17.7, which was performed during this thesis, this discussion on the two sHsps from *D. radiodurans* also covers some of the structural and functional work carried out by the coworkers of Prof. Buchner.

The functional assays identified Hsp17.7 and Hsp20.2 from *D. radiodurans* as active members of the sHsp chaperone family. Up to now, their affiliation to this class of proteins was based on sequence homology only (Kriehuber et al., 2010). Nevertheless, comparing the two sHsps of *D. radiodurans* with the ones of *E. coli*, which currently define the prokaryotic model system, uncovers striking structural differences in their oligomeric assemblies even though the respective monomers all share the same α-crystallin core fold. *E. coli* IbpA and IbpB form heterogeneous oligomers ranging from 600 kDa to 3 MDa with IbpA alone assembling into small fibrils (Kitagawa et al., 2002; Ratajczak et al., 2010; Shearstone and Baneyx, 1999). By contrast, the two sHsps from *D. radiodurans* show remarkable deviations to this and other assembly types of sHsps, which are often described as 12 or 24mers (Haslbeck et al., 2008; Kim et al., 1998; Saji et al., 2008; van Montfort et al., 2001; White et al., 2006). Hsp20.2 was found to be a 32-36mer which apparently is in equilibrium with a 16-18mer. Hsp17.7, however, seems to be an active dimer under physiological conditions. In the crystal structure, the monomers adopt the characteristic α-crystallin core fold. The dimer interface exhibits substantial association contacts between the β2 and β6-strands in the extended loop region (McHaourab et al., 2009) (Figure 39). In the native MjHsp16.5 and TaHsp16.9 oligomers, the C-terminal extension of the monomers crucially contributes to the assembly of the dimer building blocks by

binding to the β4-β8 hydrophobic groove of a neighbouring dimer via the IXI/V motif (Kim et al., 1998; McHaourab et al., 2009; van Montfort et al., 2001). The structural segments responsible for this dimer-dimer contact are conserved across the sHsp superfamily and recent reports showed that both a C-terminal truncation as well as an FKF mutation of the IXI/V motif interferes with oligomerization of sHsp14.0 from *Sulfolobus tokodaii* (Saji et al., 2008; Takeda et al., 2011). Intriguingly, the resolved part of the Hsp17.7 C-terminal tail makes a crystal contact to the abovementioned β4-β8 edge, belonging to a symmetry mate, by adopting an ordered β-strand conformation (Figure 41). Since the respective region comprises the conserved IXI/V motif, the principal contact site is still conserved in Hsp17.7, though it is not used to build up higher oligomers at physiological conditions. Nevertheless, these contacts reflect potential interaction sites which are involved in the crystal packing and might be relevant at high local protein concentrations *in vivo*.

Bearing in mind that Hsp17.7 exclusively exists as a dimer *in vitro* and *in vivo*, it is a striking feature that it is fully active as a chaperone in terms of suppressing the aggregation of diverse substrates *in vitro*. Only few other sHsps such as human HspB1 (Hsp27) and HspB6 (Hsp20), which usually appear as oligomers, can be shifted to an active dimeric state, under certain buffer conditions (Bukach et al., 2004; Bukach et al., 2009; Chernik et al., 2007; Hayes et al., 2009).

Hsp17.7 stands out for both its uncommon quaternary structure and the remarkable differences in its mode of substrate interaction compared to other sHsps. Although Hsp17.7 suppresses the aggregation of different model substrates, no stable substrate complexes could be detected. Additionally, inactivation of substrate proteins in the presence of Hsp17.7 together with

subsequent refolding by ATP-dependent chaperone systems gave only low refolding yields. In the context of its ability to affect the kinetics of citrate synthase thermoinactivation and Hsp70-mediated refolding of chemically denatured citrate synthase as well as the observation that no Hsp17.7 containing aggregates or complexes could be isolated, an exclusively transient interaction of Hsp17.7 with unfolded polypeptide chains is most plausible. Free Hsp17.7 as well as its substrate bound form may exist in a dynamic equilibrium preventing the creation of insoluble aggregates, possibly resulting in enhanced quantities of nonnative polypeptide chains readily available for the ATP-dependent cellular refolding machineries, thus accelerating the recovery process (Bepperling et al., manuscript in preparation).

9 References

Abrahams, J.P., A.G. Leslie, 1996. Methods used in the structure determination of bovine mitochondrial F1 ATPase. Acta Crystallogr D Biol Crystallogr 52, 30-42.

Al Refaii, A., J.H. Alix, 2009. Ribosome biogenesis is temperature-dependent and delayed in Escherichia coli lacking the chaperones DnaK or DnaJ. Mol Microbiol 71, 748-62.

Alte, F., A. Stengel, J.P. Benz, E. Petersen, J. Soll, M. Groll, B. Boelter, 2010. Ferredoxin:NADPH oxidoreductase is recruited to thylakoids by binding to a polyproline type II helix in a pH-dependent manner. Proceedings of the National Academy of Sciences of the United States of America 107, 19260-19265.

Altschul, S.F., W. Gish, W. Miller, E.W. Myers, D.J. Lipman, 1990. Basic local alignment search tool. Journal of Molecular Biology 215, 403-410.

Bagnéris, C., O.A. Bateman, C.E. Naylor, N. Cronin, W.C. Boelens, N.H. Keep, C. Slingsby, 2009. Crystal structures of alpha-crystallin domain dimers of alphaB-crystallin and Hsp20. J Mol Biol 392, 1242-52.

Balsera, M., A. Stengel, J. Soll, B. Bolter, 2007. Tic62: a protein family from metabolism to protein translocation. BMC Evolutionary Biology 7, Article No.: 43.

Benz, J.P., M. Lintala, J. Soll, P. Mulo, B. Bölter, 2010. A new concept for ferredoxin-NADP(H) oxidoreductase binding to plant thylakoids. Trends Plant Sci 15, 608-13.

Benz, J.P., A. Stengel, M. Lintala, Y.H. Lee, A. Weber, K. Philippar, I.L. Gugel, S. Kaieda, T. Ikegami, P. Mulo, J. Soll, B. Bolter, 2009. Arabidopsis Tic62 and Ferredoxin-NADP(H) Oxidoreductase Form Light-Regulated Complexes That Are Integrated into the Chloroplast Redox Poise. Plant Cell 21, 3965-3983.

Biggins, S., N. Bhalla, A. Chang, D.L. Smith, A.W. Murray, 2001. Genes involved in sister chromatid separation and segregation in the budding yeast Saccharomyces cerevisiae. Genetics 159, 453-470.

Birrell, G.W., G. Giaever, A.M. Chu, R.W. Davis, J.M. Brown, 2001. A genome-wide screen in Saccharomyces cerevisiae for genes affecting UV radiation sensitivity. Proc Natl Acad Sci U S A 98, 12608-13.

Bode, W., F.X. Gomisruth, W. Stockler, 1993. ASTACINS, SERRALYSINS, SNAKE-VENOM AND MATRIX METALLOPROTEINASES EXHIBIT IDENTICAL ZINC-BINDING ENVIRONMENTS (HEXXHXXGXXH AND MET-TURN) AND TOPOLOGIES AND SHOULD BE GROUPED INTO A COMMON FAMILY, THE METZINCINS. Febs Letters 331, 134-140.

Bode, W., F.X. Gomisruth, R. Huber, R. Zwilling, W. Stocker, 1992. STRUCTURE OF ASTACIN AND IMPLICATIONS FOR ACTIVATION OF ASTACINS AND ZINC-LIGATION OF COLLAGENASES. Nature 358, 164-167.

Bricogne, G., C. Vonrhein, C. Flensburg, M. Schiltz, W. Paciorek, 2003. Generation, representation and flow of phase information in structure determination: recent developments in and around SHARP 2.0. Acta Crystallogr D Biol Crystallogr 59, 2023-30.

Brinker, A., C. Scheufler, F. von der Mulbe, B. Fleckenstein, C. Herrmann, G. Jung, I. Moarefi, F.U. Hartl, 2002. Ligand discrimination by TPR domains - Relevance and selectivity of EEVD-recognition in Hsp70 center dot Hop center dot Hsp90 complexes. Journal of Biological Chemistry 277, 19265-19275.

Brunger, A.T., 1992. Free R-value - a novel statistical quantity for assessing the accuracy of crystal structures. Nature 355, 472-475.

Bruns, C.M., P.A. Karplus, 1995. Refined crystal structure of spinach Ferredoxin Reductase at 1.7 Angstrom resolution - oxidized, reduced and 2'-phospho-5'-AMP bound states. Journal of Molecular Biology 247, 125-145.

Bukach, O.V., A.S. Seit-Nebi, S.B. Marston, N.B. Gusev, 2004. Some properties of human small heat shock protein Hsp20 (HspB6). Eur J Biochem 271, 291-302.

Bukach, O.V., A.E. Glukhova, A.S. Seit-Nebi, N.B. Gusev, 2009. Heterooligomeric complexes formed by human small heat shock proteins HspB1 (Hsp27) and HspB6 (Hsp20). Biochim Biophys Acta 1794, 486-95.

Bügl, H., E.B. Fauman, B.L. Staker, F. Zheng, S.R. Kushner, M.A. Saper, J.C. Bardwell, U. Jakob, 2000. RNA methylation under heat shock control. Mol Cell 6, 349-60.

Carrillo, N., E.A. Ceccarelli, 2003. Open questions in ferredoxin-NADP+ reductase catalytic mechanism. Eur J Biochem 270, 1900-15.

Chernik, I.S., A.S. Seit-Nebi, S.B. Marston, N.B. Gusev, 2007. Small heat shock protein Hsp20 (HspB6) as a partner of 14-3-3gamma. Mol Cell Biochem 295, 9-17.

Christianson, D.W., 1991. Structural biology of zinc. Adv Protein Chem 42, 281-355.

Ciechanover, A., Y. Hod, A. Hershko, 1978. A heat-stable polypeptide component of an ATP-dependent proteolytic system from reticulocytes. Biochem Biophys Res Commun 81, 1100-5.

Collaborative Computational Project, N.m., 1994. The CCP4 suite: programs for protein crystallography. Acta Crystallogr D Biol Crystallogr 50, 760-3.

DeLano, W.L., 2002. The PyMOL Molecular Graphics System, DeLano Scientific, San Carlos, CA, USA.

Deng, Z., A. Aliverti, G. Zanetti, A.K. Arakaki, J. Ottado, E.G. Orellano, N.B. Calcaterra, E.A. Ceccarelli, N. Carrilli, P.A. Karplus, 1999. A productive NADP(+) binding mode of ferredoxin-NADP(+) reductase revealed by protein engineering and crystallographic studies. Nature Structural Biology 6, 847-853.

Denuc, A., G. Marfany, 2010. SUMO and ubiquitin paths converge. Biochem Soc Trans 38, 34-9.

Derelle, E., C. Ferraz, S. Rombauts, P. Rouze, A.Z. Worden, S. Robbens, F. Partensky, S. Degroeve, S. Echeynie, R. Cooke, Y. Saeys, J. Wuyts, K. Jabbari, C. Bowler, O. Panaud, B. Piegu, S.G. Ball, J.-P. Ral, F.-Y. Bouget, G. Piganeau, B. De Baets, A. Picard, M. Delseny, J. Demaille, Y. Van de Peer, H. Moreau, 2006. Genome analysis of the smallest free-living eukaryote Ostreococcus tauri unveils many unique features. Proceedings of the National Academy of Sciences of the United States of America 103, 11647-11652.

Dhanaraj, V., Q.Z. Ye, L.L. Johnson, D.J. Hupe, D.F. Ortwine, J.B. Dubar, J.R. Rubin, A. Pavlovsky, C. Humblet, T.L. Blundell, 1996. X-ray structure of a hydroxamate inhibitor complex of stromelysin catalytic domain and its comparison with members of the zinc metalloproteinase superfamily. Structure 4, 375-386.

Dorowski, A., A. Hofmann, C. Steegborn, M. Boicu, R. Huber, 2001. Crystal structure of paprika ferredoxin-NADP+ reductase. Implications for the electron transfer pathway. J Biol Chem 276, 9253-63.

Drenth, J., 2007. Principles of Protein X-Ray Crystallography. Springer Science+Business Media, New York, USA.

Egler, C., T. Albert, O. Brokemper, M. Zabe-Kuhn, G. Mayer, J. Oldenburg, R. Schwaab, 2009. Kinetic parameters of monoclonal antibodies ESH2, ESH4, ESH5, and ESH8 on coagulation factor VIII and their influence on factor VIII activity. Journal of Molecular Recognition 22, 301-306.

Ellis, R.J., S.M. van der Vies, S.M. Hemmingsen, 1989. The molecular chaperone concept. Biochem Soc Symp 55, 145-53.

Engh, R.A., R. Huber, 1991. Accurate bond and angle parameters for x-ray protein structure refinement. Acta Crystallographica Section A 47, 392-400.

Esnouf, R.M., 1997. An extensively modified version of MolScript that includes greatly enhanced coloring capabilities. Journal of Molecular Graphics & Modelling 15, 132-&.

Fling, S.P., D.S. Gregerson, 1986. Peptide and protein molecular weight determination by electrophoresis using a high-molarity tris buffer system without urea. Anal Biochem 155, 83-8.

Friedmann, D., T. Messick, R. Marmorstein, 2011. Crystallization of macromolecules. Curr Protoc Protein Sci Chapter 17, Unit17.4.

Geiss-Friedlander, R., F. Melchior, 2007. Concepts in sumoylation: a decade on. Nat Rev Mol Cell Biol 8, 947-56.

Geoffroy, M.C., R.T. Hay, 2009. An additional role for SUMO in ubiquitin-mediated proteolysis. Nat Rev Mol Cell Biol 10, 564-8.

Gong, L., S. Millas, G.G. Maul, E.T. Yeh, 2000. Differential regulation of sentrinized proteins by a novel sentrin-specific protease. J Biol Chem 275, 3355-9.

Gong, L., T. Kamitani, K. Fujise, L.S. Caskey, E.T. Yeh, 1997. Preferential interaction of sentrin with a ubiquitin-conjugating enzyme, Ubc9. J Biol Chem 272, 28198-201.

Gragerov, A.I., E.S. Martin, M.A. Krupenko, M.V. Kashlev, V.G. Nikiforov, 1991. Protein aggregation and inclusion body formation in Escherichia coli rpoH mutant defective in heat shock protein induction. FEBS Lett 291, 222-4.

Green, L.S., B.C. Yee, B.B. Buchanan, K. Kamide, Y. Sanada, K. Wada, 1991. Ferredoxin and ferredoxin-NADP reductase from photosynthetic and nonphotosynthetic tissues of tomato. Plant Physiol 96, 1207-13.

Groemping, Y., K. Rittinger, 2005. Activation and assembly of the NADPH oxidase: a structural perspective. Biochemical Journal 386, 401-416.

Grzyb, J., M. Gagos, W.I. Gruszecki, M. Bojko, K. Strzalka, 2008. Interaction of ferredoxin : NADP(+) oxidoreductase with model membranes. Biochimica Et Biophysica Acta-Biomembranes 1778, 133-142.

Gummadova, J.O., G.J. Fletcher, A. Moolna, G.T. Hanke, T. Hase, C.G. Bowsher, 2007. Expression of multiple forms of ferredoxin NADP+ oxidoreductase in wheat leaves. J Exp Bot 58, 3971-85.

Haley, D.A., M.P. Bova, Q.L. Huang, H.S. Mchaourab, P.L. Stewart, 2000. Small heat-shock protein structures reveal a continuum from symmetric to variable assemblies. J Mol Biol 298, 261-72.

Hanke, G.T., S. Okutani, Y. Satomi, T. Takao, A. Suzuki, T. Hase, 2005. Multiple iso-proteins of FNR in *Arabidopsis*: evidence for different contributions to chloroplast function and nitrogen assimilation. Plant, Cell & Environment 28, 1146-1157.

Haslbeck, M., A. Kastenmüller, J. Buchner, S. Weinkauf, N. Braun, 2008. Structural dynamics of archaeal small heat shock proteins. J Mol Biol 378, 362-74.

Hayes, D., V. Napoli, A. Mazurkie, W.F. Stafford, P. Graceffa, 2009. Phosphorylation dependence of hsp27 multimeric size and molecular chaperone function. J Biol Chem 284, 18801-7.

Hershko, A., A. Ciechanover, A. Varshavsky, 2000. Basic Medical Research Award. The ubiquitin system. Nat Med 6, 1073-81.

Hilario, E., F.J. Martin, M.C. Bertolini, L. Fan, 2011. Crystal structures of Xanthomonas small heat shock protein provide a structural basis for an active molecular chaperone oligomer. J Mol Biol 408, 74-86.

Hilario, E., E.C. Teixeira, G.A. Pedroso, M.C. Bertolini, F.J. Medrano, 2006. Crystallization and preliminary X-ray diffraction analysis of XAC1151, a small heat-shock protein from Xanthomonas axonopodis pv. citri belonging to the alpha-crystallin family. Acta Crystallogr Sect F Struct Biol Cryst Commun 62, 446-8.

Hoa, X.D., A.G. Kirk, M. Tabrizian, 2007. Towards integrated and sensitive surface plasmon resonance biosensors: A review of recent progress. Biosensors & Bioelectronics 23, 151-160.

Holm, L., P. Rosenstrom, 2010. Dali server: conservation mapping in 3D. Nucleic Acids Research 38, W545-W549.

Iyer, L.M., E.V. Koonin, L. Aravind, 2004. Novel predicted peptidases with a potential role in the ubiquitin signaling pathway. Cell Cycle 3, 1440-1450.

Jantschitsch, C., F. Trautinger, 2003. Heat shock and UV-B-induced DNA damage and mutagenesis in skin. Photochem Photobiol Sci 2, 899-903.

Johnson, E.S., 2004. Protein modification by SUMO. Annu Rev Biochem 73, 355-82.

Johnson, E.S., A.A. Gupta, 2001. An E3-like factor that promotes SUMO conjugation to the yeast septins. Cell 106, 735-44.

Johnsson, B., S. Lofas, G. Lindquist, 1991. Immobilization of proteins to a carboxymethyldextran-modified gold surface for biospecific interaction analysis in Surface Plasmon Resonance sensors. Analytical Biochemistry 198, 268-277.

Juric, S., K. Hazler-Pilepic, A. Tomasic, H. Lepedus, B. Jelicic, S. Puthiyaveetil, T. Bionda, L. Vojta, J.F. Allen, E. Schleiff, H. Fulgosi, 2009. Tethering of ferredoxin:NADP$^+$ oxidoreductase to thylakoid membranes is mediated by novel chloroplast protein TROL. Plant Journal 60, 783-794.

Kabsch, W., 2010. XDS. Acta Crystallogr D Biol Crystallogr 66, 125-32.

Kahyo, T., T. Nishida, H. Yasuda, 2001. Involvement of PIAS1 in the sumoylation of tumor suppressor p53. Mol Cell 8, 713-8.

Karplus, P.A., H.R. Faber, 2004. Structural Aspects of Plant Ferredoxin : NADP(+) Oxidoreductases. Photosynth Res 81, 303-15.

Karplus, P.A., M.J. Daniels, J.R. Herriott, 1991. Atomic structure of ferredoxin-NADP+ reductase: prototype for a structurally novel flavoenzyme family. Science 251, 60-6.

Kendrew, J.C., R.E. Dickerson, B.E. Strandberg, R.G. Hart, D.R. Davies, D.C. Phillips, V.C. Shore, 1960. Structure of myoglobin: A three-dimensional Fourier synthesis at 2 A. resolution. Nature 185, 422-7.

Kerner, M.J., D.J. Naylor, Y. Ishihama, T. Maier, H.C. Chang, A.P. Stines, C. Georgopoulos, D. Frishman, M. Hayer-Hartl, M. Mann, F.U. Hartl, 2005. Proteome-wide analysis of chaperonin-dependent protein folding in Escherichia coli. Cell 122, 209-20.

Kerscher, O., R. Felberbaum, M. Hochstrasser, 2006. Modification of proteins by ubiquitin and ubiquitin-like proteins. Annu Rev Cell Dev Biol 22, 159-80.

Kim, D.-U., J. Hayles, D. Kim, V. Wood, H.-O. Park, M. Won, H.-S. Yoo, T. Duhig, M. Nam, G. Palmer, S. Han, L. Jeffery, S.-T. Baek, H. Lee, Y.S. Shim, M. Lee, L. Kim, K.-S. Heo, E.J. Noh, A.-R. Lee, Y.-J. Jang, K.-S. Chung, S.-J. Choi, J.-Y. Park, Y. Park, H.M. Kim, S.-K. Park, H.-J. Park, E.-J. Kang, H.B. Kim, H.-S. Kang, H.-M. Park, K. Kim, K. Song, K. Bin Song, P. Nurse, K.-L. Hoe, 2010. Analysis of a genome-wide set of gene deletions in the fission yeast Schizosaccharomyces pombe. Nature Biotechnology 28, 617.

Kim, J.H., S.H. Baek, 2009. Emerging roles of desumoylating enzymes. Biochimica et Biophysica Acta 1792, 155-162.

Kim, K.K., R. Kim, S.H. Kim, 1998. Crystal structure of a small heat-shock protein. Nature 394, 595-9.

Kitagawa, M., M. Miyakawa, Y. Matsumura, T. Tsuchido, 2002. Escherichia coli small heat shock proteins, IbpA and IbpB, protect enzymes from inactivation by heat and oxidants. Eur J Biochem 269, 2907-17.

Kovács-Bogdán, E., J. Soll, B. Bölter, 2010. Protein import into chloroplasts: the Tic complex and its regulation. Biochim Biophys Acta 1803, 740-7.

Kraulis, P.J., 1991. Molscript - a program to produce both detailed and schematic plots of protein structures. Journal of Applied Crystallography 24, 946-950.

Kriehuber, T., T. Rattei, T. Weinmaier, A. Bepperling, M. Haslbeck, J. Buchner, 2010. Independent evolution of the core domain and its flanking sequences in small heat shock proteins. FASEB J 24, 3633-42.

Krissinel, E., K. Henrick, 2007. Inference of macromolecular assemblies from crystalline state. Journal of Molecular Biology 372, 774-797.

Kruuv, J., D. Glofcheski, K.H. Cheng, S.D. Campbell, H.M. Al-Qysi, W.T. Nolan, J.R. Lepock, 1983. Factors influencing survival and growth of mammalian cells exposed to hypothermia. I. Effects of temperature and membrane lipid perturbers. J Cell Physiol 115, 179-85.

Kuchler, M., S. Decker, F. Hormann, J. Soll, L. Heins, 2002. Protein import into chloroplasts involves redox-regulated proteins. Embo Journal 21, 6136-6145.

Kurisu, G., M. Kusunoki, E. Katoh, T. Yamazaki, K. Teshima, Y. Onda, Y. Kimata-Ariga, T. Hase, 2001. Structure of the electron transfer complex between ferredoxin and ferredoxin-NADP(+) reductase. Nature Structural Biology 8, 117-121.

Langer, G., S.X. Cohen, V.S. Lamzin, A. Perrakis, 2008. Automated macromolecular model building for X-ray crystallography using ARP/wARP version 7. Nat Protoc 3, 1171-9.

Larkin, M.A., G. Blackshields, N.P. Brown, R. Chenna, P.A. McGettigan, H. McWilliam, F. Valentin, I.M. Wallace, A. Wilm, R. Lopez, J.D. Thompson, T.J. Gibson, D.G. Higgins, 2007. Clustal W and clustal X version 2.0. Bioinformatics 23, 2947-2948.

Lee, G.J., A.M. Roseman, H.R. Saibil, E. Vierling, 1997. A small heat shock protein stably binds heat-denatured model substrates and can maintain a substrate in a folding-competent state. EMBO J 16, 659-71.

Li, S.J., M. Hochstrasser, 1999. A new protease required for cell-cycle progression in yeast. Nature 398, 246-51.

Li, S.J., M. Hochstrasser, 2000. The yeast ULP2 (SMT4) gene encodes a novel protease specific for the ubiquitin-like Smt3 protein. Mol Cell Biol 20, 2367-77.

Li, S.J., M. Hochstrasser, 2003. The Ulp1 SUMO isopeptidase: distinct domains required for viability, nuclear envelope localization, and substrate specificity. J Cell Biol 160, 1069-81.

Li, S.S.C., 2005. Specificity and versatility of SH3 and other proline-recognition domains: structural basis and implications for cellular signal transduction. Biochemical Journal 390, 641-653.

Lim, W.A., F.M. Richards, R.O. Fox, 1994. Structural determinants of peptide-binding orientation and of sequence specifity in SH3 domains. Nature 372, 375-379.

Lin, C.H., C.N. Lee, J.W. Lin, W.J. Tsai, S.W. Wang, S.F. Weng, Y.H. Tseng, 2010. Characterization of Xanthomonas campestris pv. campestris heat

shock protein A (HspA), which possesses an intrinsic ability to reactivate inactivated proteins. Appl Microbiol Biotechnol 88, 699-709.

Malmendal, A., J. Overgaard, J.G. Bundy, J.G. Sørensen, N.C. Nielsen, V. Loeschcke, M. Holmstrup, 2006. Metabolomic profiling of heat stress: hardening and recovery of homeostasis in Drosophila. Am J Physiol Regul Integr Comp Physiol 291, R205-12.

Matsuyama, A., R. Arai, Y. Yashiroda, A. Shirai, A. Kamata, S. Sekido, Y. Kobayashi, A. Hashimoto, M. Hamamoto, Y. Hiraoka, S. Horinouchi, M. Yoshida, 2006. ORFeome cloning and global analysis of protein localization in the fission yeast Schizosaccharomyces pombe. Nature Biotechnology 24, 841-847.

Matthijs, H.C.P., S.J. Coughlan, G. Hind, 1986. Removal of Ferredoxin-NADP$^+$ Oxidoreductase from thylakoid membranes, rebinding to depleted membranes, and identification of the binding-site. Journal of Biological Chemistry 261, 2154-2158.

Mayer, M.P., 2010. Gymnastics of molecular chaperones. Mol Cell 39, 321-31.

McCall, K.A., C. Huang, C.A. Fierke, 2000. Function and mechanism of zinc metalloenzymes. J Nutr 130, 1437S-46S.

McCoy, A.J., R.W. Grosse-Kunstleve, P.D. Adams, M.D. Winn, L.C. Storoni, R.J. Read, 2007. Phaser crystallographic software. Journal of Applied Crystallography 40, 658-674.

McHaourab, H.S., J.A. Godar, P.L. Stewart, 2009. Structure and mechanism of protein stability sensors: chaperone activity of small heat shock proteins. Biochemistry 48, 3828-37.

McPherson, A., 1990. Current approaches to macromolecular crystallization. Eur J Biochem 189, 1-23.

McPherson, A., 2004. Introduction to protein crystallization. Methods 34, 254-65.

Meluh, P.B., D. Koshland, 1995. Evidence that the MIF2 gene of Saccharomyces cerevisiae encodes a centromere protein with homology to the mammalian centromere protein CENP-C. Mol Biol Cell 6, 793-807.

Meulmeester, E., F. Melchior, 2008. Cell biology: SUMO. Nature 452, 709-11.

Mogk, A., C. Schlieker, K.L. Friedrich, H.J. Schönfeld, E. Vierling, B. Bukau, 2003. Refolding of substrates bound to small Hsps relies on a disaggregation reaction mediated most efficiently by ClpB/DnaK. J Biol Chem 278, 31033-42.

Mukhopadhyay, D., M. Dasso, 2007. Modification in reverse: the SUMO proteases. Trends Biochem Sci 32, 286-95.

Mullen, J.R., C.-F. Chen, S.J. Brill, 2010. Wss1 Is a SUMO-Dependent Isopeptidase That Interacts Genetically with the Slx5-Slx8 SUMO-Targeted Ubiquitin Ligase. Molecular and Cellular Biology 30, 3737-3748.

Mulo, P., 2011. Chloroplast-targeted ferredoxin-NADP(+) oxidoreductase (FNR): structure, function and location. Biochim Biophys Acta 1807, 927-34.

Murphy, G.J.P., G. Murphy, J.J. Reynolds, 1991. THE ORIGIN OF MATRIX METALLOPROTEINASES AND THEIR FAMILIAL RELATIONSHIPS. Febs Letters 289, 4-7.

Murshudov, G.N., A.A. Vagin, E.J. Dodson, 1997. Refinement of macromolecular structures by the maximum-likelihood method. Acta Crystallogr D Biol Crystallogr 53, 240-55.

Murshudov, G.N., A.A. Vagin, A. Lebedev, K.S. Wilson, E.J. Dodson, 1999. Efficient anisotropic refinement of macromolecular structures using FFT. Acta Crystallogr D Biol Crystallogr 55, 247-55.

Nguyen, T.T., S.-C. Chang, I. Evnouchidou, I.A. York, C. Zikos, K.L. Rock, A.L. Goldberg, E. Stratikos, L.J. Stern, 2011. Structural basis for antigenic peptide precursor processing by the endoplasmic reticulum aminopeptidase ERAP1. Nature Structural & Molecular Biology 18, 604-U118.

Nicholls, A., K.A. Sharp, B. Honig, 1991. Protein folding and association - insights from the interfacial and thermodynamic properties of hydrocarbons. Proteins-Structure Function and Genetics 11, 281-296.

O'Neill, B.M., D. Hanway, E.A. Winzeler, F.E. Romesberg, 2004. Coordinated functions of WSS1, PSY2 and TOF1 in the DNA damage response. Nucleic Acids Res 32, 6519-30.

Ochi, T., V.M. Bolanos-Garcia, V. Stojanoff, A. Moreno, 2009. Perspectives on protein crystallisation. Prog Biophys Mol Biol 101, 56-63.

Okutani, S., G.T. Hanke, Y. Satomi, T. Takao, G. Kurisu, A. Suzuki, T. Hase, 2005. Three maize leaf ferredoxin:NADPH oxidoreductases vary in subchloroplast location, expression, and interaction with ferredoxin. Plant Physiol 139, 1451-9.

Palenik, B., J. Grimwood, A. Aerts, P. Rouze, A. Salamov, N. Putnam, C. Dupont, R. Jorgensen, E. Derelle, S. Rombauts, K. Zhou, R. Otillar, S.S. Merchant, S. Podell, T. Gaasterland, C. Napoli, K. Gendler, A. Manuell, V. Tai, O. Vallon, G. Piganeau, S. Jancek, M. Heijde, K. Jabbari, C. Bowler, M. Lohr, S. Robbens, G. Werner, I. Dubchak, G.J. Pazour, Q. Ren, I. Paulsen, C. Delwiche, J. Schmutz, D. Rokhsar, Y. Van de Peer, H. Moreau, I.V. Grigoriev, 2007. The tiny eukaryote Ostreococcus provides genomic insights into the paradox of plankton speciation. Proceedings of the National Academy of Sciences of the United States of America 104, 7705-7710.

Perry, J.J., J.A. Tainer, M.N. Boddy, 2008. A SIM-ultaneous role for SUMO and ubiquitin. Trends Biochem Sci 33, 201-8.

Perutz, M.F., M.G. Rossmann, A.F. Cullis, H. Muirhead, G. Will, A.C. North, 1960. Structure of haemoglobin: a three-dimensional Fourier synthesis at 5.5-A. resolution, obtained by X-ray analysis. Nature 185, 416-22.

Pichler, A., A. Gast, J.S. Seeler, A. Dejean, F. Melchior, 2002. The nucleoporin RanBP2 has SUMO1 E3 ligase activity. Cell 108, 109-20.

Ratajczak, E., J. Strózecka, M. Matuszewska, S. Zietkiewicz, D. Kuczyńska-Wiśnik, E. Laskowska, K. Liberek, 2010. IbpA the small heat shock protein from Escherichia coli forms fibrils in the absence of its cochaperone IbpB. FEBS Lett 584, 2253-7.

Rawlings, N.D., A.J. Barrett, 1993. EVOLUTIONARY FAMILIES OF PEPTIDASES. Biochemical Journal 290, 205-218.

Rawlings, N.D., A.J. Barrett, A. Bateman, 2010. MEROPS: the peptidase database. Nucleic Acids Research 38, D227-D233.

Rhodes, D.G., R.E. Bossio, T.M. Laue, 2009. Determination of size, molecular weight, and presence of subunits. Methods Enzymol 463, 691-723.

Rhodes, G., 2006. Crystallography Made Crystal Clear, Elsevier Academic Press, Burlington, USA & San Diego, USA & London, UK.

Richter, K., M. Haslbeck, J. Buchner, 2010. The heat shock response: life on the verge of death. Mol Cell 40, 253-66.

Rubin, G.M., M.D. Yandell, J.R. Wortman, G.L.G. Miklos, C.R. Nelson, I.K. Hariharan, M.E. Fortini, P.W. Li, R. Apweiler, W. Fleischmann, J.M. Cherry, S. Henikoff, M.P. Skupski, S. Misra, M. Ashburner, E. Birney, M.S. Boguski, T. Brody, P. Brokstein, S.E. Celniker, S.A. Chervitz, D. Coates, A. Cravchik, A. Gabrielian, R.F. Galle, W.M. Gelbart, R.A. George, L.S.B. Goldstein, F.C. Gong, P. Guan, N.L. Harris, B.A. Hay, R.A. Hoskins, J.Y. Li, Z.Y. Li, R.O. Hynes, S.J.M. Jones, P.M. Kuehl, B. Lemaitre, J.T. Littleton, D.K. Morrison, C. Mungall, P.H. O'Farrell, O.K. Pickeral, C. Shue, L.B. Vosshall, J. Zhang, Q. Zhao, X.Q.H. Zheng, F. Zhong, W.Y. Zhong, R. Gibbs, J.C. Venter, M.D. Adams, S. Lewis, 2000. Comparative genomics of the eukaryotes. Science 287, 2204-2215.

Rupp, B., 2010. Biomolecular Crystallography. Garland Science, Taylor & Francis Group, LLC, New York, USA & Abingdon, UK.

Saji, H., R. Iizuka, T. Yoshida, T. Abe, S. Kidokoro, N. Ishii, M. Yohda, 2008. Role of the IXI/V motif in oligomer assembly and function of StHsp14.0, a small heat shock protein from the acidothermophilic archaeon, Sulfolobus tokodaii strain 7. Proteins 71, 771-82.

Schwartz, D.C., M. Hochstrasser, 2003. A superfamily of protein tags: ubiquitin, SUMO and related modifiers. Trends Biochem Sci 28, 321-8.

Shearstone, J.R., F. Baneyx, 1999. Biochemical characterization of the small heat shock protein IbpB from Escherichia coli. J Biol Chem 274, 9937-45.

Sheldrick, G.M., 2010. Experimental phasing with SHELXC/D/E: combining chain tracing with density modification. Acta Crystallogr D Biol Crystallogr 66, 479-85.

Sherwood, D., J. Cooper, 2011. Crystals, X-rays and Proteins - Comprehensive Protein Crystallography. Oxford University Press, New York, USA.

Shin, M., K. Tagawa, D.I. Arnon, 1963. Crystallization of Ferredoxin-TPN Reductase and its role in the photosynthetic apparatus of chloroplasts. Biochemische Zeitschrift 338, 84-96.

Sipiczki, M., 2000. Where does fission yeast sit on the tree of life? Genome Biol 1, REVIEWS1011.

Slade, D., M. Radman, 2011. Oxidative stress resistance in Deinococcus radiodurans. Microbiol Mol Biol Rev 75, 133-91.

Stamler, R., G. Kappé, W. Boelens, C. Slingsby, 2005. Wrapping the alpha-crystallin domain fold in a chaperone assembly. J Mol Biol 353, 68-79.

Stengel, A., P. Benz, M. Balsera, J. Soll, B. Bolter, 2008. TIC62 redox-regulated translocon composition and dynamics. Journal of Biological Chemistry 283, 6656-6667.

Stengel, A., J.P. Benz, B.B. Buchanan, J. Soll, B. Bolter, 2009. Preprotein Import into Chloroplasts via the Toc and Tic Complexes Is Regulated by Redox Signals in Pisum sativum. Molecular Plant 2, 1181-1197.

Stocker, W., M. Ng, D.S. Auld, 1990. FLUORESCENT OLIGOPEPTIDE SUBSTRATES FOR KINETIC CHARACTERIZATION OF THE SPECIFICITY OF ASTACUS PROTEASE. Biochemistry 29, 10418-10425.

Su, D., M. Hochstrasser, 2010. A WLM protein with SUMO-directed protease activity. Mol Cell Biol 30, 3734-6.

Szalay, M.S., I.A. Kovács, T. Korcsmáros, C. Böde, P. Csermely, 2007. Stress-induced rearrangements of cellular networks: Consequences for protection and drug design. FEBS Lett 581, 3675-80.

Takeda, K., T. Hayashi, T. Abe, Y. Hirano, Y. Hanazono, M. Yohda, K. Miki, 2011. Dimer structure and conformational variability in the N-terminal region of an archaeal small heat shock protein, StHsp14.0. J Struct Biol 174, 92-9.

Takeya, R., H. Sumimoto, 2003. Fhos, a mammalian formin, directly binds to F-actin via a region N-terminal to the FH1 domain and forms a homotypic complex via the FH2 domain to promote actin fiber formation. Journal of Cell Science 116, 4567-4575.

Tanaka, K., J. Nishide, K. Okazaki, H. Kato, O. Niwa, T. Nakagawa, H. Matsuda, M. Kawamukai, Y. Murakami, 1999. Characterization of a fission yeast SUMO-1 homologue, Pmt3p, required for multiple nuclear events, including the control of telomere length and chromosome segregation. Molecular and Cellular Biology 19, 8660-8672.

Toivola, D.M., P. Strnad, A. Habtezion, M.B. Omary, 2010. Intermediate filaments take the heat as stress proteins. Trends Cell Biol 20, 79-91.

Turk, D., 1992. Ph.D. Thesis, TU München.

Uzunova, K., K. Göttsche, M. Miteva, S.R. Weisshaar, C. Glanemann, M. Schnellhardt, M. Niessen, H. Scheel, K. Hofmann, E.S. Johnson, G.J. Praefcke, R.J. Dohmen, 2007. Ubiquitin-dependent proteolytic control of SUMO conjugates. J Biol Chem 282, 34167-75.

Vagin, A.A., R.A. Steiner, A.A. Lebedev, L. Potterton, S. McNicholas, F. Long, G.N. Murshudov, 2004. REFMAC5 dictionary: organization of prior chemical knowledge and guidelines for its use. Acta Crystallographica Section D-Biological Crystallography 60, 2184-2195.

van Heusden, G.P., H.Y. Steensma, 2008. The Saccharomyces cerevisiae Wss1 protein is only present in mother cells. FEMS Microbiol Lett 282, 100-4.

van Montfort, R.L., E. Basha, K.L. Friedrich, C. Slingsby, E. Vierling, 2001. Crystal structure and assembly of a eukaryotic small heat shock protein. Nat Struct Biol 8, 1025-30.

Vigh, L., H. Nakamoto, J. Landry, A. Gomez-Munoz, J.L. Harwood, I. Horvath, 2007. Membrane regulation of the stress response from prokaryotic models to mammalian cells. Ann N Y Acad Sci 1113, 40-51.

Vogel, J.L., D.A. Parsell, S. Lindquist, 1995. Heat-shock proteins Hsp104 and Hsp70 reactivate mRNA splicing after heat inactivation. Curr Biol 5, 306-17.

Waterhouse, A.M., J.B. Procter, D.M.A. Martin, M. Clamp, G.J. Barton, 2009. Jalview Version 2-a multiple sequence alignment editor and analysis workbench. Bioinformatics 25, 1189-1191.

Watson, J.D., F.H. Crick, 1953. Molecular structure of nucleic acids; a structure for deoxyribose nucleic acid. Nature 171, 737-8.

Welch, W.J., J.P. Suhan, 1985. Morphological study of the mammalian stress response: characterization of changes in cytoplasmic organelles,

cytoskeleton, and nucleoli, and appearance of intranuclear actin filaments in rat fibroblasts after heat-shock treatment. J Cell Biol 101, 1198-211.

Welch, W.J., J.P. Suhan, 1986. Cellular and biochemical events in mammalian cells during and after recovery from physiological stress. J Cell Biol 103, 2035-52.

White, H.E., E.V. Orlova, S. Chen, L. Wang, A. Ignatiou, B. Gowen, T. Stromer, T.M. Franzmann, M. Haslbeck, J. Buchner, H.R. Saibil, 2006. Multiple distinct assemblies reveal conformational flexibility in the small heat shock protein Hsp26. Structure 14, 1197-204.

Wood, V., R. Gwilliam, M.A. Rajandream, M. Lyne, R. Lyne, A. Stewart, J. Sgouros, N. Peat, J. Hayles, S. Baker, D. Basham, S. Bowman, K. Brooks, D. Brown, S. Brown, T. Chillingworth, C. Churcher, M. Collins, R. Connor, A. Cronin, P. Davis, T. Feltwell, A. Fraser, S. Gentles, A. Goble, N. Hamlin, D. Harris, J. Hidalgo, G. Hodgson, S. Holroyd, T. Hornsby, S. Howarth, E.J. Huckle, S. Hunt, K. Jagels, K. James, L. Jones, M. Jones, S. Leather, S. McDonald, J. McLean, P. Mooney, S. Moule, K. Mungall, L. Murphy, D. Niblett, C. Odell, K. Oliver, S. O'Neil, D. Pearson, M.A. Quail, E. Rabbinowitsch, K. Rutherford, S. Rutter, D. Saunders, K. Seeger, S. Sharp, J. Skelton, M. Simmonds, R. Squares, S. Squares, K. Stevens, K. Taylor, R.G. Taylor, A. Tivey, S. Walsh, T. Warren, S. Whitehead, J. Woodward, G. Volckaert, R. Aert, J. Robben, B. Grymonprez, I. Weltjens, E. Vanstreels, M. Rieger, M. Schafer, S. Muller-Auer, C. Gabel, M. Fuchs, C. Fritzc, E. Holzer, D. Moestl, H. Hilbert, K. Borzym, I. Langer, A. Beck, H. Lehrach, R. Reinhardt, T.M. Pohl, P. Eger, W. Zimmermann, H. Wedler, R. Wambutt, B. Purnelle, A. Goffeau, E. Cadieu, S. Dreano, S. Gloux, V. Lelaure*, et al.*, 2002. The genome sequence of Schizosaccharomyces pombe. Nature 415, 871-880.

Yeh, E.T., L. Gong, T. Kamitani, 2000. Ubiquitin-like proteins: new wines in new bottles. Gene 248, 1-14.

Yost, H.J., S. Lindquist, 1986. RNA splicing is interrupted by heat shock and is rescued by heat shock protein synthesis. Cell 45, 185-93.

Zarrinpar, A., R.P. Bhattacharyya, W.A. Lim, 2003. The structure and function of proline recognition domains. Sci STKE 2003, RE8.

Zhang, H.M., J.P. Whitelegge, W.A. Cramer, 2001. Ferredoxin : NADP(+) oxidoreductase is a subunit of the chloroplast cytochrome b(6)f complex. Journal of Biological Chemistry 276, 38159-38165.

10 Abbreviations

A   Ampere

Å   Ångstrom

A_{280} absorption at 280 nm

APS   ammonium persulfate

ATP   adenosine triphosphate

BSA   bovine serum albumine

°C   degree Celsius

dH_2O distilled water

ddH_2O double distilled water

DNA   deoxyribonucleic acid

dNTP   deoxyribonucleotide

Da   Dalton

Dr   *Deinococcus radiodurans*

Ec   *Escherichia coli*

EDTA   ethylenediaminetetraacetic acid

EtOH   ethanol

F   structure factor

FNR   ferredoxin:NADPH oxidoreductase

g   gram

GSH   glutathione reduced

GST	glutathione-S-transferase
h	hour(s)
HCl	hydrochloric acid
Hsp(s)	heat shock protein(s)
I	intensity
ID	identifier
IPTG	isopropyl β-D-1-thiogalactopyranoside
kDa	kilo Dalton
L	litre
LB	Luria Bertani
λ	wavelength
m	milli
μ	micro
M	molar
MAD	multi-wavelength anomalous dispersion
min	minute(s)
MIR	multiple isomorphous replacement
MR	molecular replacement
MW	molecular weight
n	nano
NCS	noncrystallographic symmetry

Ni	nickel
nm	nanometer
OD	optical density
PAGE	polyacrylamide gel electrophoresis
PBS	phosphate buffered saline
PCR	polymerase chain reaction
PDB	protein data bank
PEG	polyethylene glycol
pH	potentia hydrogenii
pI	isoelectric point
RNA	ribonucleic acid
RNAse	ribonuclease
rcf	relative centrifugal force
rmsd	root mean square deviation
rpm	rotations per minute
RT	room temperature
SAD	single-wavelength anomalous dispersion
Sc	*Saccharomyces cerevisiae*
SDS	sodium dodecyl sulfate
sec	second(s)
SLS	Swiss Light Source

Sp   *Schizosaccharomyces cerevisiae*

SPR   surface plasmon resonance

t   time

TAE   tris - acetic acid - EDTA

TCA   trichloroacetic acid

TEMED   tetramethylethylenediamine

Tris   tris(hydroxymethyl)aminomethane

U   unit

UV   ultraviolet

V   voltage/volt(s)

Vis   visible

Wss1   weak suppressor of Δsmt3

v/v   volume per volume

w/v   weight per volume

Zn   zinc

11 Publications

Parts of this thesis have already been published or will be published in scientific journals as listed below:

Alte, F., A. Stengel, J.P. Benz, E. Petersen, J. Soll, M. Groll, B. Boelter, 2010. Ferredoxin:NADPH oxidoreductase is recruited to thylakoids by binding to a polyproline type II helix in a pH-dependent manner. Proceedings of the National Academy of Sciences of the United States of America 107, 19260-19265.

Bepperling, A., F. Alte, T. Kriehuber, M. Groll, S. Weinkauf, N. Braun, M. Haslbeck, J. Buchner. Structural and functional divergence of the two small heat shock proteins of the stress resistant bacterium Deinococcus radiodurans. Manuscript in preparation

Alte, F., K. Hofmann, M. Groll et al. Structure and function of Wss1 from Schizo-saccharomyces pombe. Manuscript in preparation

13 Declaration

I, Ferdinand Alte, hereby declare that I independently prepared the present thesis, using only the references and resources stated. This work has not been submitted to any examination board yet. Parts of this work have been or will be published in scientific journals.

Hiermit erkläre ich, Ferdinand Alte, dass ich die vorliegende Arbeit selbständig verfasst und keine anderen als die angegebenen Quellen und Hilfsmittel verwendet habe. Die Arbeit wurde noch keiner Prüfungskommission vorgelegt. Teile dieser Arbeit wurden bzw. werden in wissenschaftlichen Journalen veröffentlicht.

Ferdinand Alte

München, November 2011